



UNIVERSITY OF LEEDS

The Southern Ultra-Compact HII Region Population

Yara Herminia Simango

Submitted in accordance with the requirements for the degree
of Master of Science

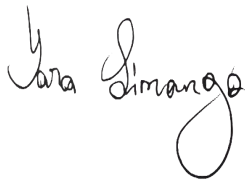
University of Leeds
School of Physics and Astronomy

February 2023

Declaration

The candidate confirms that the work submitted is her own and that appropriate credit has been given where reference has been made to the work of others.

This copy has been supplied on the understanding that it is copyright material and that no quotation from the thesis may be published without proper acknowledgement.

A handwritten signature in black ink, reading "Yara Simango". The signature is written in a cursive style with a large, looping flourish at the end of the name.

© 2023 The University of Leeds, Yara Herminia Simango

Acknowledgements

I address my gratitude to my supervisor Prof. Melvin Hoare for the exceptional support and patience, thank you for the knowledge and experience shared with me. Also a special thank you to my Co-supervisor Dr. Stuart Lumsden for helping the completion of this research. I cannot thank you enough. Dr. Tonye Irabor and Mubela thank you for some useful discussions.

A special thank you to the Development in Africa with Radio Astronomy (DARA) Newton funded project for sponsoring my masters. Also a big thank you to Prof. Claudio Paulo who introduced me to the DARA project and allowed me to work in his office while I was stuck in Mozambique waiting for my visa.

An immeasurable thank you to my parents and my siblings Katia, Salvador and Igor for the unconditional support and for never letting me give up. I love you.

To my friends Solomon, Madinah and Mercy, thank you for making my Master's time in Leeds very beautiful and for being the lap that allowed me to cry in difficult times.

Last but not less important a big thank you to my friends Dionisio and Samuel for the many python advices. To the non-academic staff, thanks for providing extra support.

Abstract

In this research the first high spatial resolution radio continuum survey of the southern galactic plane to date provided by the CORNISH-South survey is used to study a key stage of massive star forming regions. The CORNISH-South survey has the largest and well selected sample of UCHII regions of the southern Galactic plane. Taken with the Australia Telescope Compact Array (ATCA) at 5.5 GHz with 2.5 arcsec of resolution and 9 GHz with 1.5 arcsec of resolution in the region $295^\circ < l < 350^\circ$ and $|b| \leq 1^\circ$.

Observations with higher resolution of the 72 UCHII regions that were not sufficiently resolved by 5.5 GHz or 9 GHz survey were carried out with the ATCA 6 km array to provide resolutions of 0.75 and 0.55 arcsec. The majority of the sources became sufficiently resolved to show morphology, and most of them appear to be cometary. Physical properties were measured and spectral indices were estimated for the higher resolution data. At 17 GHz most of the sources remain unresolved while in 22 GHz the opposite happens. 69% of the spectral indices were consistent with free-free radiation expected from UCHII regions. The sample is composed mostly of optically thin sources. 31% of the available spectral indices are found to be below the lower limit for free-free emission, which was mainly caused by underestimation of the flux densities of the extended UCHII regions at higher resolution due to filtering out of the extended emission. The new results were combined with the available data and the spectral energy distributions (SEDs) were constructed for 59 UCHII regions, which demonstrated that the 9GHz fluxes are systematically lower than the expected.

The nature of the 255 candidate UCHII regions, detected by the CORNISH-South survey at 5.5 GHz was validated analysing the measured flux densities, angular sizes and calculated 9GHz-5GHz spectral indices. The 9 GHz observed flux densities found to be lower than expected at the SEDs, were empirically corrected, using the 5.5 to 22 GHz SEDs of the unresolved sources. The corrected fluxes were used to calculate the 9GHz-5GHz spectral indices. The UCHII regions

were found to be confined in the Galactic mid-plane as expected for very young massive star forming regions, fluxes were found to be in a range of 3 mJy to 2.413 Jy, and the majority of the sources are classified as resolved. 54% of the sample was found between the optically thin and optically thick limit, with most of the sources near the optically thin limit.

Contents

1	INTRODUCTION	1
1.1	An overview of massive star formation	1
1.1.1	Sites of massive star formation	2
1.2	HII Regions	4
1.2.1	The Strömgren Sphere	6
1.2.2	The expansions of the HII region and its evolutionary sequence	7
1.3	Ultra-compact HII Region	8
1.3.1	Morphology	9
1.4	Surveys of the Galactic Plane	14
1.4.1	The CORNISH-South survey	16
1.5	Radiative Processes in HII Regions	18
1.5.1	Radiation Transfer	18
1.5.2	Bremsstrahlung emission	21
1.6	Interferometry	23
1.7	Motivation and Thesis Outline	25
2	High Resolution Observation of Unresolved CORNISH-South UCHII regions	27
2.1	Introduction	27
2.2	Observation set-up	28
2.3	Data Flagging and Calibration	28
2.4	Imaging	30
2.5	Target detection statistics	32
2.6	Properties of the detected sources	37

2.6.1	17 GHz properties	38
2.6.2	22 GHz properties	40
2.7	22GHz-17GHz spectral indices	42
2.8	Conclusions	51
3	5.5 and 9 GHz Properties of the CORNISH-South UCHII regions	52
3.1	Introduction	52
3.2	Radio Properties of the 5.5 GHz UCHII regions	52
3.2.1	Derived physical properties	56
3.3	Aperture Photometry	58
3.3.1	Correction of the 9 GHz CORNISH-South UCHII regions	59
3.3.2	9GHz-5GHz spectral indices	61
3.4	Conclusions	63
4	Conclusion and Future Work	64
4.1	Conclusions	64
4.2	Future Work	65
	References	67
A	Additional Figures and Tables for Chapter 2	75
A.1	Radio properties of the high resolution CORNISH-South UCHII regions	76
A.2	Images of the high resolution CORNISH-South UCHII regions	80
B	Additional Figures and Tables for Chapter 3	88
B.1	Measured 5.5 and 9GHz fluxes and estimated 9GHz-5GHz spectral indices of the CORNISH-South survey	89

List of Figures

1.1	Molecular clouds in which star formation takes place.	3
1.2	Schematic evolutionary diagram proposed for the formation of massive stars from	4
1.3	Strömgren sphere	6
1.4	Morphological classification of the UCHII regions	11
1.5	Revised morphologies from De De Pree et al. (2005)	12
1.6	Histogram of different source classes identified in the CORNISH-South survey . .	17
1.7	Observational differences between UCHIIs and other sources identified in the CORNISH survey	20
1.8	Free-free thermal emission spectrum at lows frequencies, typical of HII regions (Longair 1992)	23
2.1	Work flow of the calibration pipeline adapted from the CORNISH-North calibra- tion pipeline taken from Irabor, Hoare, Oudmajer, et al. 2018	31
2.2	Images of the secondary calibrators at 17 GHz.	33
2.3	Secondary calibrators, continued.	34
2.4	Examples of the observed maps	35
2.5	Continued from previous figure	36
2.6	Histograms of the observational properties, brightness temperatures and optical depths for the high resolution sample at 17 GHz.	39
2.7	Histograms of the observational properties, brightness temperatures and optical depths for the CORNISH-South UCHII regions at 22 GHz.	41
2.8	(a)Spectral index distribution of the CORNISH UCHII regions. (b)Distribution of the spectral indices as a function of the angular sizes at 22GHz	43

2.9	Radio spectral energy distributions of UCHII regions with available 5 GHz, 9 GHz and 17 GHz and 22 GHz flux densities	47
2.10	Radio spectral energy distributions, continued	48
2.11	Radio spectral energy distributions, continued	49
2.12	Radio spectral energy distributions, continued	50
3.1	Observational radio properties of the UCHII regions sample	54
3.2	Ratio of the integrated to peak flux against angular size of the 255 CORNISH-South UCHII regions	56
3.3	Derived physical properties of the 5GHz CORNISH-South UCHII regions	57
3.4	Flux density against angular sizes, showing colour coded by the brightness temperature.	58
3.5	Distribution of the angular separation of the 154 CORNISH UCHII regions found in 9 GHz within a cross-matching radius of 3".	59
3.6	Sanity check of the aperture photometry script	60
3.7	Comparison between the observed 9 GHz flux to the predicted flux interpolated between 5 and 17 GHz	60
3.8	Plot of the RMS 3.6 cm (Urquhart, Busfield, et al. 2007) flux densities against the 9 GHz CORNISH-South flux densities	61
3.9	9GHz - 5GHz spectral index distribution of the CORNISH-South UCHII regions	62
3.10	9GHz-5GHz spectral index distribution as a function of angular sizes at 5.5 GHz	62
A.1	Radio images of the observed 17 and 22 GHz CORNISH-South UCHII regions	80
A.2	Continued from previous figure	81
A.3	Continued from previous figure	82
A.4	Continued from previous figure	83
A.5	Continued from previous figure	84
A.6	Continued from previous figure	85
A.7	Continued from previous figure	86
A.8	Continued from previous figure	87

List of Tables

2.1	Summary of observational parameters.	29
2.2	Phase calibrators for each block of observations and the longitude range.	30
2.3	Comparison of tabulated fluxes by ATCA (third column) and newly measured (last two columns) calibrator fluxes.	32
2.4	Summary of the UCHII region detection above the 7σ limit	38
2.5	Fluxes of 17 GHz and 22 GHz CORNISH-South UCHII regions, and calculated 22GHz-17GHz spectral indices	45
2.6	Continued from previous table	46
A.1	Radio properties of the high resolution CORNISH-South UCHII regions at 17 GHz	76
A.2	continued from previous page	77
A.3	Radio properties of the high resolution CORNISH-South UCHII regions at 22 GHz	78
A.4	continued from previous page	79
A.5	Radio properties of the individual sources that compose the multiple merged sources at both 17 and 22GHz	79
B.1	Fluxes of 5.5 GHz and 9 GHz CORNISH-South UCHII regions, and calculated 9GHz-5GHz spectral indices	89
B.2	Continued from previous table	90
B.3	Continued from previous table	91
B.4	Continued from previous table	92

Chapter 1

INTRODUCTION

This chapter begins with a brief summary of the massive star formation process, providing an overview of the formation sites; of the evolutionary stages of these objects and its effects in the interstellar medium (ISM). Then it focuses on bringing important concepts about HII regions, addressing concepts such as: the Strömgren sphere; the expansion and the evolutionary sequence of these regions. At the end, a summary is presented on ultra compact HII regions (UCHII), their morphology and radio surveys of the galactic plane that are key to the study of UCHII, focusing on the CORNISH-South survey.

1.1 An overview of massive star formation

Massive star is a term used to denote an OB star sufficiently massive to produce a type II supernova ($M_*/M_\odot > 8$ for solar abundances). Its formation occurs inside dense, compact clumps in giant molecular clouds, with H_2 column densities of $10^{23} - 10^{24} \text{cm}^{-2}$ (Zinnecker and Yorke 2007).

The processes that produce massive stars are not well understood. There are some obstacles studying massive stars formation, one of them being that their birth places are typically located far away from us. The closest massive star forming region, which is the Orion nebula is located 420 pc away, the second closest, which is Cepheus A is located 700 pc away and the others that are known are located more than 1000 pc away (Palla and Stahler 1999; Hughes and Wouterloot 1984). Also, the other critical problem is that massive stars evolve very quickly, i.e., from their birth to supernova explosion, which is their death, taking only a few million

years. Although a few million years do not seem to be a short period of time, in astronomical scale of events it is (generally, the lifetime of bodies in space is billions of years). That makes it difficult to trace every stage of the formation and build a full picture of how these massive stars form. Another obstacle that should be highlighted is the fact that massive stars start to fuse hydrogen consequently producing energy and light becoming very luminous, while still collecting material that leads to their formation (Zinnecker and Yorke 2007). To investigate the whole process of massive star formation, astronomers need to pick each stage of the process of massive star formation from different stars and try to join the pieces together, since to track the whole process from one single star would take millions of years.

It is very important for astronomy to overcome these difficulties because massive stars affect not only their immediate surroundings, but also influence the morphology and chemical composition of their host galaxy. Massive stars are responsible for producing most of the heavy elements across the galaxy, radiation and kinetic energy input in the ISM.

1.1.1 Sites of massive star formation

Stars are formed in dense molecular clouds located in the ISM known as **giant molecular clouds** (GMCs, illustrated in Figure 1.1), with sizes ranging from approximately 1 pc to 100 pc. Their masses vary between 10^4 to $10^6 M_{\odot}$ and they hold over 80% of the molecular hydrogen within the Milky Way with column densities varying from 10^{23} to 10^{24}cm^{-2} and temperatures varying from 10 to 15 K (Blitz 1991). For this reason, they are known as one of the largest and most massive structures within the Milky Way.

The evolutionary sequence of low-mass star formation is well understood, but its analogue for massive stars is still a challenge, due to the obstacles described in the previous section. The main issue is how different is the process that form massive stars to the one that form low-mass stars. The processes associated with the formation of massive stars were classified by Zinnecker and Yorke (2007) into the following sequence of events: **compression phase**, **collapse phase**, **accretion phase** and **disruption** and the schematic evolutionary diagram is presented in fig 1.2. There are numerous observations of star formation in OB associations that are thought to be the result of triggering. These observations suggests that massive star formation can be triggered by energetic phenomena such as the direct compression of clouds and globules, the compression and collapse of molecular clouds at the edges of HII regions and supernovae, the expansion and collapse of giant rings and shells in galaxy disks, and the collision and collapse

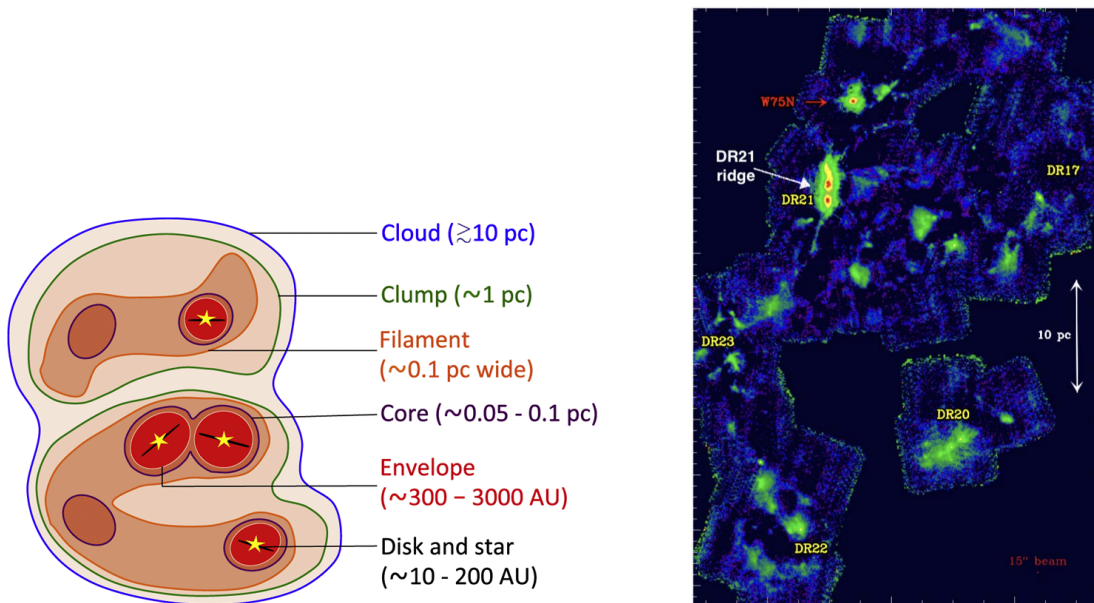


Figure 1.1 | Molecular clouds in which star formation takes place.. Left: A cartoon display of a molecular cloud showing hierarchical structures inside the cloud - the cloud, clumps, filaments, cores, envelopes and protostellar systems are shown (Pokhrel et al. 2018). Right: The Cygnus X molecular cloud complex imaged at 1.2 mm with the IRAM 30m - the mosaics approximately cover the northern part of Cygnus X. At the centre the DR21 ridge is seen, which is a 5 pc long dominating filament (Motte et al. 2018)

between two clouds (Elmegreen 1997).

When the molecular cloud becomes sufficiently unstable providing the initial conditions for collapse, the force of gravity overcomes pressure, magnetic forces, internal turbulence and rotation causing the collapse to occur (Zinnecker and Yorke 2007). The collapse results in the formation of a protostar, which is a dense, rotating and bounded hydrostatic core located in the molecular cloud. An accretion disc is formed as a consequence of the rotation of infalling material. After its formation, the protostar contracts compressing material to get up to densities and temperatures that allow the nuclear burning to occur. As the protostar evolves toward the main-sequence it accretes material. For low-mass stars, the accretion stops before hydrogen burning commences and then the pre-main-sequence star contracts to the main-sequence (Stahler 2004; Baraffe et al. 2002). However, massive stars may continue to accrete material while the star starts hydrogen burning and evolve to the main-sequence (Kudritzki 2002), i.e., massive stars are born, begin nuclear fusion and evolve to the main-sequence before the envelope has fully collapsed. That is why massive stars do not have a visible pre-main-sequence stage.

All phases of massive star formation can occur simultaneously and side-by-side in a molecular

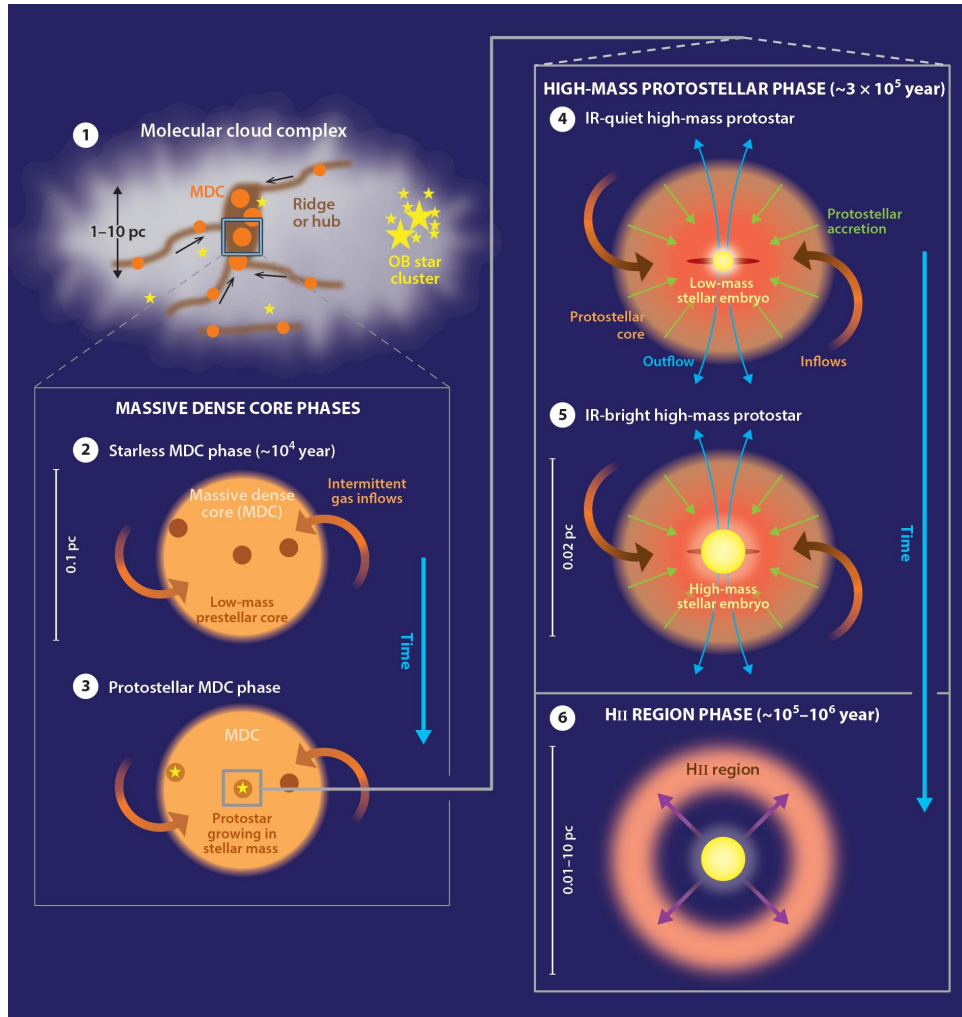


Figure 1.2 | Schematic evolutionary diagram proposed for the formation of massive stars from. (1): Massive stars forming in molecular dense cores hosted by massive filaments and spherical clumps called ridges and hubs. (2): Massive dense cores only shelter low-mass prestellar cores. (3): Low-mass prestellar cores become protostars with increasing mass rather than massive prestellar cores. (4) and (5): Protostellar envelopes accrete material from gravitationally-driven inflows, leading to the formation of massive protostar, which stays IR-quiet until reaches $8M_{\odot}$. (6): The star ionises the protostellar envelope to produce an HII region.

cloud. The dust in molecular clouds and high column densities of gas absorb the radiation coming from the recently formed massive star, turning the clouds opaque to shorter wavelengths.

1.2 HII Regions

After a massive star has formed it ionises the remaining hydrogen in the molecular cloud forming an HII region. Massive OB-type stars are buried within the cloud material from which they were born, which is mostly composed of molecular hydrogen. The ultraviolet radiation from

the stellar surface ionises the surrounding molecular hydrogen forming a bright and complex nebula known as HII region. Stars with spectral type OB have surface temperatures in order of $> 30000\text{K}$ and are able to produce a flux from UV radiation intense enough to generate ionized areas of the interstellar medium (Carroll 2017).

Considering the sequence of events that leads to the formation of massive stars, the emergence of HII regions is linked to the latest stages, i.e., shortly after the contraction of the progenitor cloud and formation of the massive stars. At the stage of ionization and consequent formation of HII regions, these objects generate remarkable effects on the surrounding interstellar environment. In fact, HII regions are considered to be one of the tracers of galactic spiral structure and a good tracer of the chemical composition of the interstellar medium in which they formed (Wenger et al. 2019).

To understand the basic structure of HII regions, the ideal case in which only one massive star is immersed inside a molecular cloud, composed solely of H_2 molecules distributed uniformly, should be considered. The most energetic photons coming from the stellar surface initially dissociate the H_2 transforming it into neutral hydrogen HI, and then ionize the resulting HI. For the HI to be ionized it is necessary that its electron receives a photon with enough energy to take it to the free state, and this minimum energy is defined as **Lyman limit**. Therefore, the Lyman limit ($\lambda = 912\text{\AA}$) is the maximum wavelength such that the photon has enough energy to ionize the atom (Stahler 2004).

While ionization occurs (before equilibrium is reached), electrons and protons from the plasma generated around the star recombine, creating a new HI atoms and giving rise to a set of emission lines, including the Balmer series. Considering that the HII regions are in equilibrium, the rate of ionization must equal the rate of recombination. When recombination occurs, the electron does not necessarily fall directly to the ground state but can cascade downward, producing a number of lower-energy photons, which will be visible in the optical and IR portion of the spectrum, specifically red colour (Carroll 2017).

The stars can only ionize a limited region of the molecular cloud around them. The ionization of the medium spreads isotropically and fills out a spherical volume of ionized gas, known as **Strömgren sphere** (Stahler 2004).



Figure 1.3 | Strömgren sphere. Left: Schematic of a spherical HII region expanding into a homogeneous medium. A shell of neutral material collected during the expansion phase surrounds the ionised region (Deharveng et al. 2010). Right: Rosette nebula there is still a cavity around the central star cluster (containing several massive objects), which was evacuated due to strong stellar winds and also due to radiation pressure acting on interstellar dust grains.

1.2.1 The Strömgren Sphere

Considering the idealized HII region introduced in the previous section (where only one massive star creates the HII region), some important information related to the dimension and boundary of Strömgren sphere can be extracted.

First it is necessary to consider that the condition of ionization balance is satisfied at each point of the HII region (after the equilibrium has been reached). Therefore, considering the entire volume of the region, the total number of ionizations per unit of time (N_{ion}) must be equal to the recombination rate (N_{rec}). If this condition were not satisfied, the volume would expand indefinitely, as the photons would need to propagate to increasingly distant regions to find non-ionised atoms (Stahler 2004). Assuming that the ionization occurs due to radiation from the "single" central massive star, then the number of ionizations must be equal to the rate at which the star emits energetic photons with energy above the Lyman limit ($N_{ion}=N_*$) (Carroll 2017). To describe recombination quantitatively, N_{rec} must be proportional to three quantities:

- To the volume of the HII region;
- To the recombination coefficient (α_{rec}), which refers to the quantum probability of an electron and a proton to combine to form an atom of HI. The recombination coefficient is a function of the temperature (T) within the region and is defined in units of $\text{cm}^3 \text{s}^{-1}$.
- To the number of electrons and protons per unit of volume (n_e and n_p).

If n_e , n_p and temperature are constant in space, then:

$$N_{rec} = \left(\frac{4}{3}\pi R_s^3\right)(n_e n_p)\alpha_{rec} \quad (1.1)$$

where R_s is the Strömngren sphere radius.

Based on the assumption that the gas is composed solely of hydrogen, and that the medium is fully ionized, $n_e = n_p$. R_s is estimated by applying the condition $N_* = N_{rec}$ and organizing equation 1.1:

$$R_s = \left[\frac{3N_*}{4\pi\alpha_{rec}n_e^2}\right]^{1/3} \quad (1.2)$$

When an HII region is formed the ionization of the surrounding medium spreads so rapidly that the original density of the cloud hardly changes (Stahler 2004). Thus in equation 1.2 n_e is equal to the number density of hydrogen atoms outside the Strömngren sphere (n_H), since the cloud is molecular n_H is the doubled becoming n_{H2} (the number density of H_2). Therefore

$$R_s = \left[\frac{3N_*}{16\pi\alpha_{rec}n_{H_2}^2}\right]^{1/3} \quad (1.3)$$

1.2.2 The expansions of the HII region and its evolutionary sequence

At the earliest stages, no HII region at all exists around the star. Later, the region spreads quickly to the Strömngren radius, basically due to the excess of UV photons emitted by the central object, and after that, a slower expansion occurs, due to the high thermal pressure of the ionized interior, when compared to the external medium. During its formation, the HII region undergoes two consecutive expansions, which will be explained in more details below.

- **First expansion:** First it is assumed that the molecular cloud has uniform density. The flow of UV photons ionizes the surrounding medium and the edge of the ionized volume starts to expand. The moving edge of the HII region is known as the **ionization front** and it defines a sphere with radius R smaller than the Strömngren radius R_s . In this case N_* is too big compared to N_{rec} . The additional flux of the photons reaches the ionization front and ionizes the gas located beyond this limit, causing the edge of the HII region to expand quickly. The time for the first expansion is approximately 100 years. During this time the average speed is about $6 \times 10^3 \text{ kms}^{-1}$ (Stahler 2004). The expansion speed exceeds

the speed of sound in an isothermal medium by approximately 3 orders of magnitude, so the expansion is supersonic. Given this discrepancy, there is not enough time during expansion for the density within the HII region to change considerably. This justifies the initial assumption that the density inside the volume is equal to the density outside.

- **Second expansion:** From the first expansion it is already known that the density inside the ionized volume is equal to the external density. As the temperature inside the HII region is of the order of 10^4K while in the molecular cloud outside the temperature is around 10K , the internal pressure must be much greater than the external pressure by about 3 magnitudes. The difference in pressure is responsible for the second expansion phase. Once the radius of the ionized sphere reaches R_s and the velocity decays to values close to $c_s = 11\text{kms}^{-1}$ (the speed of sound in an ionized medium at 10^4K , according to Stahler (2004)), the changes in pressure and density within the region reach the ionization front and generate a shock front, which is expanding. The advance of the shock front leads to the formation of neutral material around the HII region shown in figure 1.3. The ionization and shock boundaries continue to move, but with velocity gradually decreasing until equilibrium is reached.

The evolutionary sequence described above may be observationally apparent through a set of phases associated with different characteristics of the interstellar medium. In general, the evolution of a HII region, from its beginning, goes through the following consecutive stages (Zinnecker and Yorke (2007), and references contained therein): (i) Dark molecular clouds that emit in the infrared (IR) range, (ii) Hot molecular core, (iii) hyper-compact HII (HCHII) regions, (iv) ultra-compact HII (UCHII) regions and (v) compact and classical HII regions.

1.3 Ultra-compact HII Region

The earliest applied definition of the ultra-compact (UC) HII regions was given by Wood and Churchwell (1989). They defined UCHII regions as embedded photoionized regions with diameters ≤ 0.1 pc, emission measures $\geq 10^7$ pc cm⁷ (which is a physical property defined by the integral of n_e^2 along the line of sight), and electron densities $\leq 10^4$. They are one of the best indicators of recent massive star formation. At far-infrared wavelengths, they are the most luminous objects in the Galaxy, and they are observable in the radio wavelength if their luminosities are equivalent or higher than in a B0.5 main sequence star (Churchwell 2002).

The estimated age of UCHII regions is between $10^4 - 10^5$ years, determined from their spatial diameters and the typical expansion rates of HII regions (Churchwell 2002).

1.3.1 Morphology

The morphology of the UCHII regions first became accessible with the advent of radio interferometry (Wood and Churchwell 1989). The main purpose of dividing the UCHII regions into morphological classes is to group together sources which appear to have similar interactions with the environment. Israel (1977) reported low resolution interferometric observations in an extensive survey. He identified 40 potential UCHII regions but did not have sufficient resolution to reveal their internal structure. Wood and Churchwell (1989) were the first to identify five morphological classes of UCHII regions based on the appearance of their radio continuum brightness distributions. In their extensive survey of IR selected sources they observed seventy-five UCHII regions with 0.4" resolution at 2 and 6 cm using the Very Large Array (VLA), which was sufficient to classify the five classes. Out of their sample 43% of the sources were classified as spherical or unresolved; 20% as cometary; 16% core-halo; 4% shell and 17% irregular or multiply peaked, shown in a schematic diagram in figure 1.4 and described below.

- **Cometary:** In this class the ionization front is parabolic and shaped like a comet. Its leading edge is sharp and well defined. The surface brightness decreases gradually from the "head" to the "tail";
- **Core-halo:** In this class an extended low surface-brightness halo surrounds a single compact peak usually located in the centre;
- **Shell:** At wavelengths where the gas is optically thin the shell appears as a bright ring of emission and when the gas is optically thick the shell appears as a uniform-surface brightness disk. In some cases the shell appears to be broken or partially complete;
- **Irregular or multiply peaked:** In this class, several peaks are seen, usually within a common, low surface-brightness halo;
- **Spherical or unresolved:** This class may show structure when high resolution observations are available.

With similar techniques, Kurtz, Churchwell, et al. (1994) made a radio continuum observations of 59 objects selected from the *Infrared Astronomical Satellite* (IRAS) survey and found

a similar distribution of morphological classes. Walsh, Burton, et al. (1998) obtained high resolution radio continuum images of a large number of UCHII regions using the ATCA. They used the classification criteria of Wood and Churchwell (1989) and classified their sources as either cometary (43%) or irregular (40%), after ignoring the unresolved ones. Different morphologies of UCHII regions show different physical processes in the surrounding medium. Understanding the morphologies provide knowledge of the state of the surrounding medium soon after the formation of massive star (Hoare, Kurtz, et al. 2007). Using high resolution, multifrequency and multiconfiguration VLA observations of two massive star forming regions, W49A and Sgr B2, De Pree et al. (2005) classified the morphology of nearly 100 UCHII regions. These multiconfiguration observations provided more spatial dynamic range leading to modifications of the morphological classification scheme given by Wood and Churchwell (1989). They removed the core-halo classification and instead concentrated on the morphology of the compact source overlapping an extended emission, added a bipolar (UCHII regions elongated along one axis) and changed the shell classification to shell-like. The percentage of each morphological class had good agreement with the Galactic plane surveys by Wood and Churchwell (1989) and Kurtz, Churchwell, et al. (1994) for most types, except the shell-like, which was a higher percentage by nearly a factor of 10. Although, almost half of the shell-like sources classified by De Pree et al. (2005) could also be classified as cometary, since they are asymmetric (Hoare, Kurtz, et al. 2007). High sensitivity observations of cometary UCHII regions can show cavities caused by the wind from the ionising star, which are not seen in less sensitive observations, and cause them to appear more shell-like. Kurtz, Watson, et al. (1999) conducted a VLA D configuration radio continuum survey of 15 random UCHII regions out of which 12 (80%) were found associated with extended emission. In 8 (53%) sources the authors suggested that the extended emission may have a direct physical relationship to the UCHII region. In VLA multiconfiguration 21 cm radio continuum survey and radio recombination line (RRL) observations of 16 UCHII regions, Kim and Koo (2001) found that in all 16 cases the UCHII regions were associated with extended emission. Their RRL data supported the idea that the extended emission is directly related to the ultracompact emission, which has not been confirmed by Kurtz, Watson, et al. (1999). Following up on the older classification scheme introduced by Wood and Churchwell (1989) and modified by De Pree et al. (2005), (Kalcheva 2018) presented the morphology distribution of 213 UCHII regions in the CORNISH-North survey with different methods (radio-only at 1.5 and 0.3 arcsec, mid-IR, and combined multi-wavelength and multi-resolution). The radio, IR and multi-

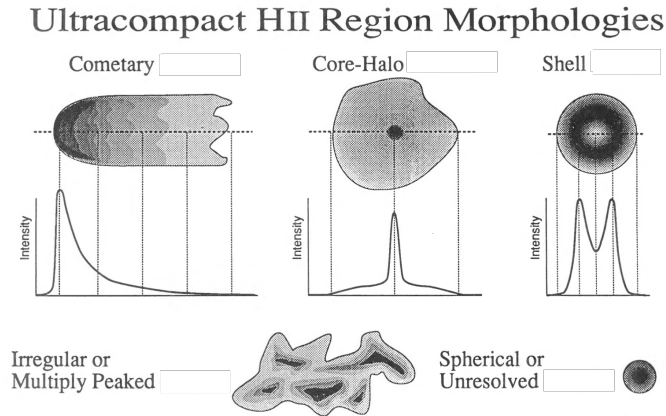


Figure 1.4 | Morphological classification of the UCHII regions. A schematic representation of the five morphological classes of UCHII regions observed and described by Wood and Churchwell (1989)

wavelength morphological classification was based on the most recent classification presented by (De Pree et al. 2005). The classification by (Kalcheva 2018) falls into five morphological classes: Cometary, shell-like, spherical, bipolar and irregular. In the cometary morphology the tail is often significantly brighter and more extended at mid-IR compared with the radio wavelength, due to the limit on the dynamic range. UCHII regions assigned to be shell-like appear as a complete or broken rings. The spherical classification was assigned for sources that appear as a two-dimensional Gaussian brightness distribution, these sources can be insufficiently resolved or cometary seen along their symmetry axes. At higher resolution irregular sources can be resolved into pairs or multiple sources. Broken-up, noisy-appearing UCHII regions identified by comparing their mid-IR and radio appearance were not considered to be ‘true’ irregulars in Kalcheva (2018), given the fact that they are likely to be the result of over-resolution of extended sources in interferometric observations. With the joint radio-IR classification (Kalcheva 2018) cometary UCHII regions were found to be predominant, comprising 71% of the resolved sample, the second largest group was irregular, comprising 14% followed by bipolar, shell-like and spherical with 8, 5 and 2% respectively. Kalcheva (2018) concluded that the observed fraction of cometary UCHII regions likely depends on age. The fraction of cometary UCHII regions found in the CORNISH-North survey is much larger than in the previous, radio-only, classifications, where more spherical or shell-like than cometary UCHIIs were found. As forewarned by Wood and Churchwell (1989), Kurtz, Churchwell, et al. (1994) and Hoare, Kurtz, et al. (2007) other morphology distribution can also change, depending on the type, sensitivity and resolution of the observation performed. Radio-only, classification of the morphology of UCHII regions, come

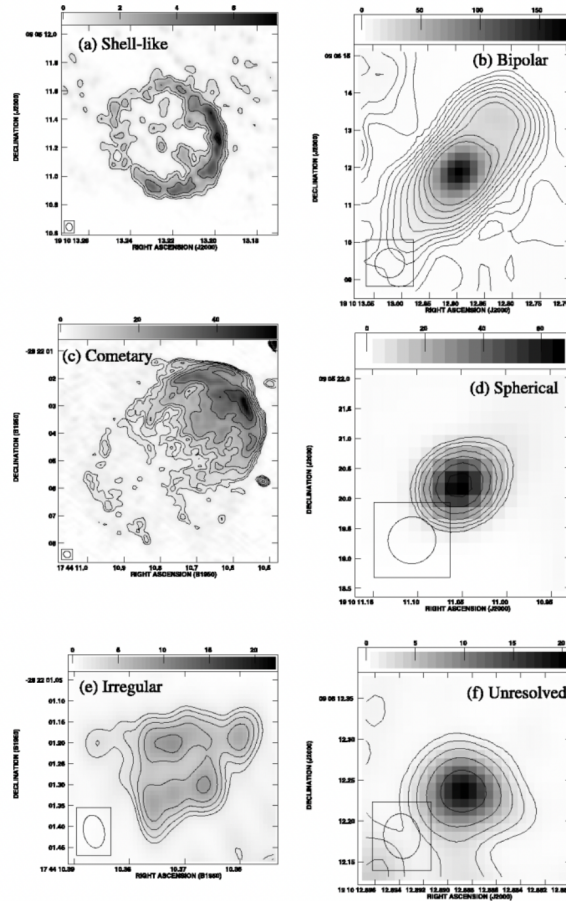


Figure 1.5 | Revised morphologies from De De Pree et al. (2005). (a) Shell-like source, W49A/D (7 mm; De Pree et al. 2004); (b) bipolar source, W49A/A (3.6 cm; De Pree et al. 1997a); (c) cometary source, Sgr B2 Main/I (1.3 cm; Gaume et al. 1995); (d) spherical source, W49A/R (3.6 cm; De Pree et al. 1997a); (e) irregular source, Sgr B2 Main/F2 (7 mm; De Pree et al. 1998); and (f) unresolved source, W49A/A2 (7 mm; De Pree et al. 2004).

with dynamical range limitations due to the nature of high resolution radio interferometry, IR or joint radio-IR classification can overcome these limitations as presented by Kalcheva (2018).

Theoretical models of the morphology of UCHII regions

Theoretical models of UCHII regions have been proposed to explain the origin of the morphological types classified through observations. Since the cometary class is very common and has a regular structure, it has been used to test some notable models, such as the champagne flow or blister model (Israel (1978); Tenorio-Tagle (1979)); the bow shock model (Van Buren et al. 1990); and the clumpy model (Dyson et al. 1995). Israel (1978) points that several authors suggest that at least to specific HII regions the exciting star is located near the edge of a neutral cloud, causing ionization fronts to move slowly into the cloud. A cavity is filled with ionized gas and dust may result from which gas flows away into space. As for the author this situation is very reminiscent of a blister on the skin of a molecular cloud, he first introduced the term blister model referring to this situation. The champagne model presented by Tenorio-Tagle (1979) proposes an explanation for the evolution of HII regions similar to the blister model introduced by Israel (1978). The model assumes a main sequence O star and its initial Strömgren sphere placed inside, and near the edge of a dense cloud. The author assumes that at the initial stage the HII region is spherically symmetric and optically not observable. As the blister model referred by Israel (1978), the champagne model assumes that a star forms near the edge of a cloud and begins to form the Strömgren sphere causing the ionization front to move eventually into the cloud and setting and pressure discontinuity between the ionized cloud material and the recently ionized cloud medium. The pressure gradient produces a strong shock which moves into the ionized cloud material. Finally the ionized cloud material flowing behind the shock is then spread over a very extended region, producing an observable ionized nebula.

Through radio observations of the UCHII region G34.3+0.2 Reid and Ho (1985) explains the effect of the stellar motion on the shape of the UCHII regions, the author suggests that the cometary appearance of the UCHII regions is due to the relative motion of the exciting star and its surroundings. In the bow shock model theory the cometary shape is explained as bow shocks created by wind-blowing massive stars moving supersonically through molecular clouds (Van Buren et al. 1990).

The clumpy model also called mass-loading model proposed by Dyson et al. (1995) suggests that the UCHII regions are result of the interaction of the wind and ionizing radiation from a young massive star with the clumpy molecular cloud gas in its vicinity. They present the clumpy model as a possible explanation for the shell-like morphology of the UCHII regions.

Lumsden and Hoare (1996) modeled the density and velocity structure of the cometary UCHII

region G29.96-0.02 through observing IR spectra of the $Br\gamma$ line. They noted that the bow shock model fails to explain the large velocity gradient across the tail of UCHII, which can be explained by the champagne model. However, the champagne model is not able to fit all of the features of the observational data, and thus should include the effects of stellar winds and density gradients to match more these data. Through the investigation of the champagne flow model plus stellar wind, and combined bow shock and champagne flow models with varied density gradients, stellar wind strengths and stellar motion, Arthur and Hoare (2006) demonstrated that the observed limb-brightened morphologies can be explained with the inclusion of stellar winds in the champagne flow model. Steggle et al. (2017) recently modeled the evolution of cometary HII regions with strong stellar winds and zero-age main-sequence ionising stars born off-centre from power-law density gas clouds for different stellar masses, age and core density. The authors found that features such as cavities and limb-brightening are produced. With these models, the observed spherical and shell morphological classes can be explained to arise due to different viewing angles, luminosities, and distances of the cometary H II region.

1.4 Surveys of the Galactic Plane

Since the late 1980s and early 1990s the surveys of the Galactic plane have been improving our understanding of massive star formation (Kurtz, Churchwell, et al. 1994). The modern family of Galactic plane surveys was able to include dust, molecular and ionized gas. The most outstanding when it comes to the study of UCHII regions include the GLIMPSE survey (Benjamin et al. 2003; Churchwell et al. 2009); the MIPS GAL survey (Carey et al. 2009); the ATLASGAL survey (Schuller et al. 2009); the UKIDSS survey (Lucas et al. 2008); the Hi-GAL Survey (Molinari, Swinyard, et al. (2010); Molinari, Schisano, et al. (2016)), and the CORNISH (North and South) survey (Hoare, Purcell, et al. 2012; Purcell et al. 2013).

The GLIMPSE Survey (Mid-Infrared)

The Galactic Legacy Infrared Mid-Plane Survey Extraordinaire (GLIMPSE) is one of the *Spitzer Space Telescope* Legacy science program survey of $\frac{2}{3}$ of the inner Galactic disc. With a resolution of $\sim 2''$, mid-infrared observations at 3.6, 4.5, 5.8 and $8.0\mu\text{m}$ were used to cover the Galactic latitudes $|b| \leq 1^\circ$ and longitudes $|l| = 10^\circ$ to 65° (both sides of the Galactic centre). The survey contains the outer ends of the Galactic bar, the Galactic molecular ring, and the inner spiral arms (Benjamin et al. 2003). It has contributed significantly to our understanding of star

formation and early evolution, the interstellar medium, Galactic structure and evolved stars (Churchwell et al. 2009).

The MIPS GAL survey (Mid-Infrared)

The MIPS GAL survey is one of the Spitzer Space Telescope surveys, covering 278 deg^2 of the inner Galactic plane (longitude, $5^\circ < l < 63^\circ$, and $298^\circ < l < 355^\circ$ and latitude, $|b| < 1^\circ$). This survey was carried out using the MIPS (Multiband Infrared Photometer for Spitzer) on the Spitzer Space Telescope in two passbands, 24 and $70 \mu\text{m}$ achieving a resolution of $6''$ and $18''$, respectively. (Carey et al. 2009). The survey was designed as a longer-wavelength complement to the shorter-wavelength Spitzer survey of the Galactic plane: GLIMPSE.

The Hi-GAL Survey (Far-infrared)

The Hi-GAL survey (Herschel infrared Galactic Plane Survey) is a survey of the Galactic plane that covers the region comprising $-70^\circ \leq l \leq +68^\circ$ and $|b| \leq 1^\circ$ in five wavelengths ($70\mu\text{m}$, $160\mu\text{m}$, $250\mu\text{m}$, $350\mu\text{m}$ and $500\mu\text{m}$). This survey used the PACS and SPIRE photometric cameras of the Herschel Space Observatory to achieve a resolution of $6''$, $12''$, $18''$, $24''$ and $35''$ in each of the five wavelengths, respectively. The aim of the Hi-GAL survey was to detect the earliest phases of the formation of molecular clouds and massive stars and deliver a homogeneous census of star forming regions and cold structures in the ISM.

The UKIDSS survey (Near-infrared)

The UKIDSS survey (UKIRT Infrared Deep Sky Survey) is a portfolio of five survey components carried out using the UKIRT (United Kingdom Infrared Telescope) wide field camera in the infrared band with a prime aim of providing a long-term astronomical legacy data base. With these five survey components being the Large Area Survey, the Galactic Clusters Survey, the Galactic Plane Survey, the Deep Extragalactic Survey and the Ultra Deep Survey (Lawrence et al. 2007). The UKIDSS Galactic Plane Survey (GPS) surveys 1868 deg^2 of the northern and equatorial Galactic plane, at Galactic latitudes of $|b| \leq 5^\circ$ and longitude of $15^\circ < l < 107^\circ$, and $142^\circ < l < 230^\circ$ with a seeing of $\sim 1.0''$. These regions were imaged in the J, H and K bands centred on $1.25 \mu\text{m}$, $1.65 \mu\text{m}$ and $2.20 \mu\text{m}$, respectively (Lucas et al. 2008).

The ATLAS GAL Survey (Sub-mm)

The ATLAS GAL is a systematic dust survey of 420 deg^2 of the inner Galactic plane that has been used to identify $\sim 10\,000$ dense molecular clumps at $870 \mu\text{m}$ using the APEX telescope (Schuller et al. 2009). It has contributed on understanding of how and under what conditions

star formation takes place and provided a well characterized sample of Galactic star-forming sites that delivered an evolutionary sequence and a mass function of high-mass, star-forming clumps.

The CORNISH survey (radio)

The CORNISH (Co-Ordinated Radio 'N' Infrared Survey for High-mass star formation) survey is the radio continuum part of a serie of multi-wavelength surveys of the Galactic plane, divided into the southern and the northern part of the Galactic plane. Using the VLA in B and BnA configurations at 5 GHz, the northern part covers 110 deg^2 of the Galactic plane defined by $10^\circ < l < 65^\circ$ and $|b| < 1^\circ$, with a resolution of $1.5''$ and sensitivity better than 0.4 mJy/beam (Purcell et al. 2013). The southern part covers an area of 110 deg^2 defined by $295^\circ < l < 350^\circ$ and $|b| < 1^\circ$ observed with all six antennas of the ATCA (Australia Telescope Compact Array)) at 5.5 and 9 GHz, with a resolution of $2.5''$ and $1.5''$ respectively (Irabor, Hoare, Burton, et al. 2023). Although the CORNISH survey describes various science topics, its prime scientific motivation is to provide an unbiased survey for UCHII regions (Hoare, Purcell, et al. 2012).

1.4.1 The CORNISH-South survey

The CORNISH-South survey catalogue provides a complete and unbiased sample of UCHII regions in the southern Galactic plane with sufficient resolution to investigate these sources. The CORNISH survey science goals, motivation, design, observation and data processing methodology are described in Hoare, Purcell, et al. (2012) and Purcell et al. (2013) for the northern counterpart and Irabor, Hoare, Burton, et al. (2023) for the southern counterpart. Observations of the southern counterpart of the CORNISH survey were carried out with all six antennas of the ATCA, using 2 GHz bandwidth of the CABB correlator between 2010 and 2012. The objects identified in the CORNISH-South survey comprise HII regions, planetary nebulae, radio galaxies and radio stars, their distribution is presented in figure 1.6.

The CORNISH-South catalogue comprises nearly 5000 detected sources and 1868 classified sources in the 7σ , where 255 (13.6 %) are UCHII regions. These highly reliable candidates UCHII regions were identified based on visual inspection of the CORNISH-South sources from other high-resolution and high-sensitivity surveys of the galactic plane (GLIMPSE, VVV, VPHAS, Hi-GAL and ATLASGAL) at other wavelengths over which UCHII regions emit. The choice of the surveys considered was based on comparable resolution and coverage. This criterion was also used by the CORNISH-North team for the sample selection and also by Urquhart, Hoare, et al.

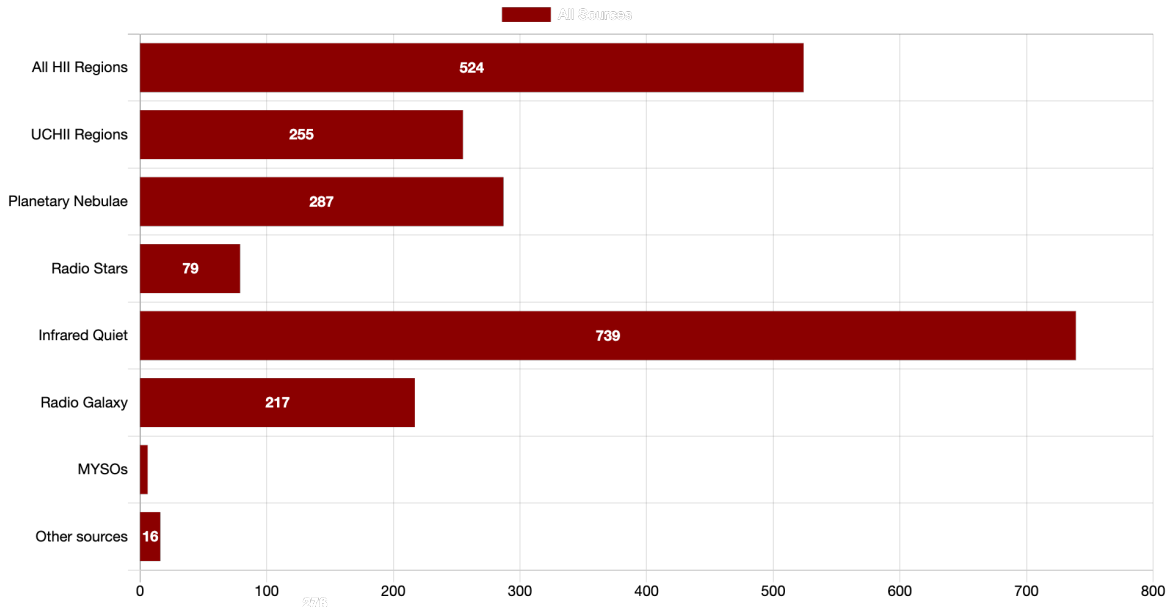


Figure 1.6 | Histogram of different source classes identified in the CORNISH-South survey. Infrared quiet sources are extragalactic sources that are relatively bright at radio wavelengths and not detected or extremely faint at infrared wavelengths (Norris et al. 2006)

(2009) to distinguish between HII regions and PNe in the RMS survey. The visual inspection method used to classify the different classes of sources in the CORNISH-South survey consisted in identifying the observational differences between the sources in the different wavelengths, and some examples are provided in figure 1.7.

The easiest source classes to distinguish from the UCHII regions are the radio galaxies and radio stars. Radio galaxies have no infrared counterpart and radio stars have lack of mid and far-infrared emission, they are also point sources in every wavelengths they are detected in (Ira- bor, Hoare, Burton, et al. 2023).

MYSOs, unlike UCHII regions, do not have strong $8.0 \mu\text{m}$ PAH (polycyclic aromatic hydrocarbon) emission. They are also generally undetected at 5GHz, even though there are a few known MYSOs observed at radio wavelengths, with radio luminosities always below $30 \text{ mJy } kpc^2$. Therefore sources above this limit are HII regions or planetary nebulae (Purser, Lumsden, Hoare, Urquhart, et al. 2016). The sensitivity of the CORNISH-South survey makes the radio emission from a few known massive young stellar objects (MYSOs) to be detected (Ira- bor, Hoare, Burton, et al. 2023). They share all the infrared characteristics of HII regions, but have very weak radio emission compared to the HII regions in general and are unresolved or jet-like (Purser, Lumsden, Hoare, Urquhart, et al. 2016).

Most extra-galactic radio sources are undetected in corresponding optical, infrared and sub-

millimetre surveys used in the CORNISH-South source classification and therefore they are easy to identify (Irabor, Hoare, Burton, et al. 2023).

This makes PNe the most likely contaminants of the selected sample of UCHII regions. Unlike PNe, UCHII regions are found within molecular clouds, often being part of a clustered environment. HII regions have strong, and usually extended, mid-IR, far-IR and sub-millimetre counterpart emission while PNe also have strong mid-IR counterparts but are much fainter at far-IR wavelengths than HII regions, and are usually undetected in the sub-millimetre band (Purser, Lumsden, Hoare, Urquhart, et al. 2016). The morphology of the UCHII regions in the infrared emission is usually irregular and complex. Their radio emission is usually fairly strong and when resolved can have a cometary, shell or irregular morphology while PNe are morphologically much simpler than HII regions and are isolated rather than being in clustered, complex environments (Sahai et al. 2011).

To distinguish the UCHII regions from HII regions, diffuse HII region and IR-Dark HII regions, all HII regions less than 5" in size have been labelled as UCHII regions. This correspond to the typical 0.1 pc size of UCHII regions if they were at a typical distance of 4 kpc for the more nearby part of the population of UCHII regions (Irabor, Hoare, Burton, et al. 2023).

After visual inspection it is expected that the sample is free of possible contaminants, however, having done visual classification does not guarantee that the sample is 100% free of contaminants.

1.5 Radiative Processes in HII Regions

In this section the physical processes that result in the emission observed by us and their use in determining the densities and temperatures of the emitting regions are characterized. Initially, the transfer of radiation inside the ionized cloud and in the interstellar medium is explained in detail. Then the thermal bremsstrahlung process is described, developing the general theory of classical braking radiation and, following the original papers by Oster (Oster 1961) and Scheuer (Scheuer 1960).

1.5.1 Radiation Transfer

Radiation that travels through a medium capable of emitting and absorbing photons to an observer can be written in terms of the variation of the radiation intensity I_ν as a function of

optical depth τ_ν , being mathematically expressed as the equation of radiative transfer (equation 1.4).

$$\frac{dI_\nu}{d\tau_\nu} = -I_\nu + S_\nu \quad (1.4)$$

with $d\tau_\nu = \kappa_\nu ds$, where ds is the distance traveled and κ_ν is the absorption coefficient; S_ν is the ratio between the emission and absorption coefficients, called the source function, and describes the interaction of radiation with the propagation medium.

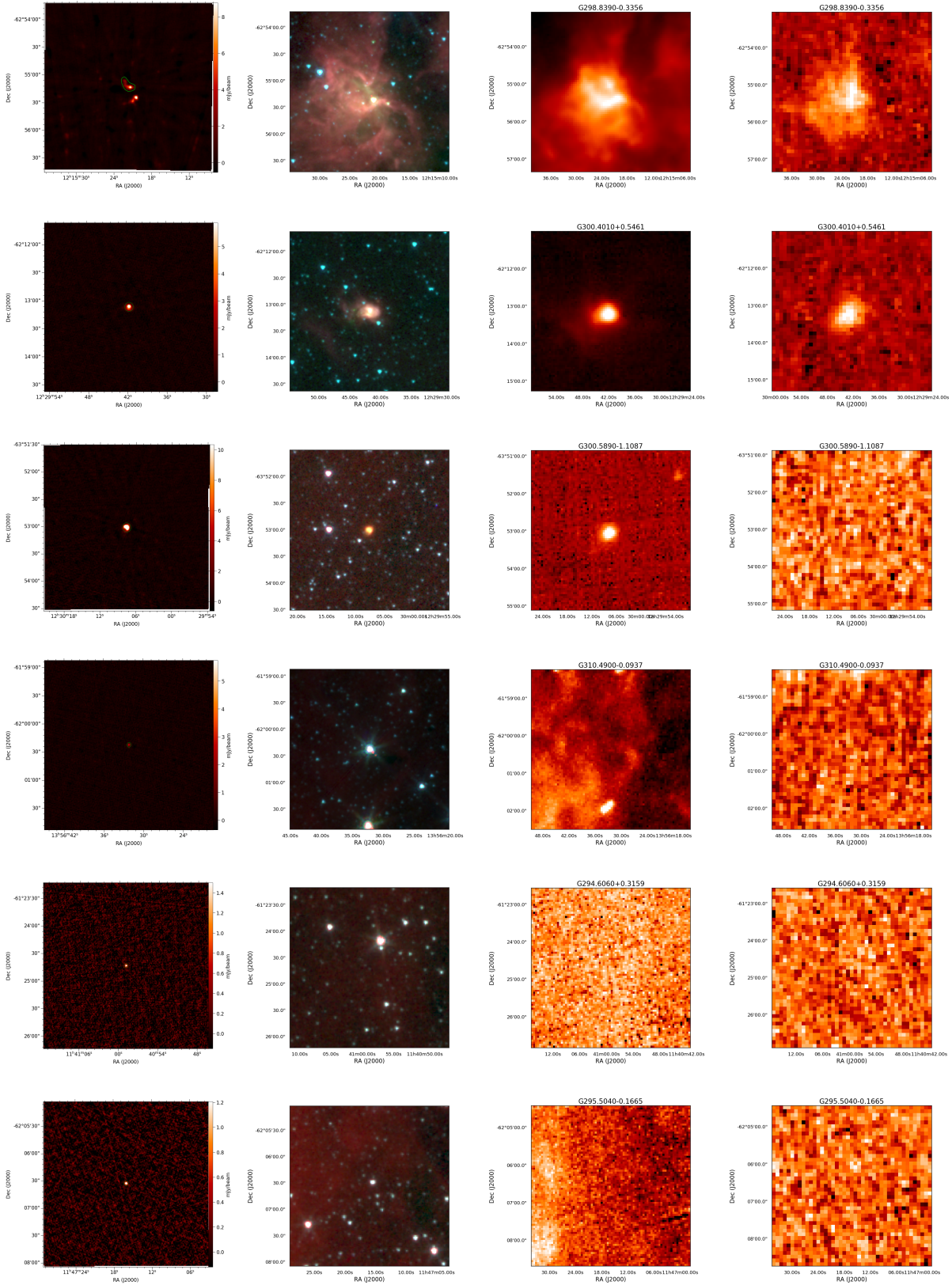


Figure 1.7 | Observational differences between UCHIs and other sources identified in the CORNISH survey. From the left: 5.5-GHz radio (CORNISH), 3-colour GLIMPSE, 70 μ m image (Hi-Gal) and ATLASGAL 850 μ m image . From top to bottom: HII region, UCHII region, PN, radio-star, radio-galaxy and infrared-quiet sources. CORNISH radio images are 80'' by 80''; GLIMPSE images are 100'' by 100''; HI-GAL and ATLASGAL images are 180'' by 180''.

In its most complete form, the source function must include the radiation scattering effects and is written as $S_\nu = (j_\nu + \sigma_\nu J_\nu)/(\kappa_\nu + \sigma_\nu)$, where j_ν and κ_ν are the emission and absorption coefficients and σ the scattering coefficient which must be treated separately from the emission because, out of thermodynamic equilibrium, its spectrum differs from the S_ν spectrum of spontaneous emission.

In local thermodynamic equilibrium, Kirchhoff's Law states that $j_\nu = \kappa_\nu B_\nu(T)$ and therefore the propagation medium behaves like a blackbody and the source function can be approximated by the Planck's law, as given in equation 1.5:

$$B_\nu = \frac{2h\nu^3}{c^2} \frac{1}{e^{h\nu/kT} - 1} \quad (1.5)$$

In the absence of radiation from external sources, radiative transfer has the general solution:

$$I_\nu = S_\nu[1 - e^{-\tau_\nu}] \quad (1.6)$$

which shows that the intensity of the observed radiation is the result of the emission of the source S_ν minus the attenuation suffered along the optical path traveled, represented by the product $S_\nu e^{-\tau_\nu}$. In the radio domain, the Planck's law can be replaced by the Rayleigh-Jeans approximation (where $h\nu \ll kT$, therefore the emission is controlled by the temperature), given by equation 1.7.

$$B_\nu(T) = \frac{2hT\nu^2}{c^2} \quad (1.7)$$

The flux density can then be expressed as equation 1.8, where F_ν is in units of Jansky (Jy) and Ω is the solid angle measured in steradians.

$$F_\nu = \frac{2\kappa_\nu\nu^2\Omega}{c^2} T_b \quad (1.8)$$

1.5.2 Bremsstrahlung emission

Bremsstrahlung emission is important for the study of HII regions because it is the dominant radiative process at radio frequencies in diffuse and ionized nebulae. Also known as free-free radiation, it is produced as a result of the interaction between an electron and an ion. It occurs

when free electrons in the plasma are deflected from their original paths by the positive ions in the gas as they enter the zone of action of their electric field (Lawrence et al. 1991). This is a thermal emission, which means it is controlled by the temperature of the ionized gas, such that electrons move at thermal speeds.

Since both interacting particles are free, their energy states are not quantized and the process can be treated classically. In this treatment the photon produced in the electron-ion interaction has energy $h\nu \ll kT$ (T is the temperature of the radiating source) and the Planck's law in equation 1.5 can be replaced by the Rayleigh Jeans approximation in equation 1.7.

Optical Depth

The optical depth of an ionized region is the distance over which a photon can travel before been absorbed. It is the integral of the opacity, along the line of sight:

$$\tau_\nu = \int -\kappa_\nu ds \propto n_e \quad (1.9)$$

Optical depth can also be expressed in terms of the emission measure (EM), equation 1.10 and can be approximated numerically by equation 1.11 (Mezger and Henderson 1967), thus $\tau_\nu \propto \nu^{-2.1}$:

$$\tau_\nu \approx 3.014 \times 10^{-2} T_e^{-3/2} \nu^{-2} EM \langle g_{ff} \rangle \quad (1.10)$$

$$\tau_\nu = 8.235 \times 10^{-2} T^{-1.35} \nu^{-2.1} EM \quad (1.11)$$

where g_{ff} is the free-free gaunt factor, presented in equation 1.12 and $EM = \int_0^s n_e^2 ds$ is given in pc cm^{-6} .

$$\langle g_{ff} \rangle(\nu, T_e) \approx \ln[4.955 \times 10^{-2} \nu^{-1}] + 1.5 \ln(T_e) \quad (1.12)$$

At low frequencies where $\tau_\nu \rightarrow \infty$ (the optically thick regime) the spectrum of the free-free emission can be approximated by a blackbody, such that the free-free emission will increase

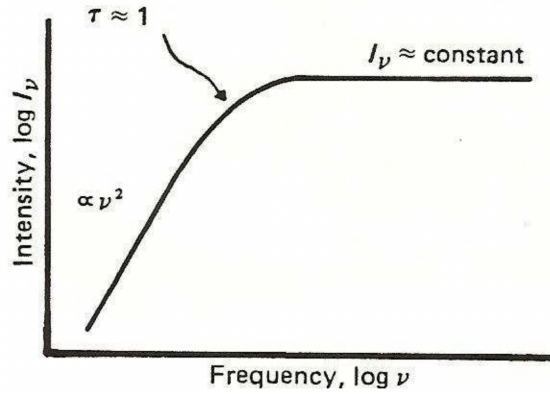


Figure 1.8 Free-free thermal emission spectrum at low frequencies, typical of HII regions (Longair 1992)

with increasing frequency as ν^2 (Burke et al. 2019).

$$F_\nu = \frac{2\kappa\nu^2\Omega}{c^2}T_e \propto \nu^2 \quad (1.13)$$

At high frequencies, where $\tau_\nu \rightarrow 0$ (the optically thin regime), the nebulae is nearly transparent and shows little dependence on frequency, such that the free-free emission does not change much with frequency.

$$F_\nu = \frac{2\kappa\nu^2\Omega}{c^2}T_e \propto \nu^{-0.1} \quad (1.14)$$

The two situations described above are represented by the graph in figure 1.8.

1.6 Interferometry

The spatial resolution of a telescope is set by its diameter (Equation 1.15). The larger the diameter of the telescope the higher the spatial resolution. However, there are physical limitations to how large a single radio telescope can be built, consequently at radio astronomy it is not practical to achieve sub-arcsecond resolution with single dishes (Ryle 1968).

$$\theta = \frac{1.22\lambda}{D} \quad (1.15)$$

To overcome these limitations, astronomers needed to build radio interferometers, arrays of small telescopes that are combined together to synthesize a larger aperture telescope (Ryle 1955). The resolution of an interferometer is defined by the distance between the telescopes,

rather than the size of the single dish, in this case, the diameter of the telescope, D , in equation 1.15 becomes the largest distance between the telescopes (the largest baseline).

The brightness distribution of the observational target is not directly measured. Instead, an interferometer measures the unique function of the source brightness, called complex visibility, $V(u,v)$. This visibility is a function of time and baseline coordinates (u,v) produced by pairs of antennas at specific frequencies (Wilson et al. 2009). The definition for the visibility function is given in the equation below:

$$V_\nu(u, v) = \int \int I_\nu(l, m) e^{-2\pi i(ul+vm)} dl dm \quad (1.16)$$

where (l, m) are the sky coordinates and (u, v) are the baseline coordinates. The baseline coordinates define the Fourier transform plane of the angular distribution of the target on the sky. The intensity distribution I_ν is derived inverting the integral through a Fourier transform by the Van Cittert-Zernike theorem (Thompson 1989), expressed as equations 1.17 and 1.18.

$$V_\nu(u, v) \rightarrow F \rightarrow I_\nu(l, m) \quad (1.17)$$

$$I_\nu(l, m) = \int \int V_\nu(u, v) e^{-2\pi i(ul+vm)} du dv \quad (1.18)$$

This represents an ideal case, in which the interferometer and Earth's rotation are employed to obtain the source visibilities equivalent to an observation from a single dish of diameter equal to the interferometer baseline. However, in practical terms radio interferometry observations leave gaps in the u - v plane coverage due to the spacing between the individual antennas. These gaps result in the so called dirty image (equation 1.19), which is the convolution of the true image and the dirty beam (equations 1.20 and 1.21). This introduces the u - v plane sampling function, $S_{(u,v)}$ (equation 1.22) (Briggs et al. 1999).

$$I_{\nu,D}(l, m) = \int \int V_\nu(u, v) S_{(u,v)} e^{-2\pi i(ul+vm)} du dv \quad (1.19)$$

$$S_{(u,v)} V_{(u,v)} \rightarrow F \rightarrow I_{\nu,D}(l, m) \quad (1.20)$$

$$I_{\nu,D}(l, m) = I_{\nu(l,m)} * s(l,m) \quad (1.21)$$

$$s_{\nu}(l, m) = \int \int S_{(u,v)} e^{-2\pi i(ul+vm)} dudv \quad (1.22)$$

When $S_{(u,v)}$ is 1 there are data and when it is zero refers to other parts of the u-v plane where there are no sampled points. The more filled the u-v coverage, the better the image will be. The sample points of the visibilities can be increased by observing for a long time, because this will allow the Earth's rotation to fill in the gaps of the u-v coverage.

To reduce the dirty beam artefacts and recover the true image the common algorithm CLEAN by Högbom (1974) is applied. The CLEAN algorithm consists of assuming the image to be a field of point sources defined by positions and peak strength. After that it finds the brightest point in the dirty map and subtracts the dirty beam from this position until a satisfactory image is obtained. The remaining peaks are called clean components. The clean components are convolved with a restoring beam and added to the residual image and the resulting map estimates the sky brightness in Jy/beam.

1.7 Motivation and Thesis Outline

In this work, the CORNISH-South survey is used to investigate the ultra-compact HII region population in the southern Galactic plane. The CORNISH-South survey is the largest complete, well-selected, and unbiased sample of candidate UCHII regions to date in the southern Galactic plane. The findings from this work, should improve what is known about the UCHII regions and guide future theoretical models to better represent the properties of the massive stars in our galaxy.

The rest of the thesis is organized as follows:

- In chapter 2, the calibration and imaging process of the high resolution observations of the unresolved CORNISH-South UCHII regions is presented.
- In chapter 3, the observational and derived physical properties of the 255 CORNISH-South UCHII regions candidates are analyzed together with the estimated spectral indices to verify the nature of these sources, and a catalogue with final classification is presented.

- In chapter 4, this work is summarized and recommendations for future work are proposed.

Chapter 2

High Resolution Observation of Unresolved CORNISH-South UCHII regions

2.1 Introduction

The CORNISH-South survey has delivered the first high-resolution radio survey of the southern Galactic plane at 5 and 9 GHz. A sample of 255 UCHII regions out of the nearly 5000 sources detected have been visually identified using multi-wavelength survey data. The CORNISH-South candidates were classified by the inspection of the visual appearance of the UCHII regions at different wavelengths over which UCHII regions emit. In this chapter, the first follow-up at higher resolution of the 72 UCHII regions that were not sufficiently resolved by 2.5" 5.5 GHz or 1.5" 9 GHz survey observations is presented. ATCA 6 km array observations at 16.7 and 22.4 GHz (here after 17 and 22 GHz) with resolutions of 0.75 and 0.55 were done with the main objective of revealing the morphologies of the vast majority of the targets. These most compact, and youngest, UCHII regions targeted are of key importance as they are still close to their birth site and environment and hold the best clues to unravelling massive star formation.

The reduction, the imaging process and measurement of the properties of the higher resolution follow-up observations are presented in this chapter. With the available 17 and 22 GHz flux measurements of the target sources, spectral indices from 17 to 22 GHz were obtained and are also presented.

2.2 Observation set-up

The follow-up survey of the southern Galactic plane was observed with the ATCA array, using the maximum 2GHz bandwidth of the CABB correlator. 6km array observations at 17 and 22 GHz of the 72 unresolved CORNISH-South UCHII regions were carried out to provide resolutions of 0.75" and 0.55" respectively. Observations were carried out with all six antennas of the array between 02/04/2022 and 11/04/2022. The maximum antenna baseline for this configuration is 6 km, and the number of baselines is 15. The targets were observed for 20 minutes total on- source time expecting a noise level of 80 μ Jy/beam. Blocks of 12 sources were observed alternating between 2 minutes on-target and 1 minute on the phase calibrator, which together with overheads and hourly pointing correction required 50 minutes per block. To achieve an optimum uv-coverage these blocks were repeated twelve times over a full track, this provided the total on-source time required. Therefore to complete the block including set-up time, flux and bandpass calibration 12 hours were needed. Six of these blocks covered the full sample of 72 targets (six days of observations), so 72 hours were spent in total.

The sources targeted have peak fluxes at 9 GHz ranging from about 1 to 30 mJy per 1.52" beam. This translates to a minimum average surface brightness of about 250 μ Jy per 0.75" beam at 17 GHz assuming a flat spectrum. Most of the targets were expected to be much brighter than this. The 20 minutes on source time was predicted to give a noise level of 80 μ Jy per beam. The second frequency of 22 GHz was selected additionally to deploy a zoom window on the water maser line at 22.235 GHz. Many UCHII regions have associated water maser emission which can be used for additional phase calibration of the continuum.

The observations are spread over a bandwidth of 2048 MHz, consisting of 2048 channels, each of 1 MHz. The observation parameters described in this section are summarized in table 2.1.

2.3 Data Flagging and Calibration

The data comprising 6 blocks of observations were flagged, calibrated and imaged with the Multichannel Image Reconstruction Image Analysis and Display (MIRIAD) software (Sault et al. 1995) by utilising the semi-automated calibration and imaging pipeline developed for the CORNISH survey by Purcell¹. The pipeline was written in python and was used directly to interface with the MIRIAD. All flagging and calibration parameters were determined manually

¹https://github.com/crpurcell/CORNISH-S-PIPELINE/blob/master/2_cal0bsDay.py

Table 2.1 Summary of observational parameters.

Parameters	Value
Observing frequency	16.7GHz & 22.4GHz
Observing period	02/04/2022 - 11/04/2022
Number of antennas	6
Number of baselines	15
Longest baseline	6 km
Size of single dish	22m
Sensitivity	0.08 mJy/beam
Bandwidth	2048 MHz
Channels	2048
Expected noise level	80 μ Jy
Synthesized beam	0.75" & 0.55"

for each block and then were put into a configuration file, such that the parameters were automatically applied when the pipeline was run.

Within the whole process (flagging, calibration and imaging) each 12 hours observation was treated separately. The raw data were converted to a MIRIAD format using the ATLOD task. For CABB data, a number of channels are affected by self-generated interference from the 640 MHz CABB clock and the ATLOD task flags these channels of the data. It also flags out 4.9% of channels on each band edge, which corresponds to 100 channels for CABB's 2048 channel spectra. ATLOAD also automatically flag out frequency bands that are known to be heavily affected by RFI and corrects the measured XY phase of the ATCA.

The uv-coverage, and the phase and amplitude variations with time were visually inspected for each block of observation before any flagging or calibration was done. This inspection allowed the identification of poor uv coverage and/or times with bad visibilities, ensuring that the data are RFI free and that no data has been flagged unnecessarily.

Each of the six blocks of observations presented very few flagging demands, with the fluctuation channels being the ones that show water maser detection and very few affected by actual RFI. As mentioned earlier most of the UCHII regions in our sample have associated water maser emission and they were localized in specific known channels. The channels with masers, RFI and another bad channels were flagged in both the frequency and time domain.

The 10 secondary calibrators listed in table 2.2, were used in the CORNISH-South follow-up observations to correct for fluctuations in the phase and amplitude due to atmospheric and instrumental effects. The phase calibrators were chosen so that they are less than 10° away from the sources, and the blocks were grouped in order to have the sources close to each other.

Table 2.2 Phase calibrators for each block of observations and the longitude range.

Calibrator	Obs. Block	Obs. Day
1414-59	1	02/04/2022
j1534-5351	1	02/04/2022
1616-52	2	04/04/2022
1646-50	2 & 3	04/04/2022 & 06/04/2022
j1631-4345	3	06/04/2022
1717-358	4	07/04/2022
1714-397	4 & 5	07/04/2022 & 10/04/2022
j1222-6035	6	11/04/2022
j1322-6532	6	11/04/2022
1352-63	6	11/04/2022

For the days with two secondary calibrators, calibration was done separately and the solutions combined. 1934-638 was used as the primary flux and bandpass calibrator. An additional bandpass calibrator (0537-441 for 4 blocks and 1253-055 for two blocks) was also observed, at the beginning of each observation, used for setup including delay calibration. The gain solutions in phase and amplitude and the visibilities after calibration were inspected before moving to the imaging stage.

The work flow for the calibration process that is implemented in the pipeline is presented in Figure 2.1 This is used in Irabor, Hoare, Burton, et al. (2023) for all CORNISH-South sources and was adapted from the calibration of the CORNISH-North dataset using AIPS (see Purcell et al. 2013).

2.4 Imaging

The calibrated target fields were split into individual sources and then imaged interactively with MIRIAD. To account for the spectral index variation across the bandwidth during the deconvolution process the imaging was executed using multi-frequency synthesis in MIRIAD (Perley et al. 1999). To remove the artefacts from the dirty beam, deconvolution was performed using the MFCLEAN task. Each image was cleaned down to a conservative threshold of 0.1 mJy in 22GHz and 0.08 in 17GHz, the exact value was determined depending on the individual noise level of each field. The variation in cleaning thresholds was kept small to preserve homogeneity as much as possible, while also aiming to produce individual maps of high quality. Interactive cleaning was performed whenever necessary, to remove artefacts resulting

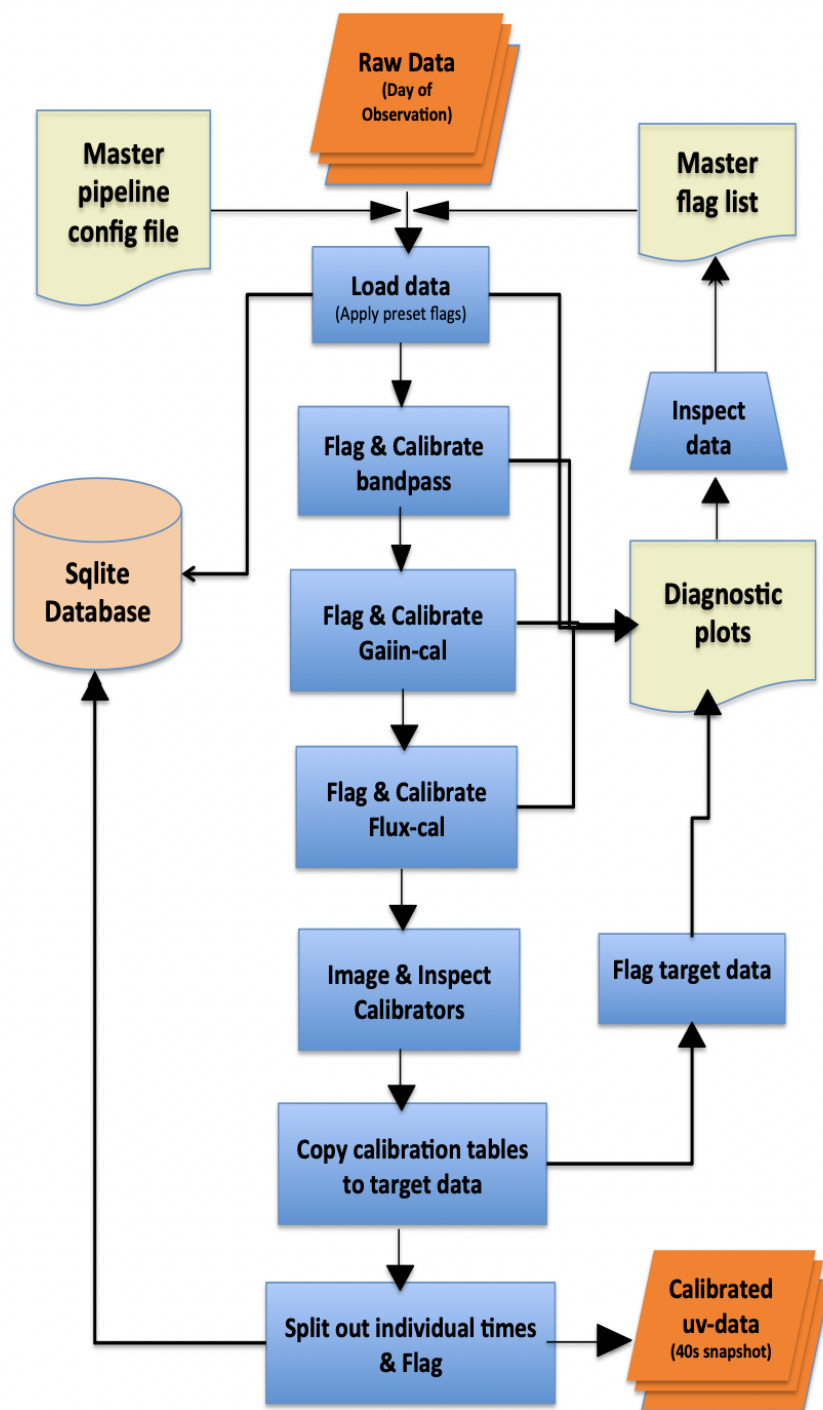


Figure 2.1 Work flow of the calibration pipeline adapted from the CORNISH-North calibration pipeline taken from Irabor, Hoare, Oudmaijer, et al. 2018

from bright sources in the primary beam. The dirty beam were created using the robust weighting scheme also called Briggs weighting (Briggs et al. 1999), with a robustness parameter of 0.5. This was chosen to provide an improved sensitivity without sacrificing the resolution (Irabor, Hoare, Oudmaijer, et al. 2018).

Table 2.3 Comparison of tabulated fluxes by ATCA (third column) and newly measured (last two columns) calibrator fluxes.

Calibrator	RA (J2000)	DEC (J2000)	Catalogued Flux at 17 GHz (Jy)	F_{17GHz}	F_{22GHz}
1414-59	14:17:41.640	-59:50:37.53	0.631 ± 0.005	0.395 ± 0.0005	0.362 ± 0.0004
j1534-5351	15:34:20.660	-53:51:13.425	1.481 ± 0.013	0.751 ± 0.001	0.766 ± 0.001
1616-52	16:20:17.840	-52:09:26.55	0.387 ± 0.014	0.417 ± 0.0001	0.322 ± 0.0003
1646-50	16:50:16.635	-50:44:48.37	1.071 ± 0.013	1.028 ± 0.001	1.153 ± 0.001
j1631-4345	16:31:37.935	-43:45:25.238	0.502 ± 0.014	0.405 ± 0.0004	0.289 ± 0.0004
1717-358	17:20:21.804	-35:52:47.708	0.602 ± 0.016	0.5269 ± 0.001	0.349 ± 0.003
1714-397	17:17:38.598	-39:48:52.586	0.432 ± 0.011	0.438 ± 0.001	0.302 ± 0.0003
j1222-6035	12:22:06.268	60:35:32.282	0.453 ± 0.013	0.470 ± 0.0002	0.432 ± 0.0002
j1322-6532	13:22:53.888	-65:32:19.892	0.444 ± 0.01	0.481 ± 0.0003	0.299 ± 0.002
1352-63	13:55:46.632	-63:26:42.62	0.625 ± 0.014	0.677 ± 0.0003	0.545 ± 0.0002

A cell size of $0.1''$ and an image size of 2048×2048 were chosen for the whole dataset and it was found to be appropriate for the targets. The field of view was then $205''$ which is bigger than the primary beam.

With the purpose of quality checking of the calibration and imaging process, images of the secondary calibrators were first inspected and their fluxes were measured to compare with the cataloged fluxes. The images are presented in figure 2.2 and 2.3, and they showed no jets or extended emission, so there was no need to perform self calibration. The comparison between the cataloged fluxes of the calibrators and the newly measured is presented in table 2.3, and the results are comparable, i.e., the fluxes of the observed phase calibrators are obviously not the same, because these sources are time variable. But most of them are flat at 17GHz and few of them are less by approximately a factor of two.

2.5 Target detection statistics

The dataset covers 72 previously unresolved CORNISH-South UCHII regions observed in two different frequencies (17 GHz and 22 GHz).

36 of the observed targets remain Gaussian sources in both 17 GHz and 22 GHz, 23 targets are extended sources in both frequencies and 7 targets are extended sources in only one of the frequencies.

All targets, except two sources in 17 GHz and four sources in 22 GHz were successfully detected and imaged, the exceptions being G338.5660+0.1096 and G305.7980-0.2415 at 22 GHz and G338.3250+0.1547 G350.1110+0.0882 at both 17 GHz and 22 GHz.

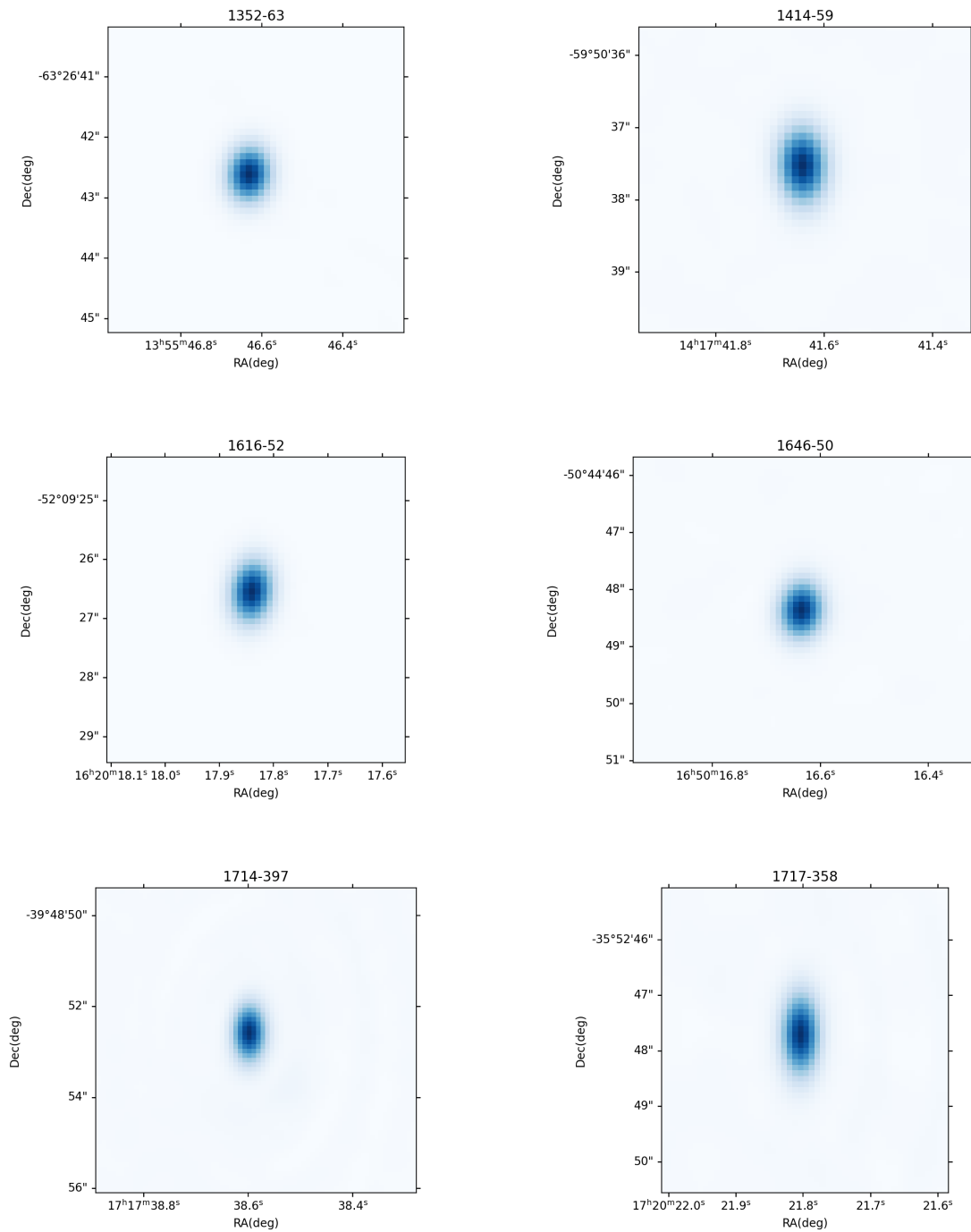


Figure 2.2 Images of the secondary calibrators at 17 GHz.

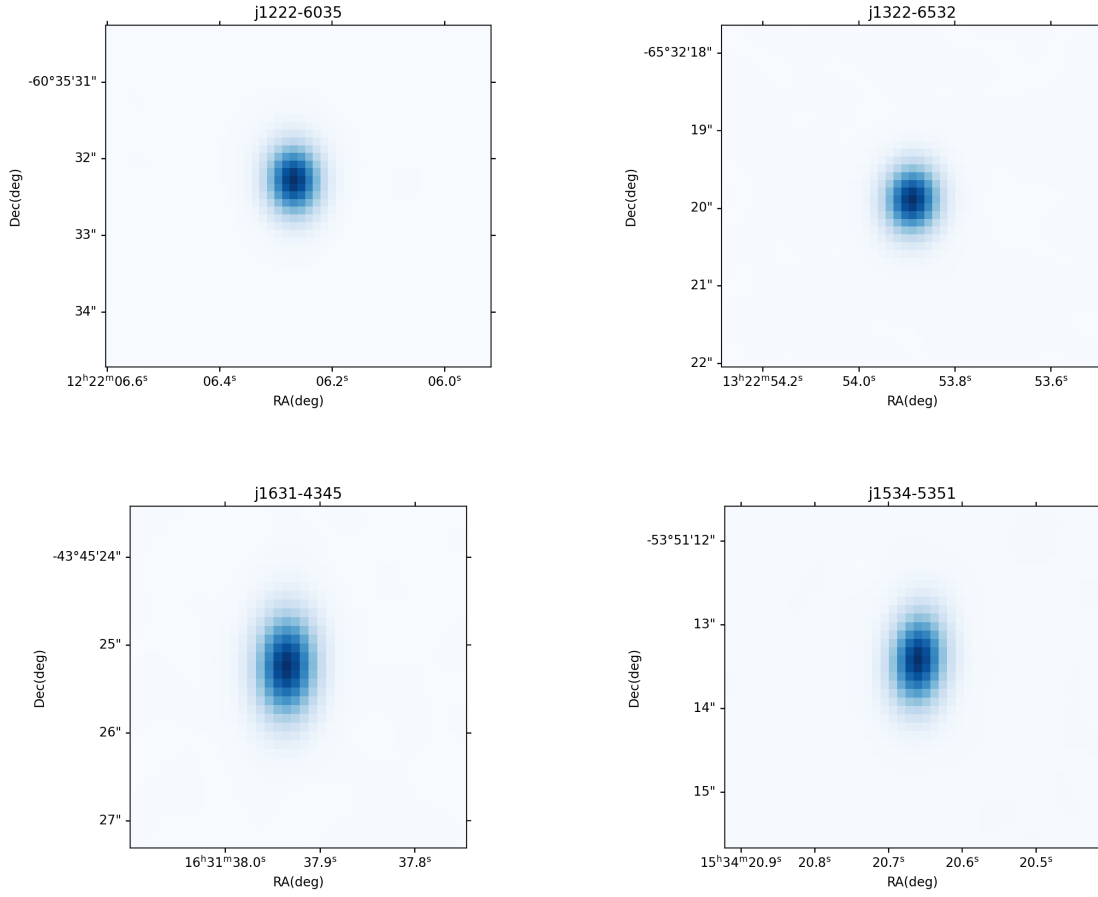


Figure 2.3 Secondary calibrators, continued.

One of the observed targets (G314.2200+0.2727) appear at the higher resolution to be clearly a merged three sources. The three merged sources that compose G314.2200+0.2727 at the higher resolution here after G314.2200+0.2727A, G314.2200+0.2727B and G314.2200+0.2727C, appear to be unresolved in 17 GHz and extended in 22 GHz. And three of the observed targets (G329.8150+0.1407, G344.5820-0.0238 and G349.7210+0.1213) at the higher resolution appear to be merged pairs of sources.

From the cross-match between the 72 unresolved CORNISH-South UCHII regions and the HOPS survey sources by Walsh, Breen, et al. (2011), performed before the observations it was already known that 22 of the observed targets have water masers associated, and it could be seen during the observations with the high amplitude observed at the specific channels that contains the masers. Water masers are thought to be associated with molecular outflows (Tofani et al. 1995)

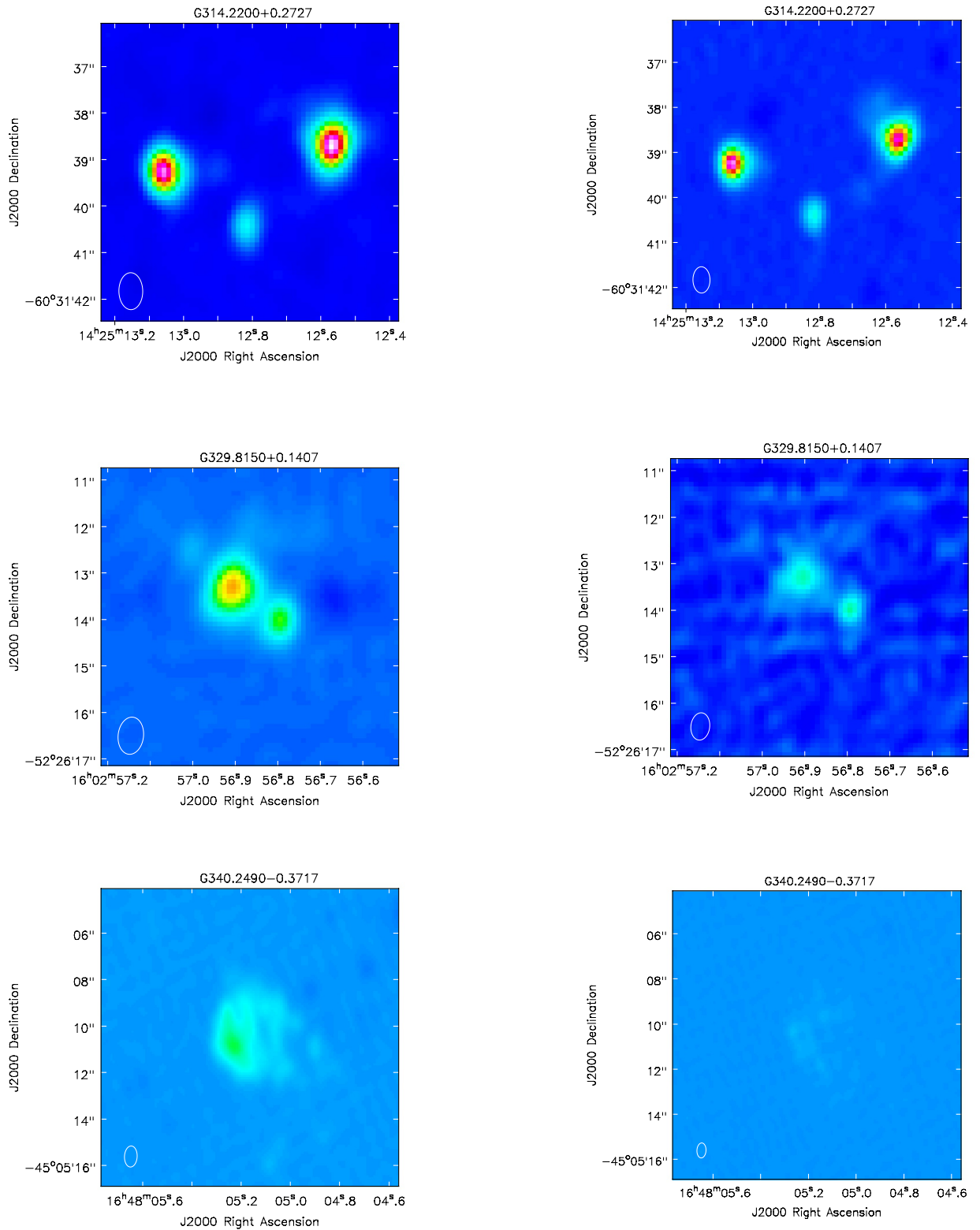


Figure 2.4 | Examples of the observed maps. At the left are presented sources observed in 17GHz and at the right are presented sources observed in 22 GHz. From the top to the bottom are presented the sources that appear at higher resolution to be merged three sources, merged two sources and that present an extended cometary morphology respectively

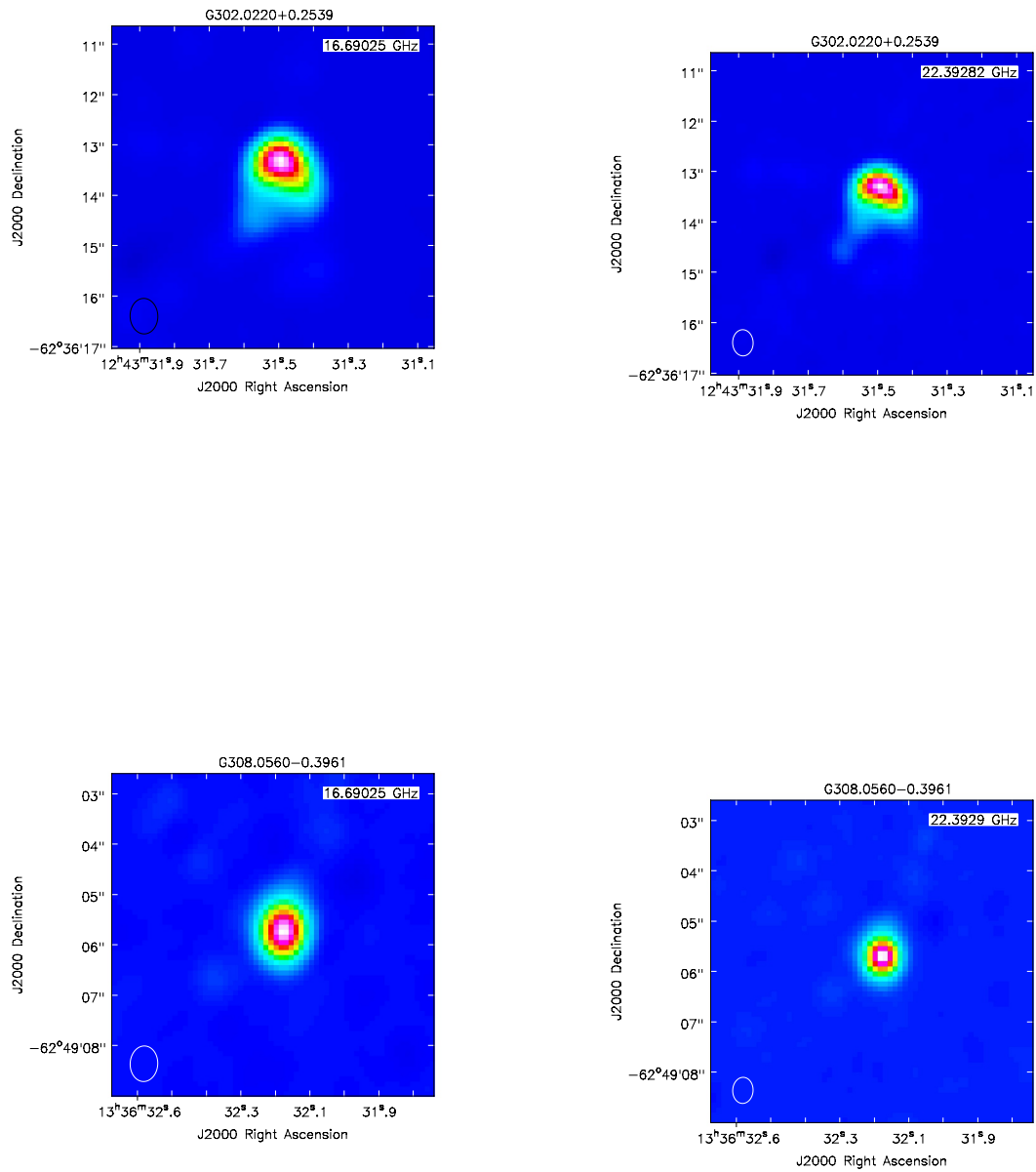


Figure 2.5 | Continued from previous figure. From the top to the bottom an example of a compact cometary source and unresolved source

All source maps are presented in figure A.1, A.2, A.3, A.4, A.5, A.6, A.7 and A.8 for both frequencies, and some examples are presented in figure 2.4 zoomed in at the relevant source. These images were chosen as examples because they are representative of the scenario that is

verified with all the data. With some of the maps being unresolved in 17 GHz and extended in 22 GHz (first example), some sources being split into multiple sources (second example), some sources showing extended cometary morphology in 17 GHz and being over-resolved in 22 GHz (third example), some showing more compact cometary morphology in both frequencies (fourth example) and some sources being unresolved in both frequencies (last example).

2.6 Properties of the detected sources

The observed properties of the detected sources such as positions of the source centres, integrated and peak fluxes, the source major- and minor-axis length and position angle were derived with CASA (Common Astronomy Software Applications). For point sources a 2D Gaussian fit was used through the `imfit` task and all the mentioned properties were displayed by the software. For extended sources a polygon was drawn manually around the sources with CASA to measure the physical properties. 38% of the sample was described by such polygons at 17 GHz and 40% at 22 GHz and this information is summarized in table 2.4.

The angular diameter (here after angular size) for Gaussian sources is the geometric mean of the measured deconvolved major- and minor-axis. It was calculated using equation 2.1 and the associated errors were calculated using equation 2.2.

$$\theta_{mean} = \sqrt{\theta_{maj}\theta_{min}} \quad (2.1)$$

$$\sigma(\theta_{mean}) = \frac{\theta_{mean}}{2} \sqrt{\frac{\sigma^2(\theta_{maj})}{\theta_{maj}^2} + \frac{\sigma^2(\theta_{min})}{\theta_{min}^2}} \quad (2.2)$$

For extended sources the angular sizes were calculated using the number of pixels in the source, region which is shown when a polygon is manually drawn. This number is multiplied by the size of each pixel to determine the area within the contours, and from there an equivalent circular diameter is determined using $A = \frac{\pi d^2}{4}$.

The derived properties of the CORNISH-South sample estimated in this section are, the brightness temperatures and the optical depth. The brightness temperatures were calculated using equation 2.3

$$T_b = \frac{1.222 \times 10^3 S_\nu}{\nu^2 \theta^2} \quad (2.3)$$

Table 2.4 | Summary of the UCHII region detection above the 7σ limit.

	17 GHz	22 GHz
Number of Gaussian sources	42	38
Number of polygonal sources	28	29
Number of not detected sources	2	4

where ν is the frequency in GHz, S_ν is the flux density in mJy, T_b is the brightness temperature in K and θ is the deconvolved size of the source in arcsec. Given the equation, for the unresolved sources the brightness temperature shows a lower limit instead of the actual value. This property can be used as a way of measuring the optical thickness of the source, τ_ν , by using equation 2.4 assuming $T_e = 10^4 K$, and therefore give us clues to infer the age of the UCHII region.

$$T_b = T_e(1 - e^{-\tau_\nu}) \quad (2.4)$$

With larger thickness the brightness temperature increases, and it may reach the electron temperature of the ionised regions in the optically thick limit. Lower values of the brightness temperature indicate optically thin sources, and therefore the brightness temperature decreases with the expansion of the UCHII regions. In short, more evolved and optically thin UCHII regions should have lower brightness temperatures compared to younger and more compact UCHII regions.

2.6.1 17 GHz properties

The integrated flux distribution presented in figure 2.6a shows a similar distribution compared to the 5 GHz CORNISH-South UCHII regions (Irabor, Hoare, Burton, et al. 2023). The faintest source has a flux density of 1.89 mJy and the brightest source a flux of 0.86 Jy, with the distribution peaking at ~ 7.9 mJy. The higher resolution follow up picked up more faint sources compared to the CORNISH-South 5 GHz, as expected due to the sensitivity being better. The distribution of the deconvolved angular sizes presented in figure 2.6b peaks towards unresolved sources at approximately $0.25''$. The definition of resolved and unresolved sources is based on the observations restoring beam size at 17 GHz which is $0.75''$ and the mean error of the angular size which is $0.06''$, therefore, all UCHII regions with angular sizes less than $0.81''$ are defined as unresolved sources ($\sim 56\%$). Resolved sources account for 42% of the sample, which $\sim 87\%$ are polygonal.

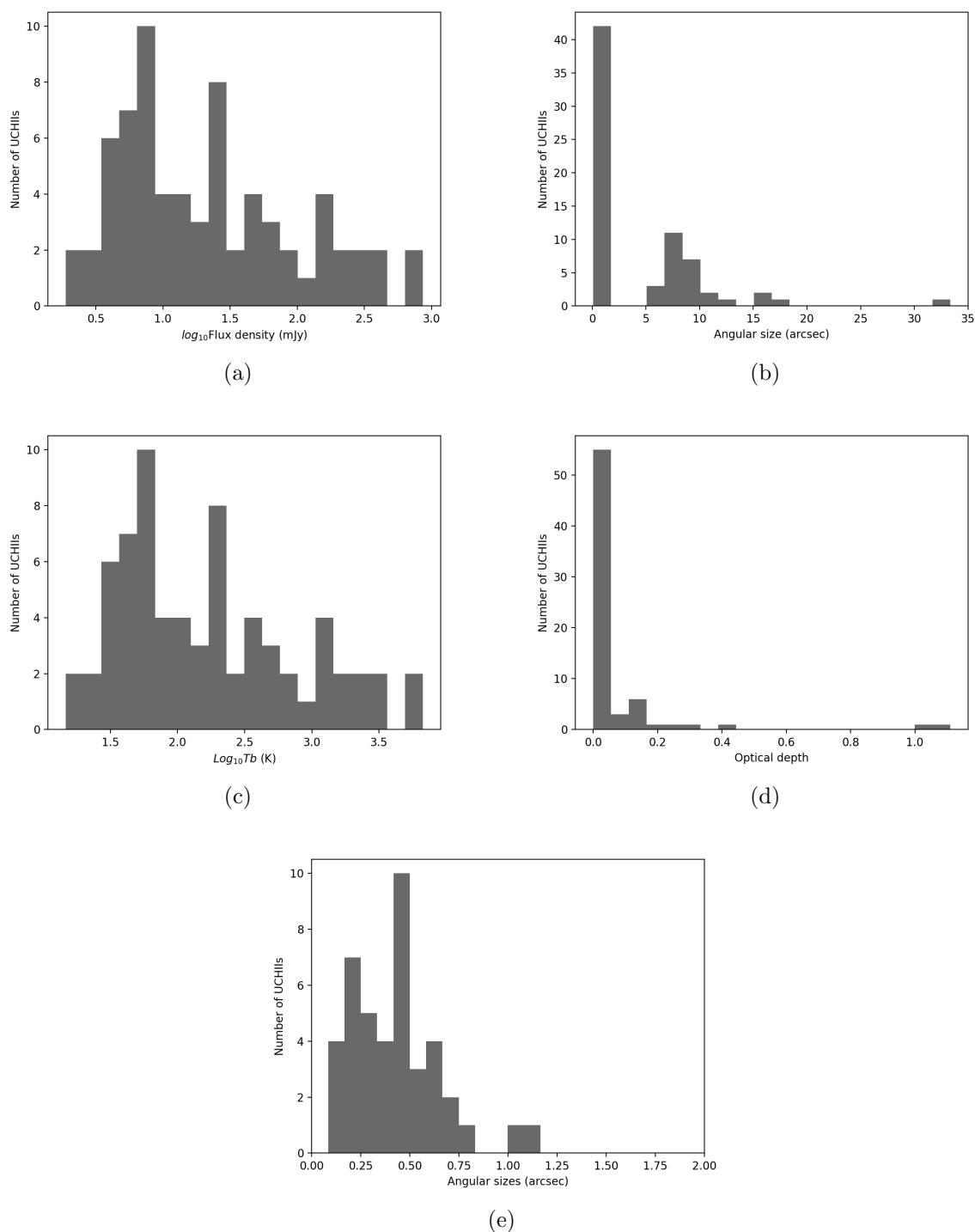


Figure 2.6 Histograms of the observational properties, brightness temperatures and optical depths for the high resolution sample at 17 GHz.

As mentioned in section 2.5 the physical properties were estimated by fitting a Gaussian in 42 sources out of the 72 UCHII regions, for these sources the angular sizes vary from $0.08''$ to $1.45''$. For the remaining 28 sources a polygon was drawn instead, and for these sources the angular sizes vary from $5.3''$ to $33.3''$. The deconvolved angular size distribution presented in figure 2.6b was

zoomed in no show details in the range of $0''$ to $2''$, which is where most of the sources are confined in, and the histogram is presented in figure 2.6e. The large angular size of $33.3''$ verified in the extended sources corresponds to G330.2950-0.3929, which is a merged multiple sources. For this source and the other four merged multiple sources (G314.2200+0.2727, G329.8150+0.1407, G344.5820-0.0238, G349.7210+0.1213) a measurement of the individual source properties (flux density and angular size) was separately performed and is presented in table A.5.

The brightness temperature and the corresponding optical depth distribution are presented in figure 2.6c and 2.6d respectively. The brightness temperature distribution varies from ~ 15 K to ~ 6704 K with a median of ~ 139 K. The optical depth distribution ($\tau \ll 1$ for the majority of the sources) shown in figure 2.6f is showing that the sample is dominated by optically thin UCHII regions. The radio properties from this section are presented in Table A.1.

2.6.2 22 GHz properties

The flux density of the 22 GHz CORNISH-South UCHII regions is presented in figure 2.7a. The histogram shows similar distribution compared to the 17 GHz sample, peaking slightly at lower value of flux density (6.9 mJy) and varying in a range of 1.4 mJy to 749 mJy.

The distribution of the angular sizes in 22 GHz (presented in figure 2.7c) (with a zoom in for $0'' \leq \theta \leq 2''$ presented in figure 2.7e) does not have much difference with the distribution in 17 GHz as well, being dominated by unresolved sources and peaking towards $0.2''$. Based on the beam size at 22 GHz, which is $0.55''$, and the mean error of the angular sizes, which is $0.05''$, sources with angular sizes less than $0.6''$ are defined as unresolved sources. unresolved sources account for $\sim 43\%$ of the sample, and all of them are Gaussian sources. The 22 GHz UCHII regions sample is composed of 39 Gaussian sources (with angular sizes varying from $0.1''$ to $1.7''$), 29 polygonal sources (with angular sizes varying from $2.62''$ to $33.45''$) and the remaining 4 sources were not detected. As explained in the previous section, the large angular size of $33.45''$ corresponds to G330.2950-0.3929, which is a merged multiple sources. And the same treatment is given to the 22 GHz observed properties (flux density and deconvolved angular size), they have been calculated for the individual sources that compose the merged sources and are presented in table A.5.

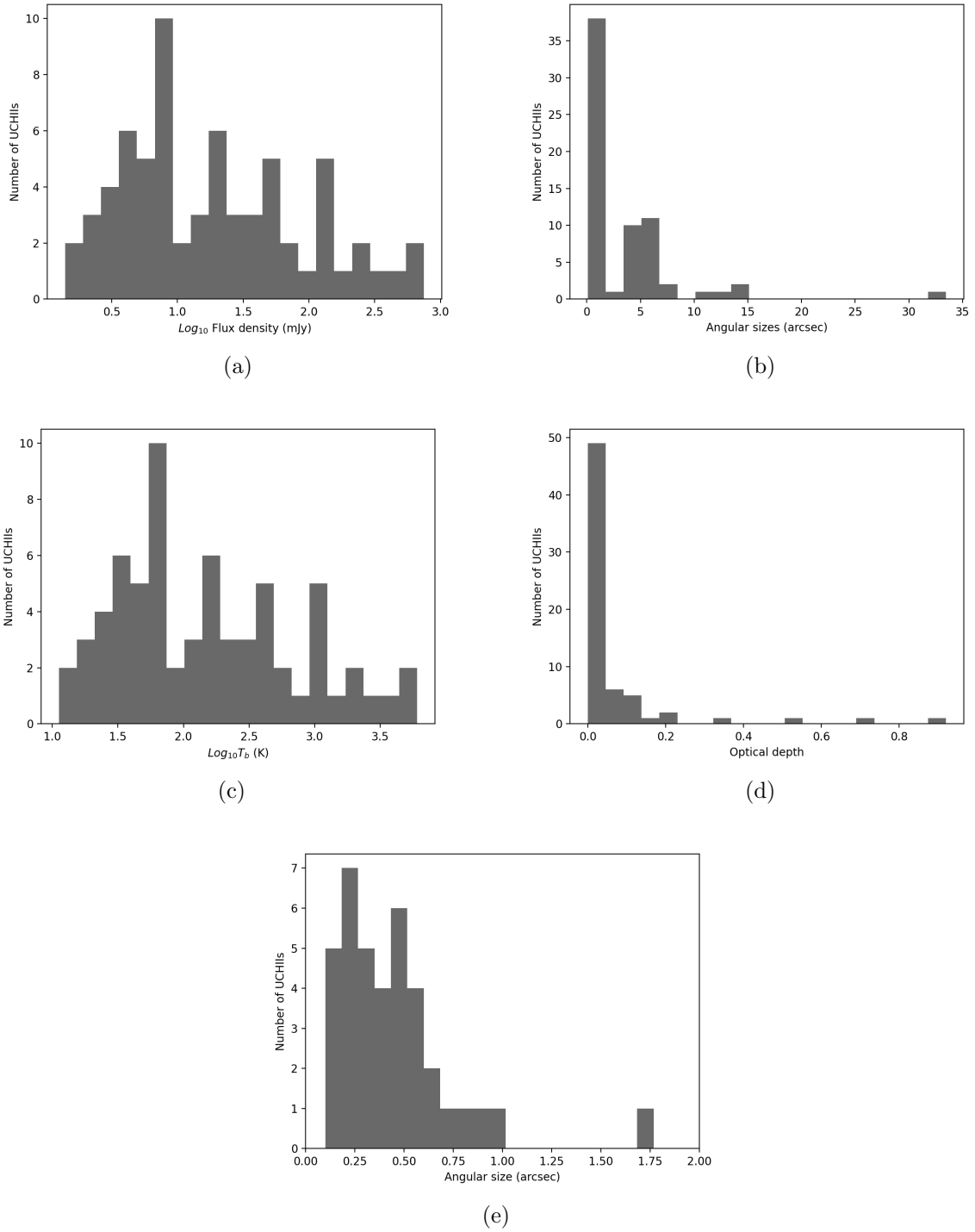


Figure 2.7 Histograms of the observational properties, brightness temperatures and optical depths for the CORNISH-South UCHII regions at 22 GHz.

The brightness temperature and the corresponding optical depth distribution are presented in figure 2.7c and 2.7d respectively. The brightness temperature distribution varies from ~ 11 K to ~ 6024 K with a median of ~ 130 K and the optical depth for the majority of the sources is less than 0.2, showing the sample being dominated by optically thin sources.

2.7 22GHz-17GHz spectral indices

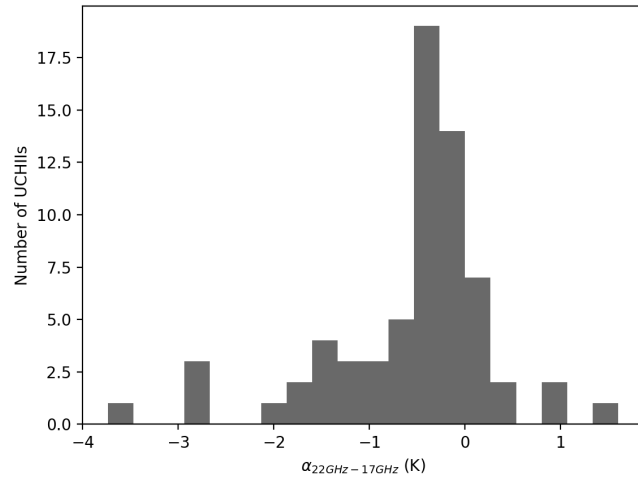
To further prove the nature of the radio emission of the presented sample of UCHII regions spectral indices from 22-17 GHz were calculated. The spectral indices and the associated errors of the sample of 68 CORNISH-South UCHII regions were estimated using equations 2.5 and 2.6, where S_1 and S_2 are the flux densities in mJy at 22 GHz and 17 GHz, respectively.

$$\alpha = \frac{\ln(S_1/S_2)}{\ln(\nu_1/\nu_2)} \quad (2.5)$$

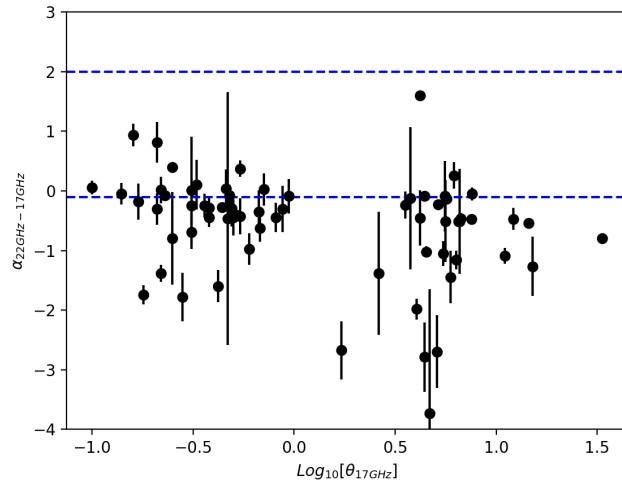
$$\Delta\alpha = \frac{1}{\ln(\nu_1/\nu_2)} \sqrt{\left(\frac{\sigma S_1}{S_1}\right)^2 + \left(\frac{\sigma S_2}{S_2}\right)^2} \quad (2.6)$$

For the four not detected UCHII regions at 22 GHz ($G305.7980 - 0.2415$, $G338.3250 + 0.1547$, $G338.5660 + 0.1096$ and $G350.1110 + 0.0882$), it was not possible to estimate the spectral index, therefore, the flux upper limit was calculated and is included in tables 2.5 and 2.6, which present estimated fluxes and calculated 22GHz-17GHz spectral indices of the whole sample. For the purpose of analyzing the 22GHz-17GHz spectral indices, the histogram of its distribution is presented in figure 2.8, together with the plot of the spectral indices as a function of their corresponding angular sizes.

The radio continuum emission observed towards UCHII regions is theoretically expected to be free-free interaction, and therefore, the spectral index range is expected to be between -0.1 and 2, that is between the optically thin and optically thick limit. Although the lower limit of the spectral index for thermal emission is -0.1, errors must be taken into account in the analysis of the results. And for this the mean error of the spectral index (~ 0.4) is considered. The histogram of the CORNISH-South UCHII regions spectral indices presented in figure 2.8a shows a peak of ~ -0.1 , which agrees with optically thin sources. Figure 2.8 clearly shows that the majority of the sample ($\sim 69\%$) has spectral indices within the theoretical range. And 21 sources are found below limit (taking errors into account), which is indicative of non-thermal emission. The reason for the apparently non-thermal emission is likely to be the fixed baseline length, which causes the emission to be spatially filtered out at higher resolution, consequently resulting in underestimated flux densities. 73 % of these negative spectral indices ($\alpha \leq -0.5$) are associated with resolved sources as can be seen in figure 2.8b, which supports this possibility.



(a)



(b)

Figure 2.8 (a) Spectral index distribution of the CORNISH UCHII regions. (b) Distribution of the spectral indices as a function of the angular sizes at 22GHz

In short, spectral index values are more reliable for the sources that are unresolved in both frequencies.

The list of steep negative spectral indices (in a range of -2.6 to -3.73) comprise the sources G337.6320-0.0781, G336.0270-0.8170 and, G300.4010+0.5461, all of them being extended. For these cases filtering of the extended emission due to the different sensitivity can still be the primary cause for the negative values of the spectral indices, since they all appear to be poorly imaged at 22 GHz compared to the 17 GHz image. At 17 GHz G337.6320-0.0781 and G300.4010 +0.5461 are large cometary sources while at 22 GHz the entire tail has not been detected. However there is a short list of unresolved sources with negative spectral indices, these sources

being G307.7360-0.5944, G333.3400-0.1279, G337.8440-0.3734, G339.4670+0.0837, G345.1980-0.0301, G345.9880+0.4696. In this it is unlikely that the sources were affected by filtering of flux at higher resolution, since they are smaller than the beam size in both frequencies. This possible non-thermal emission can be evidence of dynamic phenomenon such as for example jets (Purser, Lumsden, Hoare, and Kurtz 2021), or bow shocks from runaway massive stars (Pereira et al. 2016). To understand more, further investigation should be done.

The CORNSH-South UCHII region fluxes available in 5GHz, 9GHz, 17GHz and 22GHz were combined and the spectral energy distributions (SEDs) were presented in figure 2.9. These data comprise 57 sources. The SEDs were constructed with the objective of inferring whether they are consistent with the radiation from free-free emission mechanisms expected for UCHII regions. The SEDs can also show the turnover frequency of the source. which is the case for some of them. For example G337.7050-0.0532, G337.7130+0.0879, G337.8440-0.3747 and G344.9100+0.2469. As presented in figure 2.8 the sample is dominated by optically thin sources four young UCHII regions, the turnover for young UCHII regions is expected to be between 5GHz to 15GHz (Kalcheva 2018), in this context, the higher the turnover the younger the UCHII region. The vast majority of the radio SEDs appear to show an issue with the current value of the 9 GHz survey fluxes. This will be returned to in the next chapter and thus should be ignored here. If the 9 GHz fluxes are ignored in the SEDs, most of them look consistent with the expected shape, and they even show a turnover between 5 and 17 GHz. More complete radio SEDs could be studied in the future to look for the phenomenon causing the non-thermal appearing spectral indices and to accurately identify the turnover frequency.

Table 2.5 | Fluxes of 17 GHz and 22 GHz CORNISH-South UCHII regions, and calculated 22GHz-17GHz spectral indices.

Source name	F_{17GHz} (mJy)	F_{22GHz} (mJy)	$\alpha_{22GHz-17GHz}$
G295.1520-0.5882	23.81 ± 0.82	20.92 ± 0.72	-0.440 ± 0.166
G297.4570-0.7628	5.35 ± 0.11	5.39 ± 0.41	0.025 ± 0.268
G297.6590-0.9720	27.03 ± 0.36	23.60 ± 0.53	-0.462 ± 0.089
G300.4010+0.5461	15.57 ± 0.37	7.10 ± 1.00	-2.674 ± 0.486
G302.0220+0.2539	94.91 ± 1.28	81.63 ± 1.76	-0.513 ± 0.087
G303.9390-0.6895	36.93 ± 0.69	36.04 ± 0.48	-0.083 ± 0.078
G305.7980-0.2415	7.95 ± 0.21	< 3.21	-0.67
G307.7360-0.5944	4.81 ± 0.03	3.01 ± 0.24	-1.596 ± 0.272
G308.0560-0.3961	192.10 ± 2.90	177.10 ± 2.50	-0.277 ± 0.070
G311.1360-0.2373	3.76 ± 0.07	3.30 ± 0.29	-0.44 ± 0.306
G311.5960-0.3984	11.48 ± 0.14	11.67 ± 0.35	0.055 ± 0.110
G311.6430-0.3800	255.90 ± 5.3	226.80 ± 2.20	-0.411 ± 0.078
G312.3070+0.6608	18.55 ± 0.39	18.12 ± 0.29	-0.080 ± 0.090
G312.5480-0.2809	10.01 ± 0.19	8.78 ± 0.61	-0.447 ± 0.246
G314.2200+0.2727	22.83 ± 0.36	19.50 ± 0.09	-0.537 ± 0.056
G317.4290-0.5609	20.23 ± 0.24	22.75 ± 0.13	0.400 ± 0.045
G317.8890-0.0584	8.73 ± 0.45	8.00 ± 0.572	-0.297 ± 0.299
G318.0470+0.0855	1.89 ± 0.04	1.40 ± 0.02	-1.022 ± 0.090
G323.4590-0.0787	443.00 ± 11.0	494.00 ± 16.0	0.371 ± 0.139
G326.4480-0.7484	5.00 ± 0.27	4.74 ± 0.34	-0.182 ± 0.306
G327.6370-0.1462	2.70 ± 0.11	2.470 ± 0.16	-0.303 ± 0.261
G327.9010+0.1539	2.48 ± 0.14	2.24 ± 0.20	-0.347 ± 0.360
G329.2720+0.1148	6.75 ± 0.23	6.78 ± 0.37	0.015 ± 0.219
G329.5240+0.0846	5.56 ± 0.35	5.17 ± 0.38	-0.248 ± 0.330
G329.8150+0.1407	6.71 ± 0.34	5.78 ± 1.13	-0.508 ± 0.688
G330.2950-0.3929	813.05 ± 5.12	644.30 ± 2.89	-0.792 ± 0.026
G330.9280-0.4070	7.61 ± 0.29	6.96 ± 0.75	-0.304 ± 0.389
G331.5120-0.1027	356.70 ± 3.51	349.00 ± 18	-0.074 ± 0.179
G333.0290-0.0631	26.05 ± 0.80	25.70 ± 1.1	-0.046 ± 0.179
G333.3400-0.1279	3.06 ± 0.11	2.50 ± 0.19	-0.689 ± 0.287
G333.3870+0.0318	6.43 ± 0.21	5.68 ± 0.47	-0.422 ± 0.303
G335.3900-0.2905	47.20 ± 4.2	60.00 ± 2.8	0.817 ± 0.342
G336.0270-0.8170	15.33 ± 0.73	6.76 ± 1.10	-2.788 ± 0.579
G336.8640+0.0048	23.00 ± 1.0	30.30 ± 1.0	0.939 ± 0.186
G336.9830-0.1832	53.80 ± 4.7	55.50 ± 4.8	0.106 ± 0.419
G337.4040-0.4024	141.80 ± 2.40	136.46 ± 2.31	-0.131 ± 0.082
G337.6320-0.0781	30.52 ± 1.24	13.83 ± 2.43	-2.696 ± 0.614
G337.7050-0.0532	156.60 ± 5.8	117.70 ± 8.10	-0.972 ± 0.266
G337.7130+0.0879	12.23 ± 0.51	12.38 ± 1.05	0.041 ± 0.322
G337.8440-0.3734	26.75 ± 0.91	16.03 ± 0.53	-1.744 ± 0.162
G338.2710-0.2924	8.92 ± 0.61	8.93 ± 2.28	0.005 ± 0.900
G338.3250+0.1547	< 8.12	< 7.65	-0.04
G338.3620+0.1409	9.52 ± 0.19	6.35 ± 1.92	-1.379 ± 1.032
G338.5660+0.1096	5.57 ± 0.53	< 3.26	-0.38
G339.4670+0.0837	6.43 ± 0.29	3.81 ± 0.42	-1.782 ± 0.406
G339.9800-0.5386	62.70 ± 3.4	46.07 ± 1.37	-1.050 ± 0.211

Table 2.6 | Continued from previous table.

Source name	F_{17GHz} (mJy)	F_{22GHz} (mJy)	$\alpha_{22GHz-17GHz}$
G340.2490-0.3717	50.75 ± 1.90	35.00 ± 4.97	-1.265 ± 0.500
G340.7850-0.0959	17.25 ± 0.57	16.09 ± 0.92	-0.237 ± 0.225
G341.9740+0.2251	63.30 ± 3.6	58.83 ± 0.75	-0.250 ± 0.198
G342.7090+0.1253	8.00 ± 0.34	7.80 ± 1.32	-0.087 ± 0.592
G343.9290+0.1249	57.64 ± 0.99	53.97 ± 0.56	-0.224 ± 0.068
G344.5820-0.0238	18.68 ± 0.14	30.02 ± 0.07	1.6 ± 0.03
G344.9100+0.2469	15.11 ± 0.36	8.44 ± 0.38	-1.983 ± 0.173
G345.1980-0.0301	5.18 ± 0.10	3.45 ± 0.13	-1.384 ± 0.144
G345.4070-0.9516	860.68 ± 18.77	748.22 ± 4.66	-0.476 ± 0.077
G345.5470-0.0803	91.59 ± 1.21	79.79 ± 4.21	-0.470 ± 0.185
G345.9880+0.4696	3.74 ± 0.28	2.96 ± 0.64	-0.797 ± 0.778
G346.1960+0.0402	4.48 ± 0.33	3.92 ± 0.45	-0.455 ± 0.464
G346.2330-0.3197	22.531 ± 0.265	21.39 ± 1.09	-0.177 ± 0.178
G347.3050+0.0148	8.17 ± 0.33	7.96 ± 0.60	-0.089 ± 0.291
G347.6280+0.1482	167.50 ± 8.80	154.20 ± 1.63	-0.282 ± 0.182
G347.8980+0.0436	5.31 ± 0.37	4.57 ± 1.14	-0.511 ± 0.881
G348.3510+0.1515	4.50 ± 0.17	3.93 ± 2.44	-0.465 ± 1.149
G348.5500-0.3386	22.47 ± 0.41	18.69 ± 1.19	-0.627 ± 0.226
G348.6130-0.9099	4.49 ± 0.33	1.50 ± 0.91	-3.734 ± 2.087
G348.6490+0.0228	4.02 ± 0.25	3.88 ± 1.34	-0.121 ± 1.195
G348.7280-1.0417	171.02 ± 20.56	111.90 ± 5.04	-1.444 ± 0.437
G348.8920-0.1796	186.82 ± 8.37	132.95 ± 1.29	-1.158 ± 0.156
G349.7210+0.1213	41.52 ± 0.899	40.93 ± 0.98	-0.049 ± 0.110
G350.0150+0.4329	107.80 ± 6.9	116.35 ± 1.60	0.260 ± 0.223
G350.1110+0.0882	< 43.01	< 32.03	-0.22
G350.1210+0.0592	303.20 ± 10.74	220.20 ± 3.56	-1.089 ± 0.133

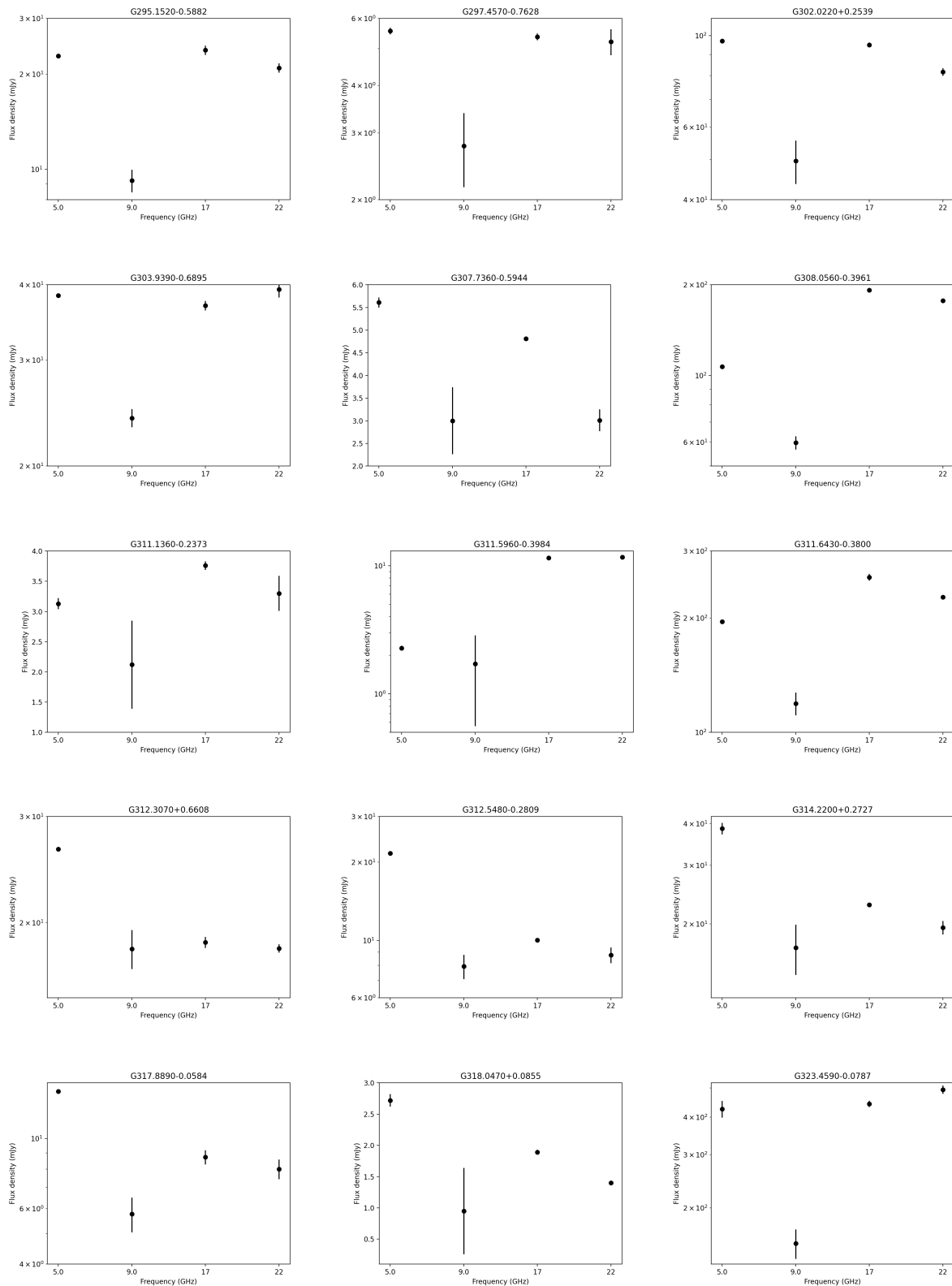


Figure 2.9 Radio spectral energy distributions of UCHII regions with available 5 GHz, 9 GHz and 17 GHz and 22 GHz flux densities

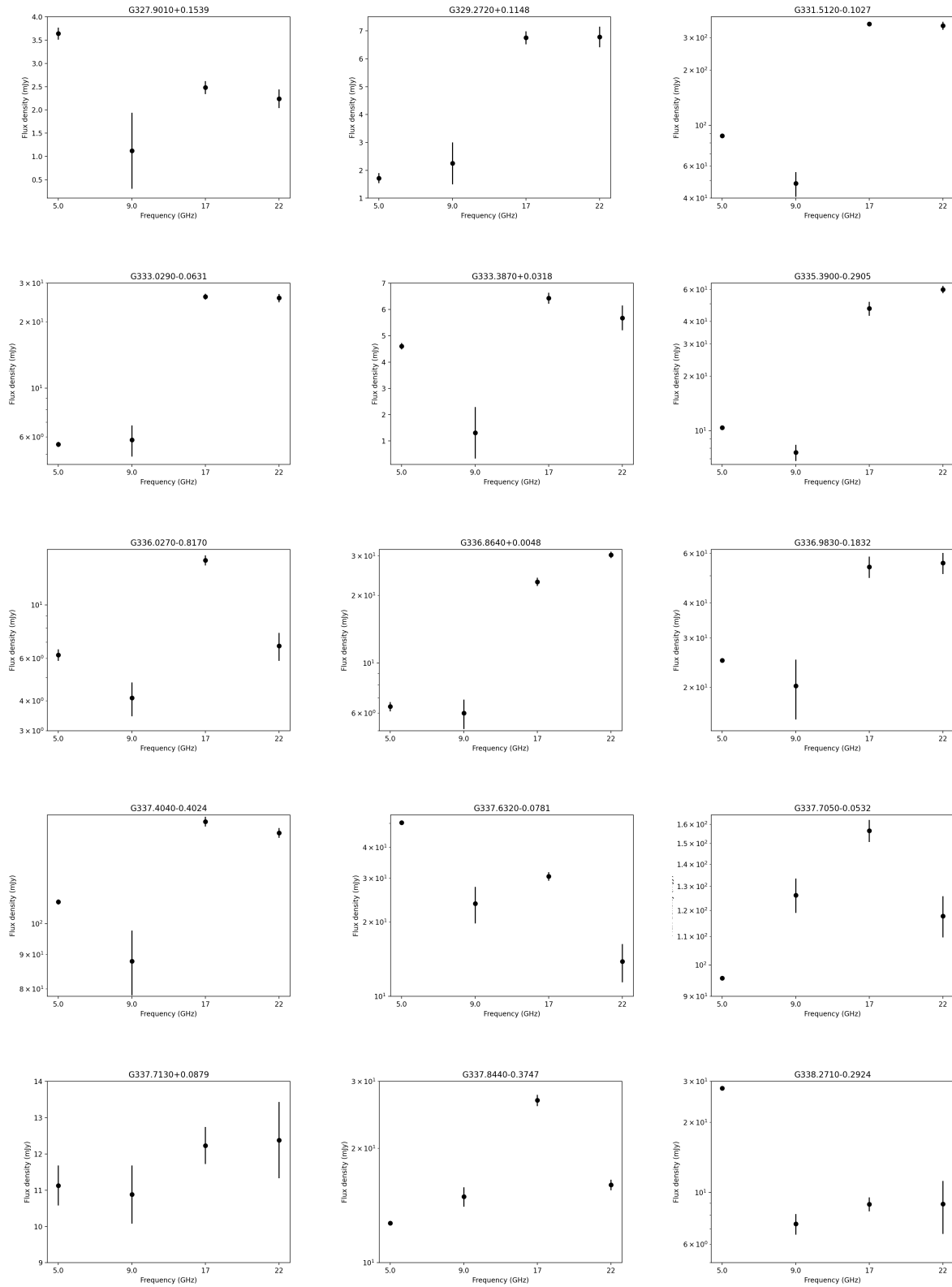


Figure 2.10 Radio spectral energy distributions, continued

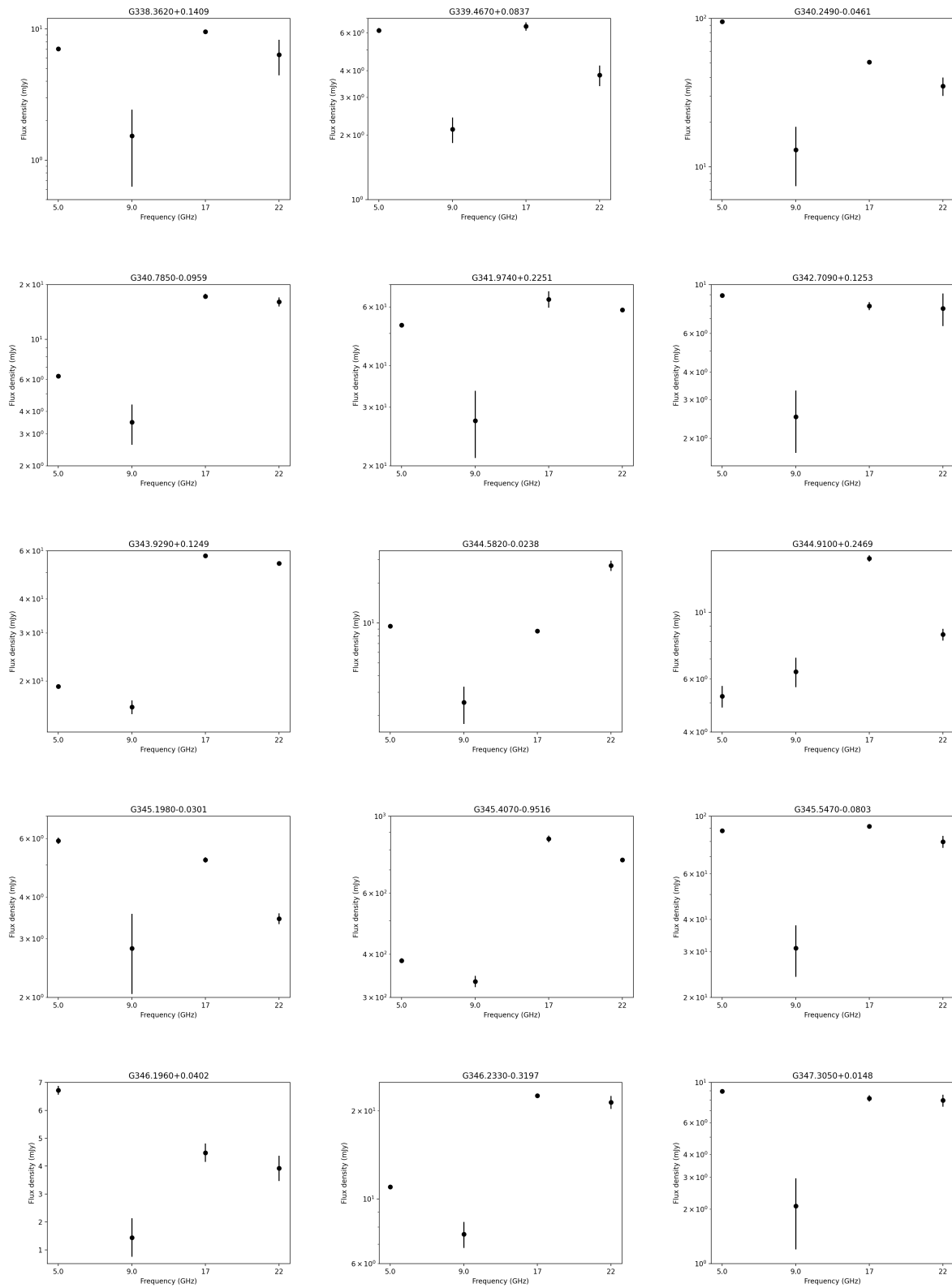


Figure 2.11 Radio spectral energy distributions, continued

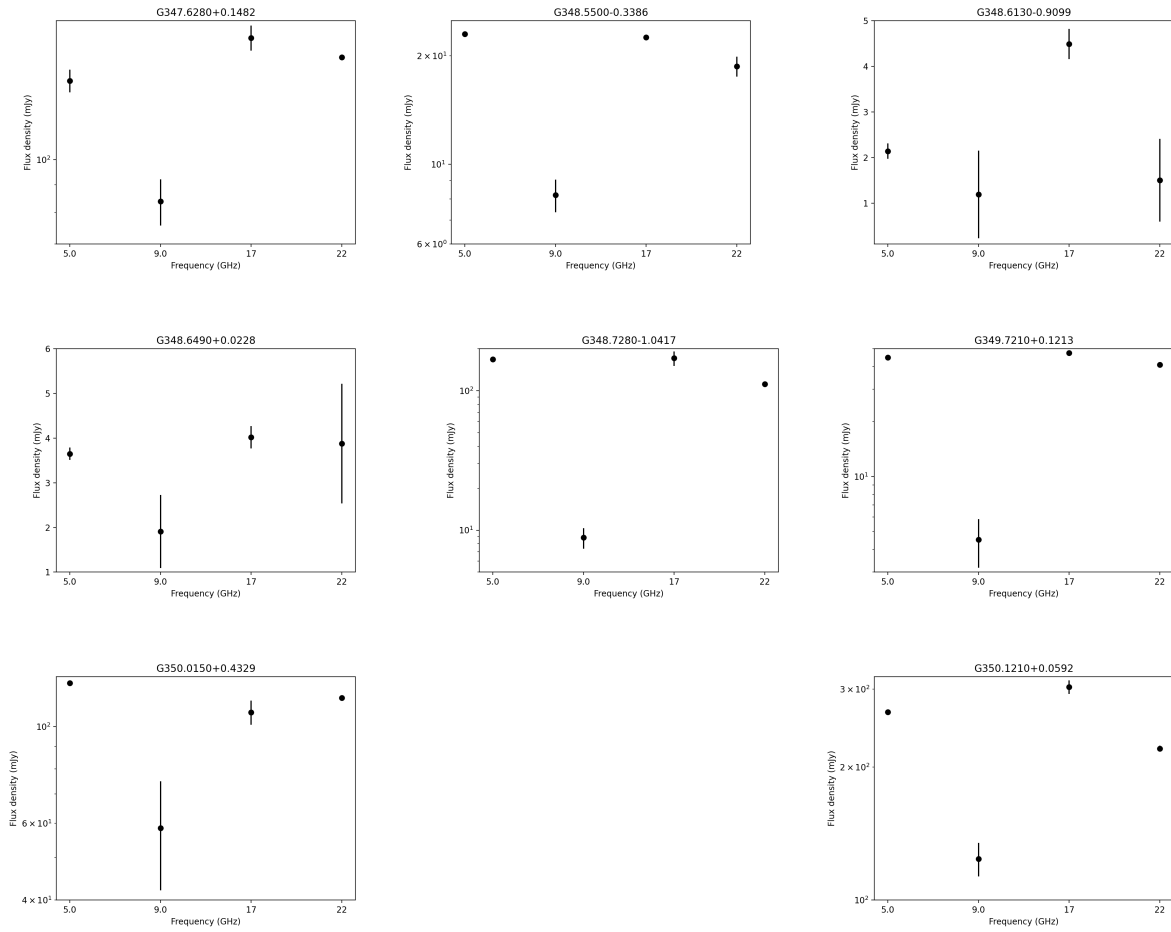


Figure 2.12 Radio spectral energy distributions, continued

2.8 Conclusions

Observations with higher resolution at 17GHz and 22 GHz were presented for 72 CORNISH-South UCHII regions considered unresolved at 5GHz, i.e, with angular sizes smaller than $2.8''$. The targets were reduced and imaged using a semi-automated pipeline, and all but four sources were detected. Four sources were found to be comprised of at least more than one component at the higher resolution follow-up. The majority of the detected UCHII regions remain unresolved at 17 GHz, approximately 56%. While at 22 GHz the opposite is true, approximately 43% are unresolved. Several sources are sufficiently resolved to provide morphological information. In this subset, $\sim 38\%$ of the resolved sources show cometary morphology.

Physical properties and spectral indices of the detected sources were presented and the sample is composed mostly of optically thin sources. 31% of the available spectral indices are found to be below the lower limit for free-free emission. To find the cause of this emission these sources could be further investigated in future.

A well sampled SEDs were constructed with available data in 5GHz, 9GHz, 17GHz and 22GHz, to infer if they are consistent with the radiation from UCHII region. The majority of the SEDs show that the 9GHz fluxes are systematically lower than the expected. However, ignoring the 9 GHz fluxes, the SEDs do agree with the expected shape and most of them show a turn over between 5 and 17 GHz.

Chapter 3

5.5 and 9 GHz Properties of the CORNISH-South UCHII regions

3.1 Introduction

The aim of this chapter is to validate the nature of the 255 candidate UCHII regions, detected by the CORNISH-South survey at 5.5 GHz and presented in the catalogue. Simultaneously with the 5.5 GHz observations the CORNISH-South survey also made observations at 9 GHz with higher resolution. The 9 GHz survey data have been pipeline reduced as well as source finding and initial flux measurements carried out by Irabor (private communication). The nature of the visually identified as UCHII regions source were investigated through their observational and derived physical properties. Spectral indices which were estimated for the sources that are detected in both 5.5 GHz and the 9 GHz observations. Through this investigation a final catalogue of the southern UCHII regions should be provided.

3.2 Radio Properties of the 5.5 GHz UCHII regions

The integrated fluxes, angular sizes and Galactic latitude distribution were measured as the primary properties of the radio sources from a continuum observation. The procedures used to measure the primary properties of the CORNISH-South sources are explained in Irabor, Hoare, Burton, et al. (2023), and summarized here.

Source finding and characterization was performed using the AEGEAN software, a program

implemented by Hancock et al. (2012) to detect and characterize sources within radio images. AEGEAN characterizes the background and noise properties of the image, then works by defining two thresholds, σ_s (seeding threshold) and σ_f (flooding threshold), which are used to seed an island and to grow the island respectively. The seeding threshold and the flooding threshold are defined such that $\sigma_s \geq \sigma_f$. The islands are groups of pixels in the image that are significant deviations above the background within the radio image. The AEGEAN program assumes that the detected sources are compact and characterizes them by fitting with one or more overlapping 2D Gaussians.

For the compact sources fitted with a single Gaussian, the integrated flux densities and its associated errors were measured by the AEGEAN using the equations (3.1) and (3.2), but the rms noise level was re-measured using the aperture photometry.

$$S = \frac{A\pi}{4\ln(2)} \frac{\theta_{maj}\theta_{min}}{\theta_{bm}^2} \quad (3.1)$$

$$\frac{\sigma_S^2}{S^2} \approx \frac{\sigma_A^2}{A^2} + \frac{\theta_{bm}^2}{\theta_{maj}\theta_{min}} \left[\frac{\sigma^2(\theta_{maj})}{\theta_{maj}^2} + \frac{\sigma^2(\theta_{min})}{\theta_{min}^2} \right] \quad (3.2)$$

where A is the peak amplitude, θ_{maj} is the major axis, θ_{min} is the minor axis and θ_{bm} is the synthesized beam size, $\sigma(\theta_{min})$ and $\sigma(\theta_{maj})$ are the errors on the Gaussian fits.

Extended non-Gaussian sources were detected by searching for sources fitted with multiple Gaussians by the AEGEAN source finder. For these sources the flux densities were measured by defining a single 2D polygon to trace the outer outline of the emission. There were some exceptions, where the extended sources were not properly imaged and appear to be multiple individual Gaussians. In such cases, the outline of the real emission was again traced manually. Having the polygon defined, new diameters and intensity weighted centres were determined. Aperture photometry for the extended sources was used to measure flux density and the weighted diameter within the defined polygon, the equation used for the flux densities and its uncertainties are:

$$S = \left(\sum_{i=1}^{N_{src}} A_i - N_{src}\bar{B} \right) / a_{bm} \quad (3.3)$$

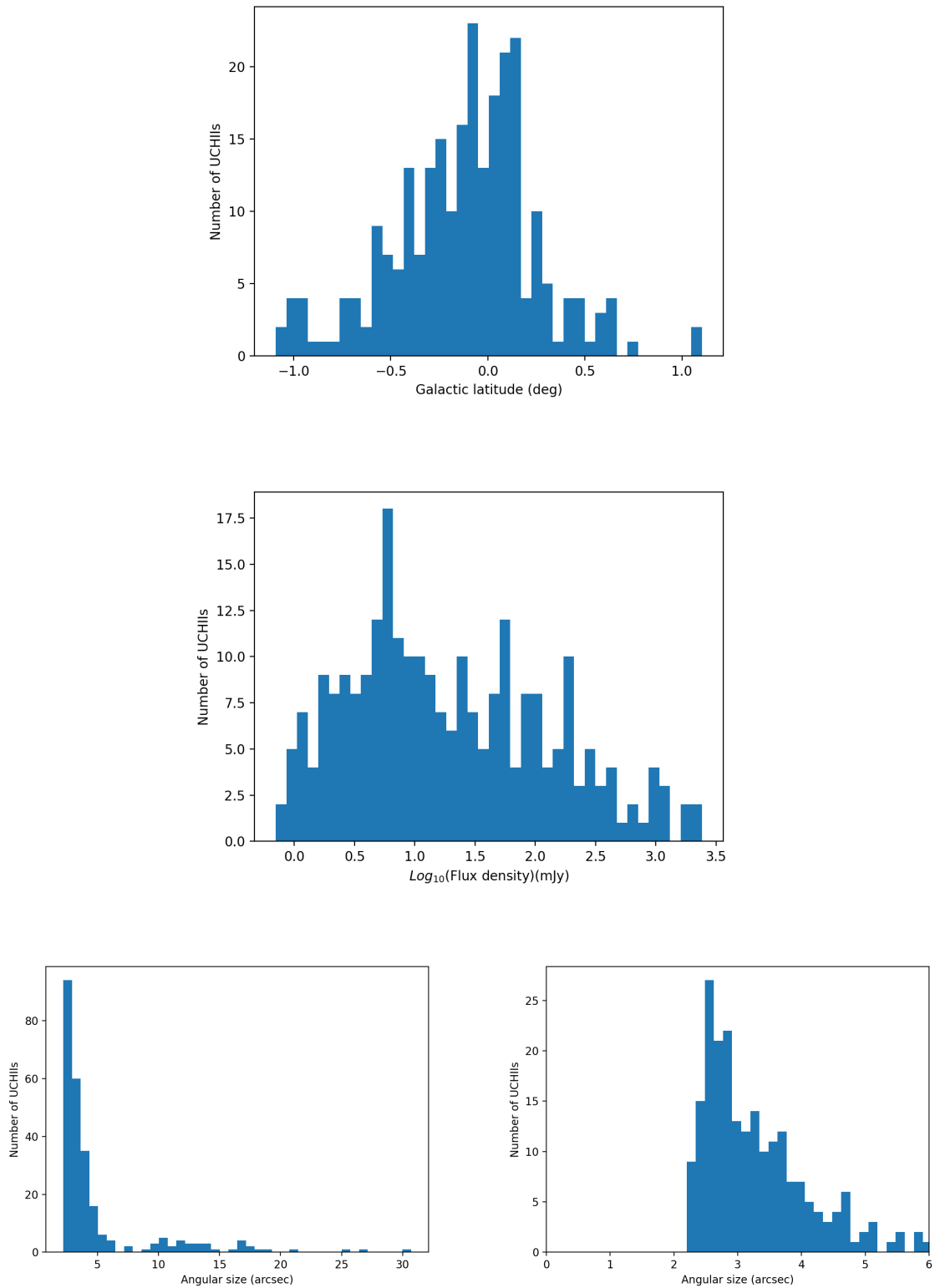


Figure 3.1 | Observational radio properties of the UCHII regions sample. Distributions of the Galactic latitude (top panel), distribution of the flux density and integrated flux (middle panel), and distribution of the angular sizes density (bottom panel).

$$\sigma_S^2 = \left(\sigma \left(\sum A_i \right)^2 + \frac{\pi N_{src}^2 \sigma_g^2}{2 N_{sky}} \right) / a_{bm} \quad (3.4)$$

where $\sum_{i=1}^{N_{src}} A_i$ is the total flux in given aperture over N_{src} pixels, \bar{B} is the median background flux and a_{bm} is the beam area. σ_g^2 is the variance and N_{sky} is the number of pixels in the annulus (A contour at the sky area outside the drawn polygon). The annulus provides a good estimate of the background level around a source.

To determine the angular sizes of the Gaussian sources the geometric mean of the major- and minor-axis was calculated using equation (2.1), and the associated uncertainties using equation (2.2). The angular size for the extended non-Gaussian sources is the intensity-weighted diameter, and is given by the equation (3.5).

$$d_w = \frac{\sum_{i=1}^{N_{src}} r_i A_i}{\sum_{i=1}^{N_{src}} A_i} \quad (3.5)$$

where d_w is the intensity weighted diameter and $\sum_{i=1}^{N_{src}} A_i$ is the sum of the flux within the defined source aperture.

215 of the CORNISH South UCHII regions were found to be Gaussian sources and the remaining 40 CORNISH South UCHII regions to be extended sources.

Figure 3.1 (top panel) shows the distributions of the CORNISH-South UCHII regions in Galactic latitude. The Galactic latitude distribution shows that the sources are concentrated towards the Galactic mid-plane as expected for very young massive star forming regions (Urquhart, Thompson, et al. 2013). This distribution is similar compared to the CORNISH-North catalogue (Kalcheva 2018).

Figure 3.1 (middle panel) shows the distribution of the integrated flux of the sample. The distribution falls above the 100% completeness limit for the CORNISH-South catalogue, which is $> 3\text{mJy}$ as discussed by Irabor, Hoare, Burton, et al. (2023). The histogram shows that the distribution of the flux density peaks at $\sim 5.74\text{ mJy}$, and the brightest source has a flux density of 2.413 Jy , thus showing fainter sources compared to the CORNISH-North survey.

The CORNISH-South UCHII regions with angular sizes less than $2.8''$ are marked as unresolved, based on the CORNISH-South restoring beam size of $2.5''$ and on the mean error of the angular size of $0.3''$ (Irabor, Hoare, Burton, et al. 2023). The sample of candidate UCHII regions is

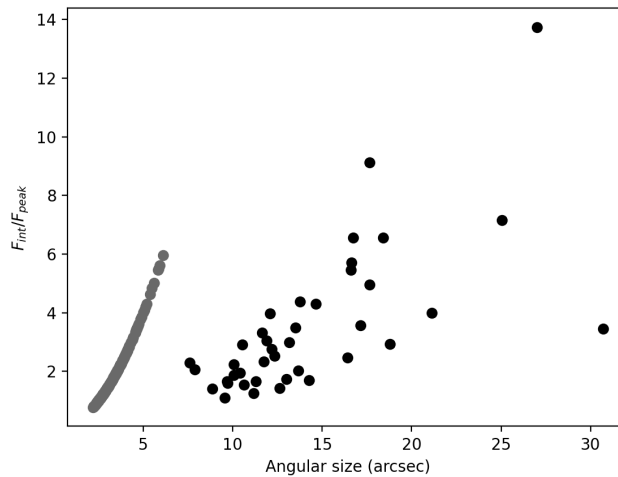


Figure 3.2 | Ratio of the integrated to peak flux against angular size of the 255 CORNISH-South UCHII regions. Gaussian sources are shown as grey circles and polygonal sources are shown as black circles.

dominated by resolved sources (183), with the remaining 72 sources being unresolved sources. The angular size distribution peaks at $\sim 2.9''$ extending up to $\sim 31''$ as shown in Figure 3.1 (bottom left panel). The angular size distribution presented in figure 3.1 (bottom left panel) was zoomed in to show details in the range of $0''$ to $6''$, which is where most of the sources are confined in, and the histogram is presented in figure 3.1 (bottom right panel). 15.6 % of the sample are polygonal sources and, as expected all of them have angular sizes greater than $2.8''$ while the Gaussian sources have their angular sizes in the range of $2.20''$ to $6.11''$. This is clearly shown in figure 3.2, where the ratio of the integrated to peak flux is shown as a function of angular size of each source. The Gaussian sources show an increase of the flux ratio with increasing angular size, while the polygonal sources do not show this trend. The trend of the flux ratio with increasing angular size shows that the flux ratio is ~ 1 , which is expected for Gaussian sources.

3.2.1 Derived physical properties

Figure 3.3 shows the brightness temperature distribution of the CORNISH UCHII regions and its corresponding optical depth. As presented in previous chapters the radio continuum emission of the UCHII regions can be expressed in terms of the brightness temperature, and this property is very useful to investigate the evolutionary stage of the UCHII regions.

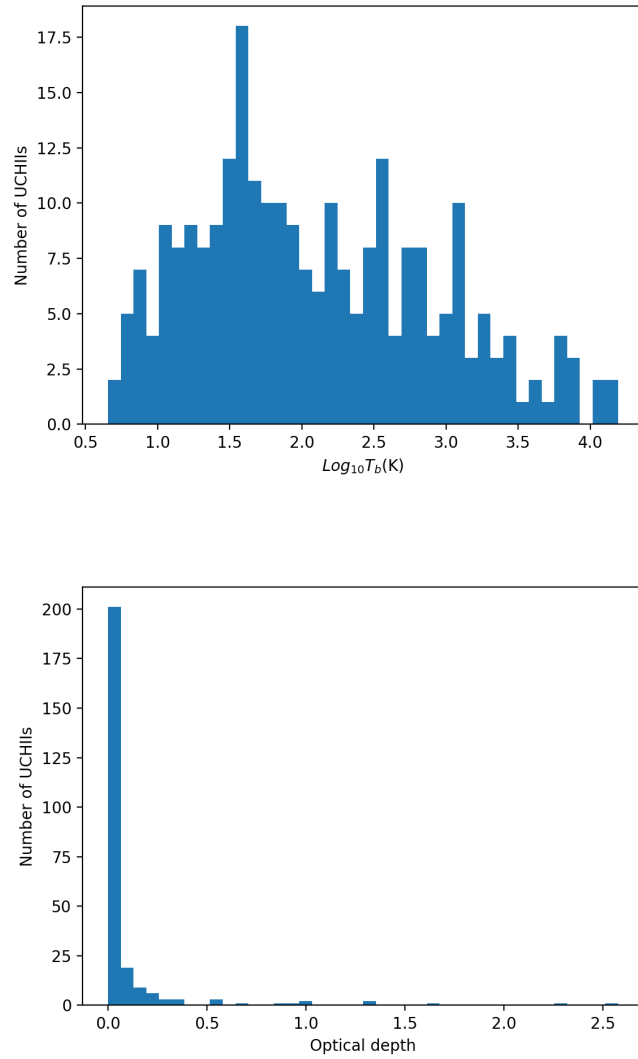


Figure 3.3 | Derived physical properties of the 5GHz CORNISH-South UCHII regions. Left: Distribution of the brightness temperature of the CORNISH-South UCHII regions at 5 GHz. Right: Distribution of the optical depth of the CORNISH-South UCHII regions at 5 GHz

The brightness temperatures were estimated using equation 2.3 and the optical depths τ_ν were estimated using equation 2.4, presented in the previous chapter.

The distribution presented in 3.3 shows the brightness temperature distribution varying in a range of ~ 5 K to ~ 15602 K with a median of ~ 91 K and peaking at ~ 40 K, above which the number of sources drops off. Although distances and physical sizes would also be necessary to infer the evolutionary stage of the UCHII regions, the variation of the angular sizes with corresponding flux densities colour coded by the brightness temperature presented in figure 3.4 can provide clues of the age of our sample. The graph shows that there are more UCHII

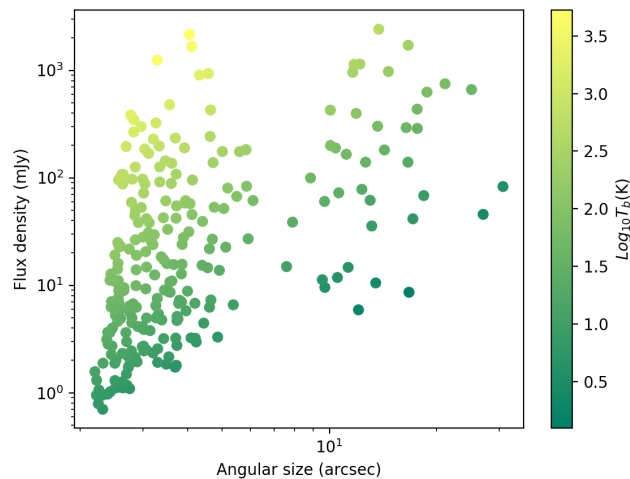


Figure 3.4 Flux density against angular sizes, showing colour coded by the brightness temperature.

regions that are young and compact. Some of these sources have low flux density and low brightness temperature but more of them have higher flux density and brightness temperature. The distribution of the CORNISH-South UCHII regions optical depth shown in figure 3.3 peaks towards zero ($\tau \ll 1$ for the majority of the sources). This distribution corresponds to optically thin sources.

3.3 Aperture Photometry

The 5.5 GHz UCHII regions from the CORNISH-South survey were cross-matched with the 9 GHz sources within a radius of 3". This resulted in a total of 145 matches out of the initial 255 5.5 GHz CORNISH-South UCHII regions. 74% of the cross-matched sources have angular separations less than 1" and this distribution is presented in figure 3.5. There were sources matching more than once, therefore to obtain a reliable cross-match with the 5.5 GHz table, visual identification of the matching sources was done.

The flux densities and magnitudes of 64 extended 9 GHz CORNISH-South sources, not measured with the AEGEAN algorithm, were measured via aperture photometry, with an algorithm implemented in python created by Purcell et al. (2013) for the CORNISH-North and adapted by Irabor, Hoare, Oudmaijer, et al. (2018) for the southern part. To check the reliability of the flux densities measured with the aperture photometry script the photometry script was performed on the compact 9 GHz sources, which have the flux densities already measured with

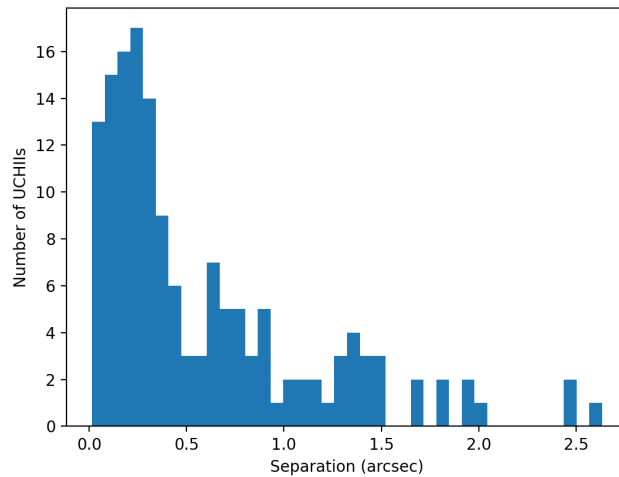


Figure 3.5 Distribution of the angular separation of the 154 CORNISH UCHII regions found in 9 GHz within a cross-matching radius of 3".

the AEGEAN algorithm. The flux densities measured with the AEGEAN algorithm are plotted against the flux densities measured with photometry and shown in figure 3.6. The plot shows that the aperture photometry is working correctly, since it is nearly showing a one-to-one plot between fluxes with the AEGEAN measurements and fluxes with photometry measurements.

3.3.1 Correction of the 9 GHz CORNISH-South UCHII regions

In the previous chapter, SEDs of the CORNISH-South UCHII regions available at 5.5 GHz, 9 GHz, 17 GHz and 22 GHz were presented, but further analysis were left to be discussed here. Most of the SEDs show that the 9 GHz fluxes are below where they should be if a line is fitted between 5.5 GHz and 17 GHz. Thus predicted 9 GHz fluxes were interpolated between 5.5 GHz and 17 GHz to quantify and correct the apparent error. In figure 3.7 a plot of the observed 9 GHz fluxes as a function of the interpolated 9 GHz fluxes is presented. The graph shows that the observed 9 GHz fluxes are systematically low by a factor of 2. The 9 GHz sample of UCHII regions was also cross-matched with the 8.6 GHz sample of UCHII regions from the RMS survey paper by Urquhart, Busfield, et al. (2007). A graph of the RMS 8.6 GHz flux densities as a function of the 9 GHz CORNISH-South flux densities with the one-to-one line ($y=x$) and the best fit line defined by $\log(y) = 0.90\log(x) + 0.46$ was plotted and is presented in figure 3.8. The plot shows that the 8.6 GHz RMS fluxes are systematically higher than the 9 GHz CORNISH-South fluxes.

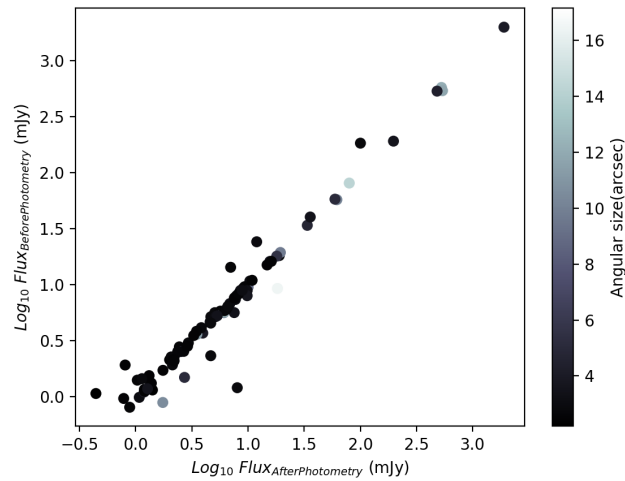


Figure 3.6 | Sanity check of the aperture photometry script. Right: The 9 GHz flux densities measured with the AEGEAN algorithm are plotted against the 9 GHz flux densities measured with the automated photometry.

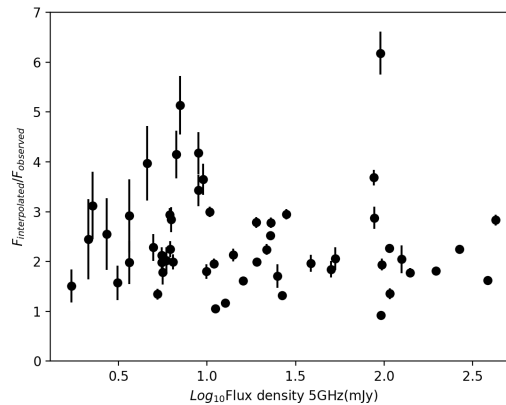


Figure 3.7 | Comparison between the observed 9 GHz flux to the predicted flux interpolated between 5 and 17 GHz.

Using the equation that define the best fit line presented in figure 3.8, a typical correction factor for the 9 GHz was determined based on the RMS 8.6 GHz fluxes. This was done by computing the difference between the best fit line and the $y=x$ line at a suitable flux level. This gives a factor of ~ 2.5 , which is very close to the factor of 2 determined by the predicted interpolated 9 GHz fluxes. The factor of 2 determined by the predicted interpolated 9 GHz fluxes was used to correct the observed 9 GHz fluxes for the whole sample. Using this correction factor, the spectral index histogram is shifted to the right by one unit. However, fig3.7 shows that not all sources have the flux density deviated by a factor of 2, some are deviated by a higher factor such as 6 for example, so applying a constant correction factor does not correct the flux density

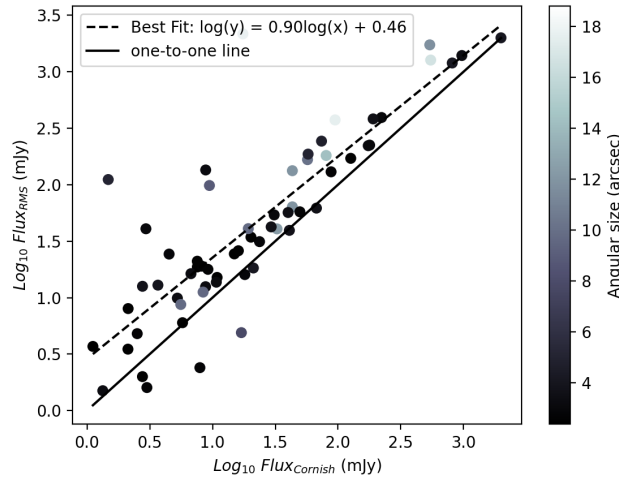


Figure 3.8 | Plot of the RMS 3.6 cm (Urquhart, Busfield, et al. 2007) flux densities against the 9 GHz CORNISH-South flux densities. The continuous line is the one-to-one line ($y=x$) and the dotted line is the best fit line defined by $\log(y) = 0.90\log(x) + 0.46$

for all sources accurately. To correct the flux density of that is higher by a factor of 6 for example, the observed 9 GHz flux would have been multiplied by 6, which would shift the point in the histogram by 3 units to the right.

3.3.2 9GHz-5GHz spectral indices

Spectral indices were estimated for the cross-matched 5.5 and 9 GHz CORNISH-South UCHII regions. The spectral indices were calculated using equation 2.5 and the associated errors using equation 2.6. The results are presented in figure 3.9a and table B.1.

As explained in the previous chapter its expected that the spectral index range is between -0.1 and 2, which is between the optically thin and optically thick limit. 54% of the CORNISH-South UCHII regions do agree with the thermal emission expected from UCHII regions. The distribution of the spectral indices presented in figure 3.9a shows a peak at ~ -0.8 which is slightly below the optically thin limit taking errors into account. 46% of the 145 sources have spectral indices out of the expected range considering the errors. A plot of spectral indices as a function of angular sizes is presented in figure 3.10. This was done to infer whether the extended sources are the ones falling out of the expected values. If so, spatially filtered out fluxes at 9GHz could have been the reason of the negative values. The graph presented does not show a tendency to have only extended sources below the optically thin limit, as it can be seen, many compact sources are also below the optically thin limit. This is justified by the

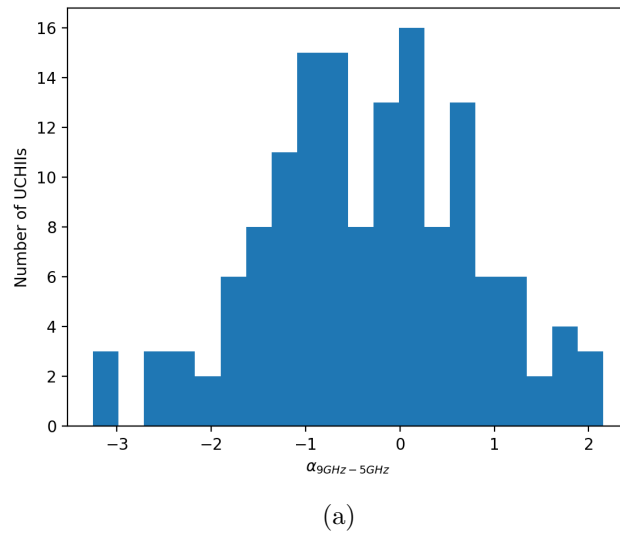


Figure 3.9 | 9GHz - 5GHz spectral index distribution of the CORNISH-South UCHII regions.

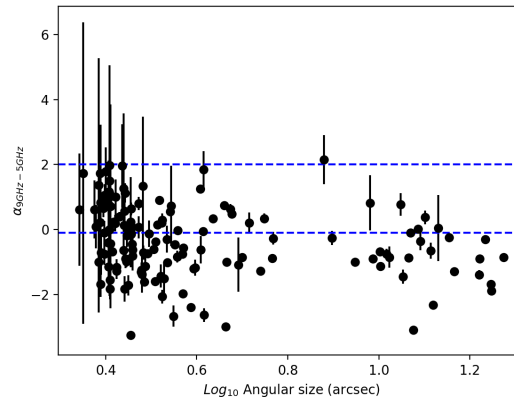


Figure 3.10 | 9GHz-5GHz spectral index distribution as a function of angular sizes at 5.5 GHz.

fact that the correction factor of 2 applied to the observed 9 GHz fluxes is not constant for all sources. In figure 3.7 it is seen that some sources have the correction factor much greater than 2. As the sample used to determine the correction factor is quite reduced compared to the sample of sources for which the spectral index was calculated, so there is no way to identify among the sources below the optically thin limit which one is the real correction factor to see how far are they from 2.

3.4 Conclusions

In this chapter, the 5.5 GHz physical properties of the CORNISH-South UCHII regions were analysed and the 9GHz-5GHz spectral indices were estimated with the purpose of nature confirmation of the UCHII regions from the full catalogue of the CORNISH-South survey. 100% of the sources are confined at the Galactic mid-plane, as UCHII regions are supposed to be. The flux density distribution falls above the completeness limit of the CORNISH-South survey. 72% of the sources are classified as resolved. The unresolved sources have angular size $< 2.8''$, based on the beam size and the mean error of the deconvolved angular size.

The SEDs presented in chapter 2 show that the observed 9 GHz flux densities are systematically lower than what they were supposed to be. 9 GHz fluxes were interpolated between 5.5 GHz and 17 GHz and a factor of 2 was determined for correction of the observed 9 GHz fluxes. With the corrected fluxes, the 9GHz-5GHz spectral indices were estimated. 54% of the sample have spectral indices between the optically thin and the optically thick limit, taking errors into account, with many sources near the optically thin limit. Further investigations into the causes of the error on observed 9 GHz fluxes is needed to be able to understand the reason why 46% of the sources are found below the optically thin limit.

Chapter 4

Conclusion and Future Work

4.1 Conclusions

Due to dust extinction near the Galactic plane, observation of the UCHII regions is limited in the optical domain. Thus, the search for UCHII region population requires observations at longer wavelengths where dust extinction can be overcome. Through a large scale, high quality and high resolution radio continuum survey provided by the CORNISH-South survey, the focus of this thesis was to study the properties of the UCHII regions of the Milky Way southern Galactic plane. The CORNISH-South survey is a radio continuum survey that mapped the area of the Galactic plane defined by $10^\circ < l < 65^\circ$ and $|b| < 1^\circ$ at 5.5 and 9 GHz. The data processing was performed by Irabor, Hoare, Burton, et al. (2023) and at a 7σ limit 5013 sources were detected.

Higher resolution observations at 17 GHz and 22 GHz were carried out for 72 CORNISH-South UCHII regions that were not sufficiently resolved at 5.5 GHz and 9 GHz observations. Calibration and imaging of these observations was performed with MIRIAD and presented in this work. The properties of the Gaussian sources were measured by fitting a 2D Gaussian with the imfit task in CASA. While the properties of the non-Gaussian extended sources were measured by drawing manually a polygon around the source. 38% of the sample was described by such polygons at 17 GHz and 40% at 22 GHz.

22GHz-17GHz spectral indices were estimated. In majority of cases, the estimated spectral indices are consistent with optically thin emission, but 32% of cases were not consistent with free-free emission. These cases where the spectral index is apparently from non-thermal emission

could be due to the fixed baseline length, which causes the emission to be spatially filtered out at higher resolution for extended sources, or associated physical mechanism resulting in a non-thermal contribution to the flux. 6 unresolved sources were found below the optically thin limit, these candidate non-thermal emission should be investigated to identify their origin. Several sources are sufficiently resolved to provide morphological information. In this subset, $\sim 38\%$ of the resolved sources show cometary morphology.

The results from the 17 and 22 GHz observations were combined with the available 5.5 and 9 GHz fluxes to construct SEDs. Ignoring the 9 GHz fluxes, the SEDs were consistent with UCHII regions showing a turnover between 5.5 and 17 GHz. Thus, interpolated 8 GHz fluxes between 5.5 GHz and 17 GHz were predicted and this interpolation was used to correct the observed 9 GHz fluxes of the entire catalogue.

The nature of the 255 candidate UCHII regions, detected by the CORNISH-South survey at 5.5 GHz was confirmed using the physical properties and estimated 9GHz-5GHz spectral indices. The 9 GHz observed flux densities ignored in the SEDs, were empirically corrected using the 5.5 GHz to 22 GHz SEDs. The CORNISH-South UCHII regions are confined in the Galactic mid-plane as expected for very young massive star forming regions, fluxes were found to be in a range of 3 mJy to 2.413 Jy, and the majority of the sources are classified as resolved. 54% of the sample a found between the optically thin and optically thick limit, with most of the sources near the optically thin limit.

4.2 Future Work

To confirm the nature of the UCHII regions other derived properties that were not calculated in this work can provide great contribution. Such properties being distances, luminosities, physical sizes, Lyman continuum fluxes, emission measures, electron densities and IR colours. The distribution of these properties will allow the characterization of the CORNISH-South UCHII regions to be more accurate.

To extend the SEDs to lower frequency there is also the 1.4 GHz fluxes from the MeerKAT Galactic plane survey [Goedhart et al. in prep.].

Higher resolution observations can be done to resolve the UCHII regions that are still unresolved at 22 GHz.

The method implemented by Kalcheva (2018) (radio-only, mid-IR and combined multi-resolution) to classify the morphology of the CORNISH-North UCHII regions can be performed to classify the morphology for the whole CORNISH-South UCHII regions.

References

- Arthur, S Jane and Hoare, MG (2006). “Hydrodynamics of cometary compact H II regions”.
In: *The Astrophysical Journal Supplement Series* 165.1, p. 283.
- Baraffe, Isabelle, Chabrier, Gilles, Allard, France, and Hauschildt, PH (2002). “Evolutionary models for low-mass stars and brown dwarfs: Uncertainties and limits at very young ages”.
In: *Astronomy & Astrophysics* 382.2, pp. 563–572.
- Benjamin, Robert A, Churchwell, E, Babler, Brian L, Bania, TM, Clemens, Dan P, Cohen, Martin, Dickey, John M, Indebetouw, Rémy, Jackson, James M, Kobulnicky, Henry A, et al. (2003). “GLIMPSE. I. An SIRTf legacy project to map the inner galaxy”. In: *Publications of the Astronomical Society of the Pacific* 115.810, p. 953.
- Blitz, Leo (1991). “Star forming giant molecular clouds”. In: *The Physics of Star Formation and Early Stellar Evolution*, pp. 3–34.
- Briggs, Daniel S, Schwab, Frederic R, and Sramek, Richard A (1999). “Imaging”. In: *Synthesis Imaging in Radio Astronomy II*. Vol. 180, p. 127.
- Burke, Bernard F, Graham-Smith, Francis, and Wilkinson, Peter N (2019). *An introduction to radio astronomy*. Cambridge University Press.
- Carey, SJ, Noriega-Crespo, A, Mizuno, DR, Shenoy, S, Paladini, R, Kraemer, KE, Price, SD, Flagey, N, Ryan, E, Ingalls, JG, et al. (2009). “MIPSGAL: A Survey of the Inner Galactic Plane at 24 and 70 μm ”. In: *Publications of the Astronomical Society of the Pacific* 121.875, p. 76.

- Carroll, Bradley W. (2017). *An introduction to modern astrophysics*. eng. Second edition. Cambridge: Cambridge University Press. ISBN: 9781108380980.
- Churchwell, Ed (2002). “ULTRA-COMPACT HII REGIONS AND MASSIVE STAR FORMATION”. eng. In: *Annual review of astronomy and astrophysics* 40.1, pp. 27–62. ISSN: 0066-4146.
- Churchwell, Ed, Babler, Brian L, Meade, Marilyn R, Whitney, Barbara A, Benjamin, Robert, Indebetouw, Remy, Cyganowski, Claudia, Robitaille, Thomas P, Povich, Matthew, Watson, Christer, et al. (2009). “The Spitzer/GLIMPSE surveys: a new view of the Milky Way”. In: *Publications of the Astronomical Society of the Pacific* 121.877, p. 213.
- De Pree, CG, Wilner, DJ, Deblasio, J, Mercer, AJ, and Davis, LE (2005). “The morphologies of ultracompact H II regions in W49A and Sagittarius B2: The prevalence of shells and a modified classification scheme”. In: *The Astrophysical Journal* 624.2, p. L101.
- Deharveng, L, Schuller, F, Anderson, LD, Zavagno, Annie, Wyrowski, F, Menten, KM, Bronfman, L, Testi, L, Walmsley, CM, and Wienen, M (2010). “A gallery of bubbles-The nature of the bubbles observed by Spitzer and what ATLASGAL tells us about the surrounding neutral material”. In: *Astronomy & Astrophysics* 523, A6.
- Dyson, JE, Williams, RJR, and Redman, MP (1995). “Clumpy ultracompact H II regions—I. Fully supersonic wind-blown models”. In: *Monthly Notices of the Royal Astronomical Society* 277.2, pp. 700–704.
- Elmegreen, Bruce G (1997). “Observations and theory of dynamical triggers for star formation”. In: *arXiv preprint astro-ph/9712352*.
- Hancock, P. J., Murphy, T., Gaensler, B. M., Hopkins, A., and Curran, J. R. (Apr. 2012). “Compact continuum source finding for next generation radio surveys”. In: *Monthly Notices of the Royal Astronomical Society* 422.2, pp. 1812–1824. ISSN: 0035-8711. DOI: 10.1111/j.1365-2966.2012.20768.x. eprint: <https://academic.oup.com/mnras/article-pdf/422/2/1812/3523167/mnras0422-1812.pdf>. URL: <https://doi.org/10.1111/j.1365-2966.2012.20768.x>.

- Hoare, M. G., Kurtz, S. E., Lizano, S., Keto, E., and Hofner, P. (Jan. 2007). “Ultracompact Hii Regions and the Early Lives of Massive Stars”. In: ed. by Bo Reipurth, David Jewitt, and Klaus Keil, p. 181. arXiv: [astro-ph/0603560](https://arxiv.org/abs/astro-ph/0603560) [astro-ph].
- Hoare, MG, Purcell, CR, Churchwell, EB, Diamond, Philip, Cotton, WD, Chandler, CJ, Smethurst, S, Kurtz, SE, Mundy, LG, Dougherty, SM, et al. (2012). “The coordinated radio and infrared survey for high-mass star formation (the CORNISH survey). I. Survey design”. In: *Publications of the Astronomical Society of the Pacific* 124.919, p. 939.
- Högbom, JA (1974). “Aperture synthesis with a non-regular distribution of interferometer baselines”. In: *Astronomy and Astrophysics Supplement Series* 15, p. 417.
- Hughes, VA and Wouterloot, JGA (1984). “The star-forming region in Cepheus A”. In: *Astrophysical Journal* 276, pp. 204–210.
- Irabor, T, Hoare, MG, Oudmaijer, RD, Urquhart, JS, Kurtz, S, Lumsden, SL, Purcell, CR, Zijlstra, AA, and Umana, G (2018). “The coordinated radio and infrared survey for high-mass star formation–IV. A new radio-selected sample of compact galactic planetary nebulae”. In: *Monthly Notices of the Royal Astronomical Society* 480.2, pp. 2423–2448.
- Irabor, T., Hoare, M. G., Burton, M., Cotton, W. D., Diamond, P., Dougherty, S., Ellingsen, S. P., Fender, R., Fuller, G. A., Garrington, S., Goldsmith, P. F., Green, J., Gunn, A. G., Jackson, J., Kurtz, S., Lumsden, S. L., Marti, J., McDonald, I., Molinari, S., Moore, T. J., Mutale, M., Muxlow, T., O’Brien, T., Oudmaijer, R. D., Paladini, R., Pandian, J. D., Paredes, J. M., Richards, A. M. S., Sanchez-Monge, A., Spencer, R., Thompson, M. A., Umana, G., Urquhart, J. S., Wieringa, M., and Zijlstra, A. (Jan. 2023). “The Co-Ordinated radio and infrared survey for high-mass star formation - V. The CORNISH-South survey and catalogue”. In: DOI: [10.1093/mnras/stad005](https://doi.org/10.1093/mnras/stad005). arXiv: [2301.01988](https://arxiv.org/abs/2301.01988) [astro-ph.GA].
- Israel, F. P. (Nov. 1977). “Aperture synthesis observations of galactic H II regions. VII. A “quick look” survey of galactic H II regions.” In: 61, p. 377.
- (1978). “H II regions and CO clouds–The blister model”. In: *Astronomy and Astrophysics* 70, pp. 769–775.

- Kalcheva, Ivayla (2018). “The Ultra-Compact H II Region Population of the Galaxy”. PhD thesis. University of Leeds.
- Kim, Kee-Tae and Koo, Bon-Chul (2001). “Radio continuum and recombination line study of ultracompact h ii regions with extended envelopes”. In: *The Astrophysical Journal* 549.2, p. 979.
- Kudritzki, Rolf (Sept. 2002). “Line-driven Winds, Ionizing Fluxes, and Ultraviolet Spectra of Hot Stars at Extremely Low Metallicity. I. Very Massive O Stars”. In: *The Astrophysical Journal* 577, p. 389. DOI: 10.1086/342178.
- Kurtz, S., Churchwell, E., and Wood, D. O. S. (Apr. 1994). “Ultracompact H II Regions. II. New High-Resolution Radio Images”. In: 91, p. 659. DOI: 10.1086/191952.
- Kurtz, Stanley E, Watson, Alan M, Hofner, Peter, and Otte, Birgit (1999). “Ultracompact H II Regions with Extended Radio-Continuum Emission”. In: *The Astrophysical Journal* 514.1, p. 232.
- Lawrence, A, Warren, SJ, Almaini, O, Edge, AC, Hambly, NC, Jameson, RF, Lucas, P, Casali, M, Adamson, A, Dye, S, et al. (2007). “The UKIRT infrared deep sky survey (UKIDSS)”. In: *Monthly Notices of the Royal Astronomical Society* 379.4, pp. 1599–1617.
- Lawrence, Aller H et al. (1991). *Atoms, stars, and nebulae*. Cambridge University Press.
- Longair, Malcolm S. (1992). *High energy astrophysics*. eng. Second edition. Cambridge: Cambridge University Press. ISBN: 0521387736.
- Lucas, PW, Hoare, Melvin G, Longmore, A, Schröder, AC, Davis, Christopher J, Adamson, A, Bandyopadhyay, Reba M, De Grijs, Richard, Smith, M, Gosling, Amanda, et al. (2008). “The UKIDSS Galactic plane survey”. In: *Monthly Notices of the Royal Astronomical Society* 391.1, pp. 136–163.
- Lumsden, Stuart and Hoare, Melvin (1996). “An IR Study of the Velocity Structure of the Cometary Compact HII region G29. 96-0.02”. In: *arXiv preprint astro-ph/9603114*.
- Mezger, PG and Henderson, AP (1967). “Galactic H II regions. I. Observations of their continuum radiation at the frequency 5 GHz”. In: *The Astrophysical Journal* 147, p. 471.

- Molinari, S, Swinyard, B, Bally, J, Barlow, Mike, Bernard, J-P, Martin, P, Moore, T, Noriega-Crespo, A, Plume, R, Testi, L, et al. (2010). “Hi-gal: The herschel infrared galactic plane survey”. In: *Publications of the Astronomical Society of the Pacific* 122.889, p. 314.
- Molinari, Sergio, Schisano, EUGENIO, Elia, D, Pestalozzi, M, Traficante, ALESSIO, Pezzuto, Stefano, Swinyard, BM, Noriega-Crespo, A, Bally, J, Moore, TJJ, et al. (2016). “Hi-GAL, the Herschel infrared Galactic Plane Survey: photometric maps and compact source catalogues- First data release for the inner Milky Way: + 68° l- 70°”. In: *Astronomy & Astrophysics* 591, A149.
- Motte, Frederique, Bontemps, Sylvain, and Louvet, Fabien (2018). “High-mass star and massive cluster formation in the Milky Way”. In: *Annual Review of Astronomy and Astrophysics* 56, pp. 41–82.
- Norris, Ray P, Afonso, José, Appleton, Phil N, Boyle, Brian J, Ciliegi, Paolo, Croom, Scott M, Huynh, Minh T, Jackson, Carole A, Koekemoer, Anton M, Lonsdale, Carol J, et al. (2006). “Deep ATLAS radio observations of the Chandra Deep Field-South/Spitzer wide-area infrared extragalactic field”. In: *The Astronomical Journal* 132.6, p. 2409.
- Oster, Ludwig (1961). “Emission, absorption, and conductivity of a fully ionized gas at radio frequencies”. In: *Reviews of Modern Physics* 33.4, p. 525.
- Palla, Francesco and Stahler, Steven W (1999). “Star formation in the Orion nebula cluster”. In: *The Astrophysical Journal* 525.2, p. 772.
- Pereira, V, López-Santiago, J, Miceli, Marco, Bonito, Rosaria, and De Castro, E (2016). “Modeling nonthermal emission from stellar bow shocks”. In: *Astronomy & Astrophysics* 588, A36.
- Perley, Richard A, Taylor, GB, and Carilli, CL (1999). “Synthesis imaging in radio astronomy ii”. In: *ASP Conference Series, San Francisco: NRAO/NMIMT*. Vol. 180, pp. 383–395.
- Pokhrel, Riway, Myers, Philip C, Dunham, Michael M, Stephens, Ian W, Sadavoy, Sarah I, Zhang, Qizhou, Bourke, Tyler L, Tobin, John J, Lee, Katherine I, Gutermuth, Robert A, et al. (2018). “Hierarchical fragmentation in the Perseus molecular cloud: from the cloud scale to protostellar objects”. In: *The Astrophysical Journal* 853.1, p. 5.

- Purcell, CR, Hoare, MG, Cotton, WD, Lumsden, SL, Urquhart, JS, Chandler, C, Churchwell, EB, Diamond, P, Dougherty, SM, Fender, RP, et al. (2013). “The coordinated radio and infrared survey for high-mass star formation. II. Source catalog”. In: *The Astrophysical Journal Supplement Series* 205.1, p. 1.
- Purser, SJD, Lumsden, SL, Hoare, MG, and Kurtz, S (2021). “A Galactic survey of radio jets from massive protostars”. In: *Monthly Notices of the Royal Astronomical Society* 504.1, pp. 338–355.
- Purser, SJD, Lumsden, SL, Hoare, MG, Urquhart, JS, Cunningham, Nichol, Purcell, CR, Brooks, KJ, Garay, Guido, Gúzman, AE, and Voronkov, Maxim A (2016). “A search for ionized jets towards massive young stellar objects”. In: *Monthly Notices of the Royal Astronomical Society* 460.1, pp. 1039–1053.
- Reid, Mark J and Ho, Paul TP (1985). “G34. 3+ 0.2-A’cometary’H II region”. In: *Astrophysical Journal, Part 2-Letters to the Editor (ISSN 0004-637X)*, vol. 288, Jan. 1, 1985, p. L17-L19. 288, pp. L17–L19.
- Ryle, M (1955). “The application of interferometric methods in radio astronomy”. In: *Vistas in Astronomy* 1, pp. 532–541.
- (1968). “The counts of radio sources”. In: *Annual Review of Astronomy and Astrophysics* 6.1, pp. 249–266.
- Sahai, Raghvendra, Morris, Mark R, and Villar, Gregory G (2011). “Young planetary nebulae: Hubble Space Telescope imaging and a new morphological classification system”. In: *The Astronomical Journal* 141.4, p. 134.
- Sault, R. J., Teuben, P. J., and Wright, M. C. H. (Jan. 1995). “A Retrospective View of MIRIAD”. In: *Astronomical Data Analysis Software and Systems IV*. Ed. by R. A. Shaw, H. E. Payne, and J. J. E. Hayes. Vol. 77. Astronomical Society of the Pacific Conference Series, p. 433. arXiv: astro-ph/0612759 [astro-ph].
- Scheuer, PAG (1960). “The absorption coefficient of a plasma at radio frequencies”. In: *Monthly Notices of the Royal Astronomical Society* 120.3, pp. 231–241.

- Schuller, F, Menten, KM, Contreras, Y, Wyrowski, F, Schilke, P, Bronfman, L, Henning, Thomas, Walmsley, CM, Beuther, H, Bontemps, Sylvain, et al. (2009). “ATLASGAL–The APEX telescope large area survey of the galaxy at 870 m”. In: *Astronomy & Astrophysics* 504.2, pp. 415–427.
- Stahler, Steven William. (2004). *The formation of stars : Steven W. Stahler and Francesco Palla*. eng. Weinheim: Wiley-VCH.
- Steggles, HG, Hoare, MG, and Pittard, JM (2017). “Hydrodynamical models of cometary H ii regions”. In: *Monthly Notices of the Royal Astronomical Society* 466.4, pp. 4573–4591.
- Tenorio-Tagle, G (1979). “The gas dynamics of H II regions. I-The champagne model”. In: *Astronomy and Astrophysics* 71, pp. 59–65.
- Thompson, A Richard (1989). “The interferometer in practice”. In: *Synthesis Imaging in Radio Astronomy*. Vol. 6, p. 11.
- Tofani, G, Felli, M, Taylor, GB, and Hunter, TR (1995). “Exploring the engines of molecular outflows. Radio continuum and H₂O maser observations.” In: *Astronomy and Astrophysics Supplement Series* 112, p. 299.
- Urquhart, J. S., Busfield, A. L., Hoare, M. G., Lumsden, S. L., Clarke, A. J., Moore, T. J. T., Mottram, J. C., and Oudmaijer, R. D. (Jan. 2007). “The RMS survey. Radio observations of candidate massive YSOs in the southern hemisphere”. In: 461.1, pp. 11–23. DOI: 10.1051/0004-6361:20065837. arXiv: astro-ph/0605738 [astro-ph].
- Urquhart, JS, Hoare, Melvin G, Purcell, CR, Lumsden, Stuart L, Oudmaijer, Rene D, Moore, Toby JT, Busfield, AL, Mottram, Joseph C, and Davies, Ben (2009). “The RMS survey-6 cm continuum VLA observations towards candidate massive YSOs in the northern hemisphere”. In: *Astronomy & Astrophysics* 501.2, pp. 539–551.
- Urquhart, JS, Thompson, MA, Moore, TJT, Purcell, CR, Hoare, MG, Schuller, F, Wyrowski, F, Csengeri, T, Menten, KM, Lumsden, SL, et al. (2013). “ATLASGAL–properties of compact H ii regions and their natal clumps”. In: *Monthly Notices of the Royal Astronomical Society* 435.1, pp. 400–428.

- Van Buren, Dave, Mac Low, Mordecai-Mark, Wood, Douglas OS, and Churchwell, Ed (1990). “Cometary compact H II regions are stellar-wind bow shocks”. In: *The Astrophysical Journal* 353, pp. 570–578.
- Walsh, AJ, Burton, MG, Hyland, AR, and Robinson, Garry (1998). “Studies of ultracompact H ii regions—II. High-resolution radio continuum and methanol maser survey”. In: *Monthly Notices of the Royal Astronomical Society* 301.3, pp. 640–698.
- Walsh, Andrew J, Breen, SL, Britton, Tui, Brooks, KJ, Burton, Michael G, Cunningham, MR, Green, JA, Harvey-Smith, Lisa, Hindson, Luke, Hoare, Melvin G, et al. (2011). “The H₂O southern galactic plane survey (HOPS)—i. techniques and H₂O maser data”. In: *Monthly Notices of the Royal Astronomical Society* 416.3, pp. 1764–1821.
- Wenger, Trey V, Dickey, John M, Jordan, Christopher H, Balser, Dana S, Armentrout, William Paul, Anderson, LD, Bania, TM, Dawson, JR, McClure-Griffiths, Naomi M, and Shea, Jeanine (2019). “The Southern H ii Region Discovery Survey. I. The Bright Catalog”. In: *The Astrophysical Journal Supplement Series* 240.2, p. 24.
- Wilson, Thomas L, Rohlfs, Kristen, and Hüttemeister, Susanne (2009). *Tools of radio astronomy*. Vol. 5. Springer.
- Wood, Douglas OS and Churchwell, Ed (1989). “The morphologies and physical properties of ultracompact H II regions”. In: *The Astrophysical Journal Supplement Series* 69, pp. 831–895.
- Zinnecker, Hans and Yorke, Harold W (2007). “Toward Understanding Massive Star Formation”. eng. In: *Annual review of astronomy and astrophysics* 45.1, pp. 481–563. ISSN: 0066-4146.
-

Appendix A

Additional Figures and Tables for Chapter 2

A.1 Radio properties of the high resolution CORNISH-South UCHII regions

Table A.1 | Radio properties of the high resolution CORNISH-South UCHII regions at 17 GHz. For the not detected sources the Flux upper limits are included and they are preceded by "<".

Source name	RA (J2000)	DEC (J2000)	F_{17GHz} (mJy)	θ (arcsec)	T_b (K)	Optical depth
G295.1520-0.5882	11:43:25.245	-62:25:41.047	23.81 ± 0.82	0.37	185.47	0.02
G297.4570-0.7628	12:02:43.050	-63:06:55.807	5.35 ± 0.11	0.68	41.67	0.00
G297.6590-0.9720	12:04:08.506	-63:21:30.552	27.03 ± 0.36	7.00	210.55	0.02
G300.4010+0.5461	12:29:41.675	-62:13:07.684	15.57 ± 0.37	17.98	121.28	0.01
G302.0220+0.2539	12:43:31.493	-62:36:13.440	94.91 ± 1.28	7.03	739.31	0.08
G303.9390-0.6895	13:00:24.062	-63:32:31.793	36.93 ± 0.69	0.15	287.67	0.03
G305.7980-0.2415	13:16:42.608	-62:58:20.711	7.95 ± 0.21	8.28	61.93	0.01
G307.7360-0.5944	13:34:03.403	-63:04:04.999	4.81 ± 0.03	7.00	37.47	0.00
G308.0560-0.3961	13:36:32.177	-62:49:05.717	192.10 ± 2.90	0.46	1496.38	0.16
G311.1360-0.2373	14:02:09.913	-61:58:37.973	3.76 ± 0.07	0.46	29.25	0.00
G311.5960-0.3984	14:06:18.331	-62:00:15.132	11.48 ± 0.14	0.08	89.42	0.01
G311.6430-0.3800	14:06:38.726	-61:58:23.410	255.90 ± 5.3	0.56	1993.36	0.22
G312.3070+0.6608	14:09:24.924	-60:47:00.711	18.55 ± 0.39	0.22	144.50	0.01
G312.5480-0.2809	14:13:41.929	-61:36:26.459	10.01 ± 0.19	8.46	77.95	0.01
G314.2200+0.2727	14:25:12.807	-60:31:38.993	22.83 ± 0.36	11.86	177.84	0.02
G317.4290-0.5609	14:51:37.645	-60:00:20.206	20.23 ± 0.24	0.27	157.58	0.02
G317.8890-0.0584	14:53:06.276	-59:20:59.895	8.73 ± 0.45	0.48	68.00	0.01
G318.0470+0.0855	14:53:41.667	-59:09:01.809	1.89 ± 0.04	0.58	14.72	0.00
G323.4590-0.0787	15:29:19.376	-56:31:22.303	443.0 ± 11.0	0.60	3450.80	0.42
G326.4480-0.7484	15:49:18.665	-55:16:52.005	5.00 ± 0.27	0.15	38.95	0.00
G327.6370-0.1462	15:53:05.168	-54:03:55.829	2.70 ± 0.11	0.23	21.03	0.00
G327.9010+0.1539	15:53:10.840	-53:39:58.250	2.48 ± 0.14	0.63	19.32	0.00
G329.2720+0.1148	16:00:21.764	-52:48:47.717	6.75 ± 0.23	0.23	52.58	0.01

Table A.2 | continued from previous page.

Source name	RA (J2000)	DEC (J2000)	F_{17GHz} (mJy)	θ (arcsec)	T_b (K)	Optical depth
G329.5240+0.0846	16:01:45.053	-52:40:15.430	5.56 ± 0.35	0.33	43.31	0.00
G329.8150+0.1407	16:02:56.892	-52:26:13.377	6.71 ± 0.34	9.09	52.27	0.01
G330.2950-0.3929	16:07:37.928	-52:30:57.514	813.05 ± 5.12	33.35	6333.34	1.00
G330.9280-0.4070	16:10:44.847	-52:05:51.167	7.61 ± 0.29	0.74	59.28	0.01
G331.5120-0.1027	16:12:10.014	-51:28:37.383	356.70 ± 3.51	0.49	2778.55	0.33
G333.0290-0.0631	16:18:56.868	-50:23:54.109	26.05 ± 0.80	0.19	202.92	0.02
G333.3400-0.1279	16:20:36.931	-50:13:35.695	3.06 ± 0.11	0.27	23.82	0.00
G333.3870+0.0318	16:20:07.539	-50:04:47.062	6.43 ± 0.21	0.45	50.09	0.01
G335.3900-0.2905	16:30:10.151	-48:52:23.433	47.20 ± 4.20	0.47	367.67	0.04
G336.0270-0.8170	16:35:08.608	-48:45:59.442	15.33 ± 0.73	9.37	119.41	0.01
G336.8640+0.0048	16:34:54.408	-47:35:37.168	23.00 ± 1.00	0.31	179.16	0.02
G336.9830-0.1832	16:36:12.409	-47:37:58.049	53.80 ± 4.7	0.53	419.08	0.04
G337.4040-0.4024	16:38:50.560	-47:28:02.934	141.80 ± 2.40	8.38	1104.57	0.12
G337.6320-0.0781	16:38:19.025	-47:04:51.171	30.52 ± 1.24	7.32	237.74	0.02
G337.7050-0.0532	16:38:29.638	-47:00:35.827	156.60 ± 5.80	0.50	1219.85	0.13
G337.7130+0.0879	16:37:54.446	-46:54:36.981	12.23 ± 0.51	0.28	95.27	0.01
G337.8440-0.3734	16:40:26.693	-47:07:13.615	26.75 ± 0.91	0.23	208.37	0.02
G338.2710-0.2924	16:41:44.241	-46:44:45.106	8.92 ± 0.61	0.59	69.484	0.01
G338.3250+0.1547	16:39:59.856	-46:24:32.841	< 8.12	-	-	-
G338.3620+0.1409	16:40:11.871	-46:23:27.547	9.52 ± 0.19	0.25	74.19	0.01
G338.5660+0.1096	16:41:07.147	-46:15:30.073	5.57 ± 0.53	1.10	43.39	0.00
G339.4670+0.0837	16:44:38.158	-45:35:48.274	6.43 ± 0.29	0.37	50.09	0.01
G339.9800-0.5386	16:49:14.733	-45:36:32.276	62.70 ± 3.40	7.21	488.41	0.05
G340.2490-0.3717	16:48:05.193	-45:05:10.455	50.75 ± 1.90	15.60	395.32	0.04
G340.7850-0.0959	16:50:14.819	-44:42:26.509	17.25 ± 0.57	5.35	134.37	0.01
G341.9740+0.2251	16:53:05.132	-43:35:10.145	63.30 ± 3.60	0.36	493.08	0.05
G342.7090+0.1253	16:56:03.466	-43:04:40.873	8.00 ± 0.34	7.03	62.32	0.01
G343.9290+0.1249	17:00:10.889	-42:07:19.618	57.64 ± 0.99	5.27	448.99	0.05
G344.5820-0.0238	17:02:57.829	-41:41:53.778	8.68 ± 0.19	6.96	67.63	0.01
G344.9100+0.2469	17:02:53.526	-41:16:21.238	15.11 ± 0.36	8.42	117.70	0.01
G345.1980-0.0301	17:04:59.431	-41:12:45.911	5.18 ± 0.10	0.34	40.36	0.00
G345.4070-0.9516	17:09:35.425	-41:35:55.117	860.68 ± 18.77	9.24	6704.36	1.11
G345.5470-0.0803	17:06:19.334	-40:57:53.254	91.59 ± 1.21	15.67	713.48	0.07
G345.9880+0.4696	17:05:24.913	-40:16:52.907	3.74 ± 0.28	0.22	29.13	0.00
G346.1960+0.0402	17:07:52.279	-40:22:24.971	4.48 ± 0.33	1.02	34.90	0.00
G346.2330-0.3197	17:09:30.332	-40:33:31.816	22.531 ± 0.27	0.14	175.51	0.02
G347.3050+0.0148	17:11:25.180	-39:29:51.626	8.17 ± 0.33	0.79	63.64	0.01
G347.6280+0.1482	17:11:51.039	-39:09:29.012	167.50 ± 8.80	0.47	1304.76	0.14
G347.8980+0.0436	17:13:06.294	-39:00:05.652	5.31 ± 0.37	5.60	41.36	0.00
G348.3510+0.1515	17:14:01.247	-38:34:15.359	4.50 ± 0.17	0.47	35.09	0.00
G348.5500-0.3386	17:16:39.222	-38:41:41.145	22.47 ± 0.41	0.65	175.03	0.02
G348.6130-0.9099	17:19:14.242	-38:58:21.590	4.49 ± 0.33	9.20	35.00	0.00
G348.6490+0.0228	17:15:26.536	-38:24:16.545	4.02 ± 0.25	0.48	31.31	0.00
G348.7280-1.0417	17:20:07.891	-38:57:14.485	171.02 ± 20.56	11.39	1332.18	0.14
G348.8920-0.1796	17:17:00.135	-38:19:28.530	186.82 ± 8.37	7.60	1455.26	0.16
G349.7210+0.1213	17:18:11.091	-37:28:23.579	41.52 ± 0.90	9.84	323.42	0.03
G350.0150+0.4329	17:17:45.459	-37:03:12.640	107.80 ± 6.90	8.14	839.72	0.09
G350.1110+0.0882	17:19:25.609	-37:10:04.554	< 43.01	-	-	-
G350.1210+0.0592	17:19:35.680	-37:10:56.093	303.20 ± 10.74	10.66	2361.81	0.27

Table A.3 | Radio properties of the high resolution CORNISH–South UCHII regions at 22 GHz. For the not detected sources the Flux upper limits are included and they are preceded by ”<”.

Source name	RA (J2000)	DEC (J2000)	F_{22GHz} (mJy)	θ (arcsec)	T_b (K)	Optical depth
G295.1520-0.5882	11:43:25.244	-62:25:41.032	20.92 ± 0.72	0.38	168.43	0.02
G297.4570-0.7628	12:02:43.051	-63:06:55.824	5.39 ± 0.41	0.71	43.39	0.00
G297.6590-0.9720	12:04:07.321	-63:21:37.014	23.60 ± 0.53	6.69	190.00	0.02
G300.4010+0.5461	12:29:41.664	-62:13:07.123	7.1 ± 1.0	1.71	57.16	0.01
G302.0220+0.2539	12:43:31.491	-62:36:13.407	81.63 ± 1.76	6.53	657.20	0.07
G303.9390-0.6895	13:00:24.077	-63:32:31.774	36.04 ± 0.48	4.41	290.16	0.03
G305.7980-0.2415	13:16:42.609	-62:58:20.692	< 3.21	-	-	-
G307.7360-0.5944	13:34:03.407	-63:04:05.046	3.01 ± 0.24	0.42	24.23	0.00
G308.0560-0.3961	13:36:32.179	-62:49:05.698	177.10 ± 2.50	0.44	1425.83	0.15
G311.1360-0.2373	14:02:09.909	-61:58:37.993	3.30 ± 0.29	0.50	26.57	0.00
G311.5960-0.3984	14:06:18.331	-62:00:15.130	11.67 ± 0.35	0.10	93.96	0.01
G311.6430-0.3800	14:06:38.729	-61:58:23.418	226.80 ± 2.20	0.52	1825.97	0.20
G312.3070+0.6608	14:09:24.925	-60:47:00.705	18.12 ± 0.29	0.23	145.88	0.01
G312.5480-0.2809	14:13:41.926	-61:36:26.493	8.78 ± 0.61	0.81	70.67	0.01
G314.2200+0.2727	14:25:12.564	-60:31:38.993	19.50 ± 0.09	14.52	156.99	0.02
G317.4290-0.5609	14:51:37.646	-60:00:20.178	22.75 ± 0.13	0.25	183.16	0.02
G317.8890-0.0584	14:53:06.278	-59:20:59.917	8.00 ± 0.57	0.49	64.41	0.01
G318.0470+0.0855	14:53:41.663	-59:09:01.805	1.40 ± 0.02	4.52	11.27	0.00
G323.4590-0.0787	15:29:19.500	-56:31:20.650	494.00 ± 16.0	0.54	3977.19	0.51
G326.4480-0.7484	15:49:18.662	-55:16:52.013	4.74 ± 0.34	0.17	38.16	0.00
G327.6370-0.1462	15:53:05.169	-54:03:55.867	2.470 ± 0.16	0.21	19.89	0.00
G327.9010+0.1539	15:53:10.839	-53:39:58.236	2.24 ± 0.20	0.67	18.03	0.00
G329.2720+0.1148	16:00:21.763	-52:48:47.717	6.78 ± 0.37	0.22	54.59	0.01
G329.5240+0.0846	16:01:45.051	-52:40:15.442	5.17 ± 0.38	0.31	41.62	0.00
G329.8150+0.1407	16:02:56.880	-52:26:13.417	5.78 ± 1.13	5.62	46.53	0.01
G330.2950-0.3929	16:07:38.106	-52:30:53.948	644.30 ± 2.89	33.45	5187.26	0.73
G330.9280-0.4070	16:10:44.846	-52:05:51.206	6.96 ± 0.75	0.88	56.03	0.01
G331.5120-0.1027	16:12:10.010	-51:28:37.365	349.00 ± 18	0.48	2809.80	0.33
G333.0290-0.0631	16:18:56.867	-50:23:54.108	25.70 ± 1.1	0.14	206.91	0.02
G333.3400-0.1279	16:20:36.933	-50:13:35.731	2.50 ± 0.19	0.31	20.13	0.00
G333.3870+0.0318	16:20:07.538	-50:04:47.037	5.68 ± 0.47	0.54	45.73	0.00
G335.3900-0.2905	16:30:10.158	-48:52:23.623	60.00 ± 2.8	0.21	483.06	0.05
G336.0270-0.8170	16:35:08.621	-48:45:59.808	6.76 ± 1.10	4.41	54.42	0.01
G336.8640+0.0048	16:34:54.422	-47:35:37.440	30.30 ± 1.0	0.16	243.95	0.02
G336.9830-0.1832	16:36:12.415	-47:37:58.286	55.50 ± 4.8	0.33	446.83	0.05
G337.4040-0.4024	16:38:50.472	-47:28:03.066	136.46 ± 2.31	5.69	1098.64	0.12
G337.6320-0.0781	16:38:19.025	-47:04:51.096	13.83 ± 2.43	5.10	111.35	0.01
G337.7050-0.0532	16:38:29.638	-47:00:35.811	117.70 ± 8.10	0.60	947.60	0.10
G337.7130+0.0879	16:37:54.452	-46:54:36.901	12.38 ± 1.05	0.46	99.65	0.01
G337.8440-0.3734	16:40:26.692	-47:07:13.607	16.03 ± 0.53	0.18	129.05	0.02
G338.2710-0.2924	16:41:44.233	-46:44:45.059	8.93 ± 2.28	0.31	71.92	0.01
G338.3250+0.1547	16:39:59.856	-46:24:32.841	< 7.65	-	-	-
G338.3620+0.1409	16:40:11.871	-46:23:27.555	6.35 ± 1.92	2.62	51.12	0.01
G338.5660+0.1096	16:41:07.147	-46:15:30.073	< 3.36	-	-	-
G339.4670+0.0837	16:44:38.155	-45:35:48.344	3.81 ± 0.42	0.28	30.67	0.00
G339.9800-0.5386	16:49:14.735	-45:36:32.274	46.07 ± 1.37	5.47	370.91	0.04
G340.2490-0.3717	16:48:05.200	-45:05:10.598	35.00 ± 4.97	15.10	281.78	0.03
G340.7850-0.0959	16:50:14.816	-44:42:26.626	16.09 ± 0.92	3.55	129.54	0.01

Table A.4 | continued from previous page.

Source name	RA (J2000)	DEC (J2000)	F_{22GHz} (mJy)	θ (arcsec)	T_b (K)	Optical depth
G341.9740+0.2251	16:53:05.133	-43:35:10.168	58.83 ± 0.75	0.36	473.62	0.05
G342.7090+0.1253	16:56:03.455	-43:04:40.884	7.80 ± 1.32	5.59	62.79	0.01
G343.9290+0.1249	17:00:10.889	-42:07:19.636	53.97 ± 0.56	5.15	434.51	0.04
G344.5820-0.0238	17:02:57.902	-41:41:53.498	27.13 ± 2.47	4.21	218.42	0.02
G344.9100+0.2469	17:02:53.529	-41:16:21.238	8.44 ± 0.38	4.04	67.95	0.01
G345.1980-0.0301	17:04:59.431	-41:12:45.924	3.45 ± 0.13	0.22	27.78	0.00
G345.4070-0.9516	17:09:35.425	-41:35:54.986	748.22 ± 4.66	7.54	6023.92	0.92
G345.5470-0.0803	17:06:19.334	-40:57:53.277	79.79 ± 4.21	12.16	642.37	0.07
G345.9880+0.4696	17:05:24.913	-40:16:52.933	2.96 ± 0.64	0.25	23.83	0.00
G346.1960+0.0402	17:07:52.279	-40:22:24.912	3.92 ± 0.45	4.21	31.56	0.00
G346.2330-0.3197	17:09:30.332	-40:33:31.834	21.39 ± 1.09	-	172.21	0.02
G347.3050+0.0148	17:11:25.178	-39:29:51.695	7.96 ± 0.60	0.94	64.09	0.01
G347.6280+0.1482	17:11:51.034	-39:09:29.036	154.20 ± 1.63	0.38	1241.46	0.13
G347.8980+0.0436	17:13:06.308	-39:00:05.839	4.57 ± 1.14	6.58	36.79	0.00
G348.3510+0.1515	17:14:01.248	-38:34:15.408	3.93 ± 2.44	0.47	31.61	0.00
G348.5500-0.3386	17:16:39.220	-38:41:41.106	18.69 ± 1.19	0.68	150.47	0.02
G348.6130-0.9099	17:19:11.886	-38:58:21.338	1.50 ± 0.91	4.69	12.08	0.00
G348.6490+0.0228	17:15:26.533	-38:24:16.622	3.88 ± 1.34	3.76	31.24	0.00
G348.7280-1.0417	17:20:07.918	-38:57:14.413	111.90 ± 5.04	5.96	900.91	0.09
G348.8920-0.1796	17:17:00.148	-38:19:27.913	132.95 ± 1.29	6.35	1070.38	0.11
G349.7210+0.1213	17:18:11.095	-37:28:23.531	40.93 ± 0.98	7.60	329.53	0.03
G350.0150+0.4329	17:17:45.460	-37:03:12.679	116.35 ± 1.60	6.17	936.73	0.10
G350.1110+0.0882	17:19:25.609	-37:10:04.554	< 32.02	-	-	-
G350.1210+0.0592	17:19:35.673	-37:10:56.292	220.20 ± 3.56	11.03	1772.831	0.20

Table A.5 | Radio properties of the individual sources that compose the multiple merged sources at both 17 and 22GHz. Source G349.7210+0.1213 is a point source and an upper limit on its size cannot be determined

Source name	RA (J2000)	DEC (J2000)	F_{17GHz} (mJy)	F_{22GHz} (mJy)	θ_{17GHz} (arcsec)	θ_{22GHz} (arcsec)
G314.2200+0.2727A	14:25:12.815	-60:31:40.416	2.37 ± 0.15	1.91 ± 0.06	0.26	0.17
G314.2200+0.2727B	14:25:12.568	-60:31:38.660	11.07 ± 0.40	8.6 ± 0.42	0.57	0.43
G314.2200+0.2727C	14:25:13.054	-60:31:39.254	8.29 ± 0.50	6.77 ± 0.35	0.38	0.31
G329.8150+0.1407A	16:02:56.907	-52:26:13.302	4.53 ± 0.84	3.40 ± 0.69	0.72	0.65
G329.8150+0.1407B	16:02:56.813	-52:26:13.932	2.60 ± 0.7	1.76 ± 0.26	0.33	0.20
G330.2950-0.3929A	16:07:37.457	-52:31:01.520	256.00 ± 11	186.00 ± 14	1.57	1.49
G330.2950-0.3929B	16:07:38.103	-52:30:53.956	393.00 ± 12	305.00 ± 18	0.82	0.79
G330.2950-0.3929C	16:07:38.854	-52:30:59.938	138.00 ± 9.8	69.00 ± 6.7	0.73	0.61
G344.5820-0.0238A	17:02:57.753	-41:41:53.709	11.07 ± 0.63	16.6 ± 1.0	1.25	-
G344.5820-0.0238B	17:02:57.836	-41:41:53.788	7.61 ± 0.60	13.42 ± 0.09	0.67	-
G349.7210+0.1213A	17:18:11.094	-37:28:23.560	31.60 ± 2.20	25.4 ± 1.8	0.47	0.51
G349.7210+0.1213B	17:18:11.218	-37:28:24.318	10.48 ± 0.89	10.52 ± 0.64	0.35	0.38

A.2 Images of the high resolution CORNISH-South UCHII regions

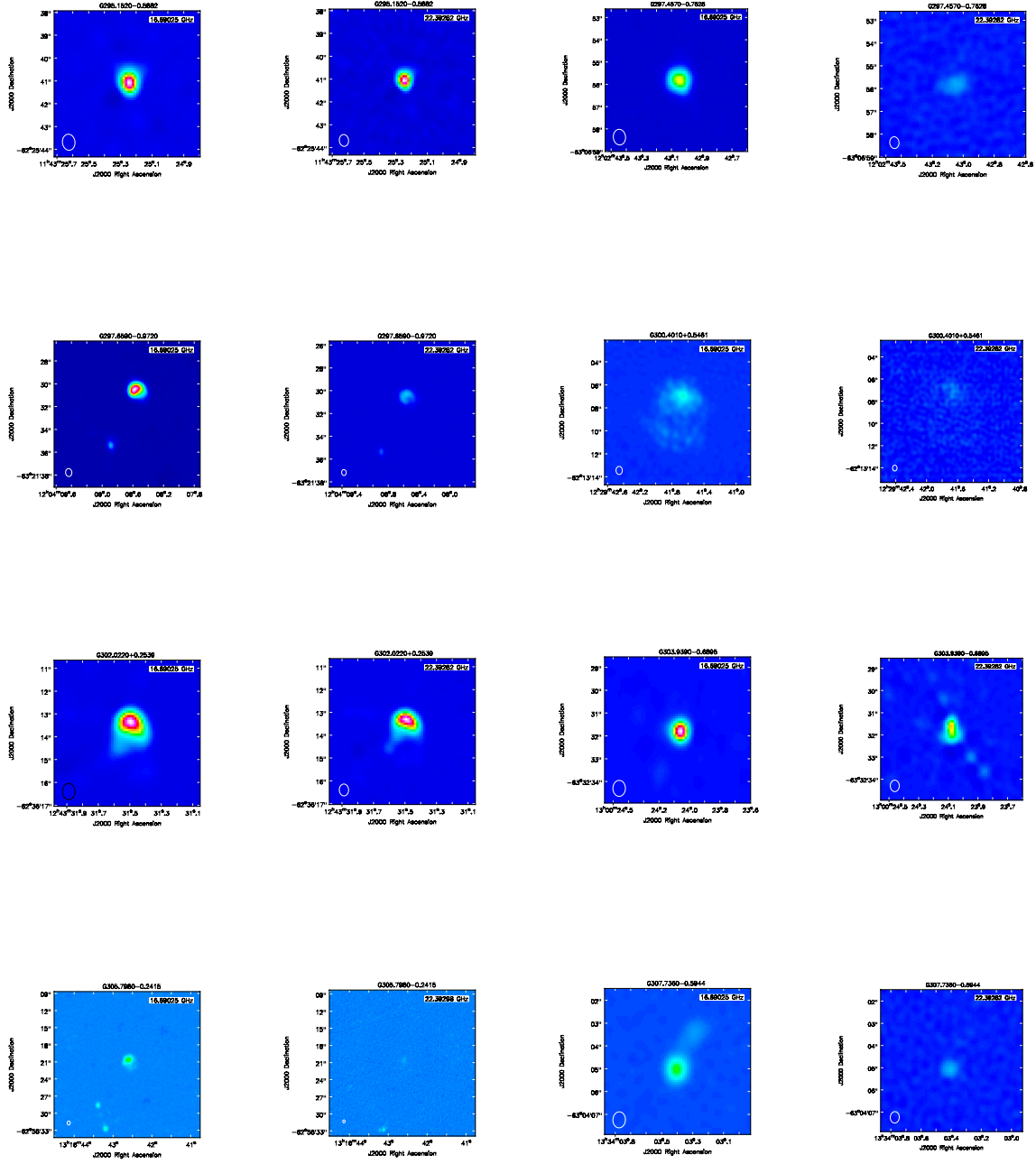


Figure A.1 | Radio images of the observed 17 and 22 GHz CORNISH-South UCHII regions. The same source is presented in both frequencies side by side.

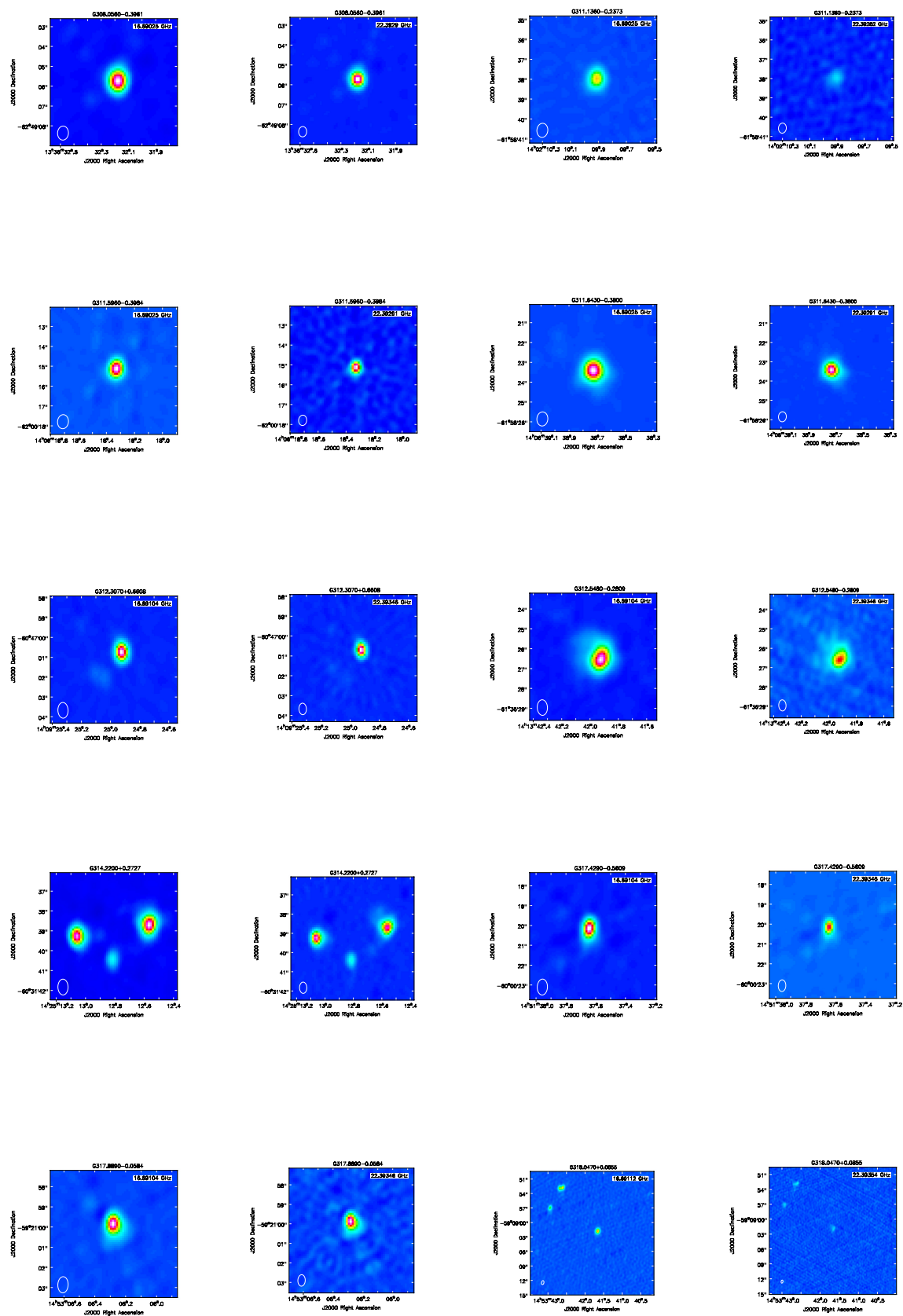


Figure A.2 Continued from previous figure

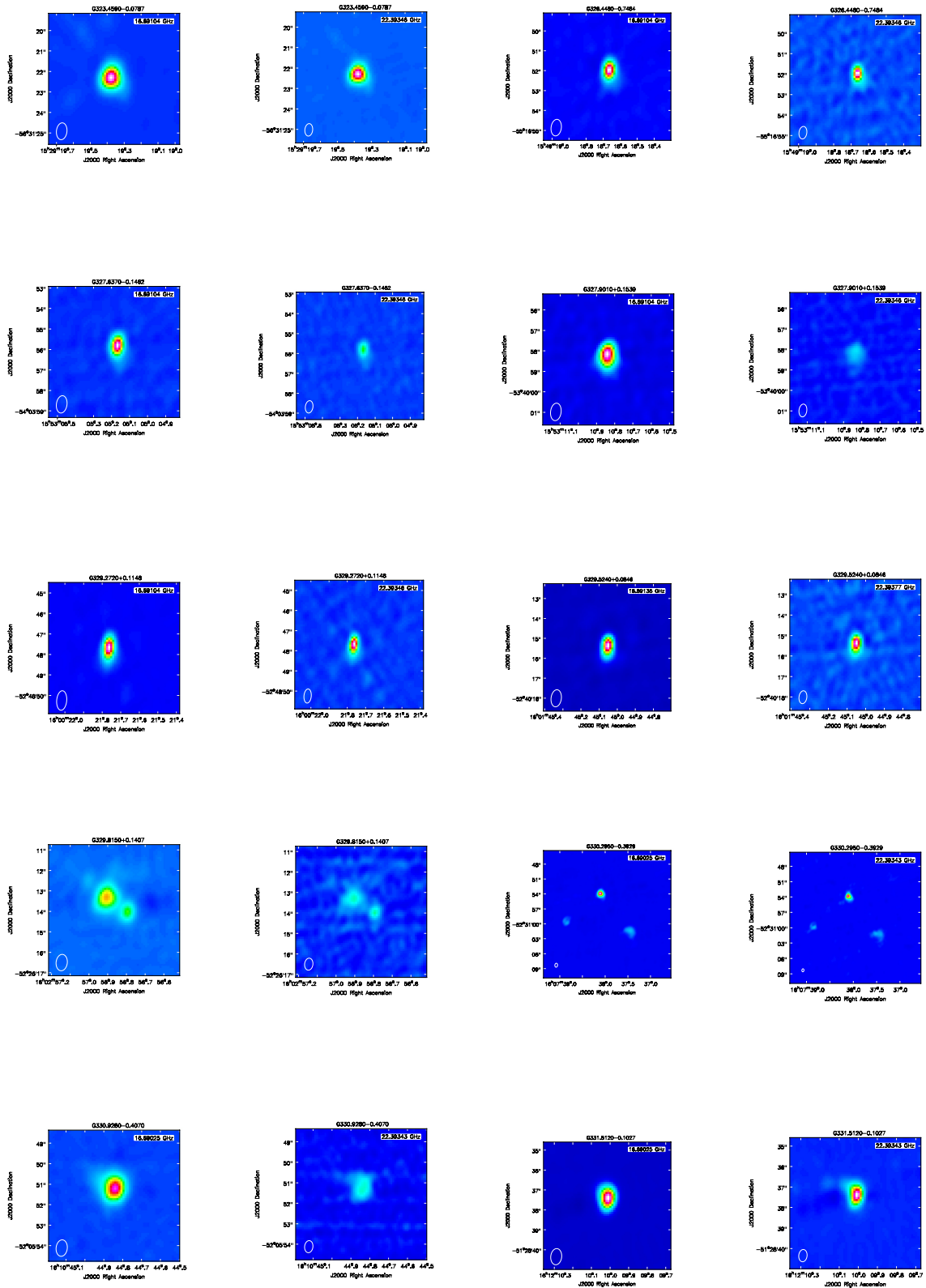


Figure A.3 Continued from previous figure

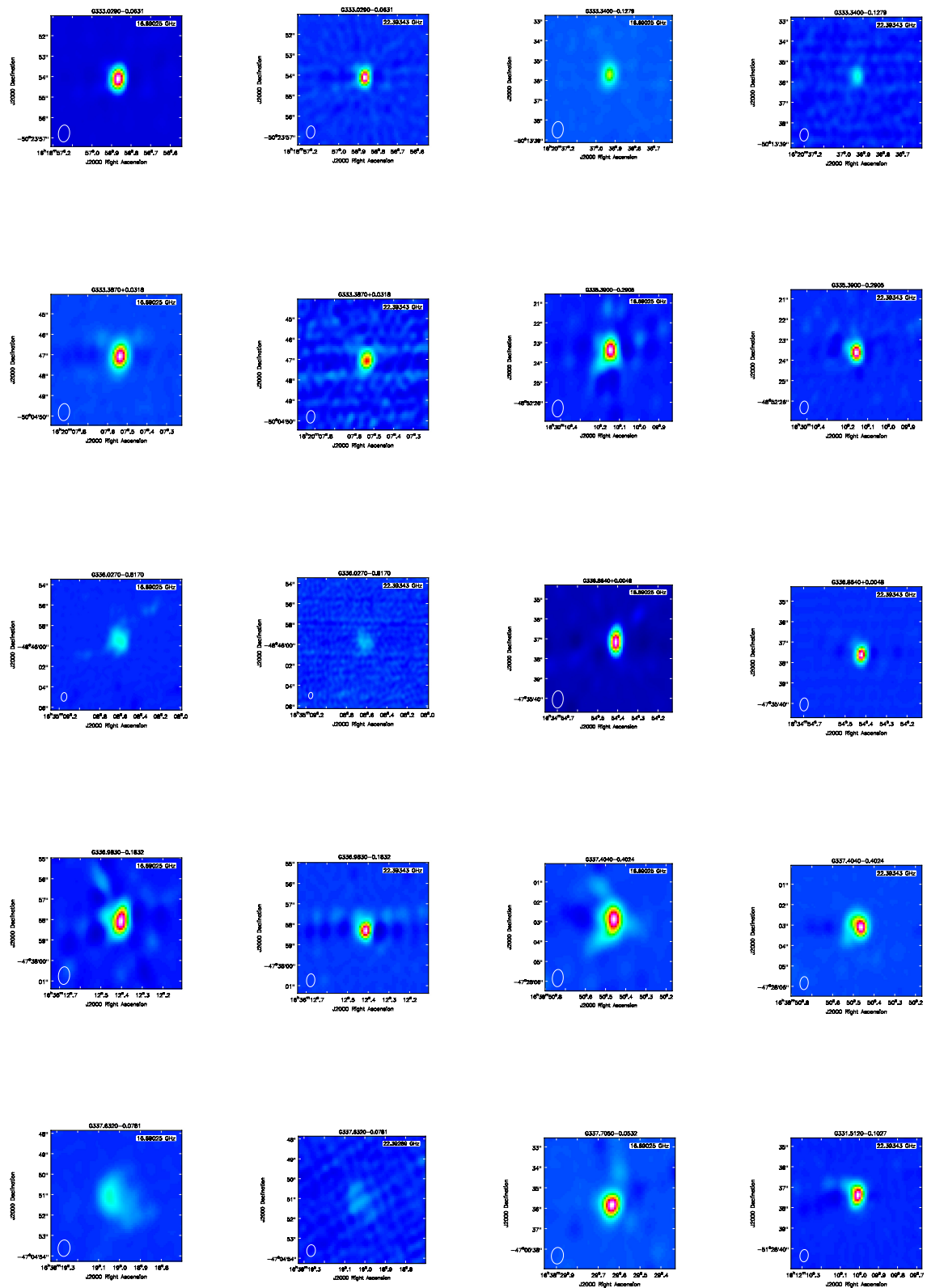


Figure A.4 Continued from previous figure

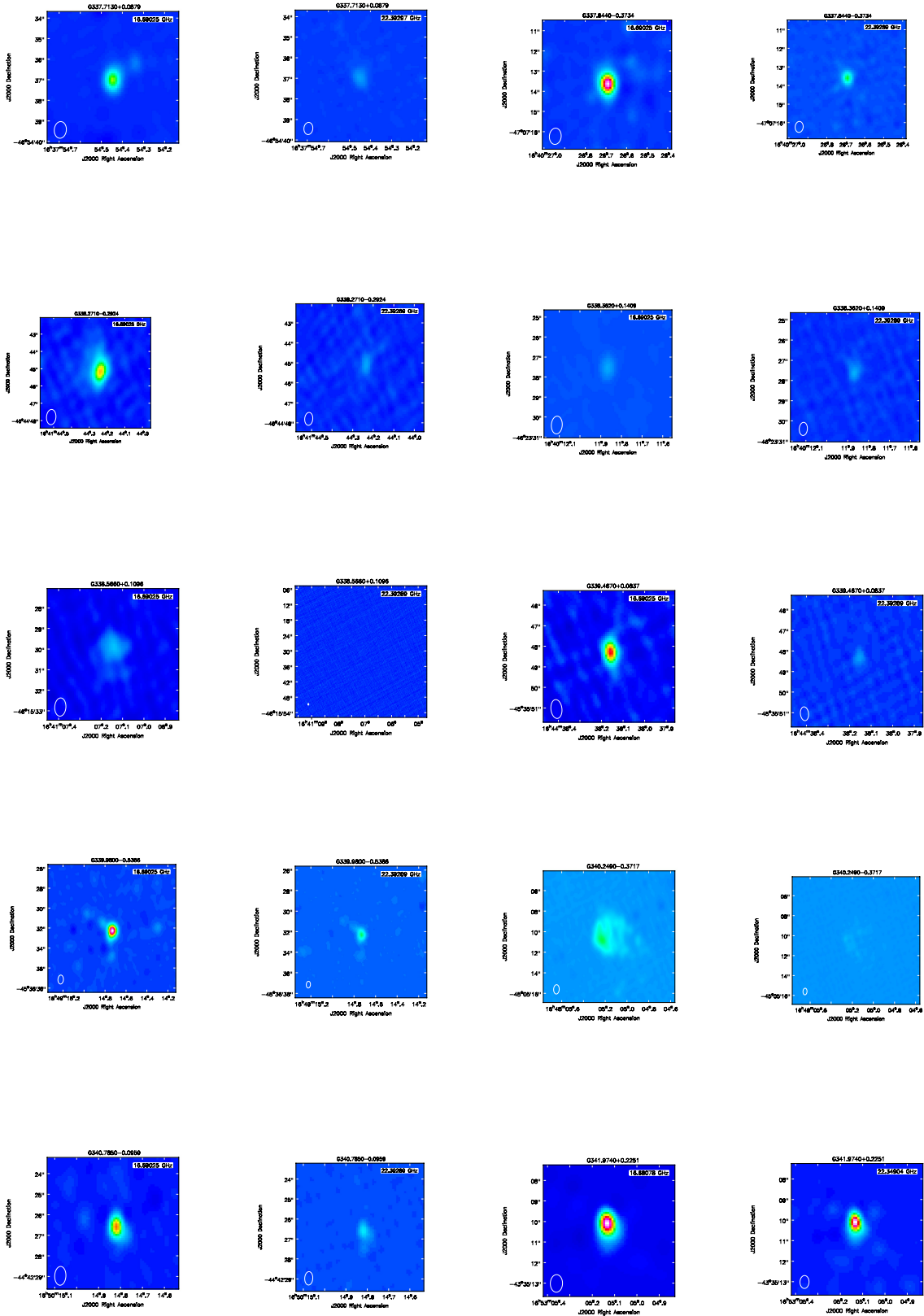


Figure A.5 Continued from previous figure

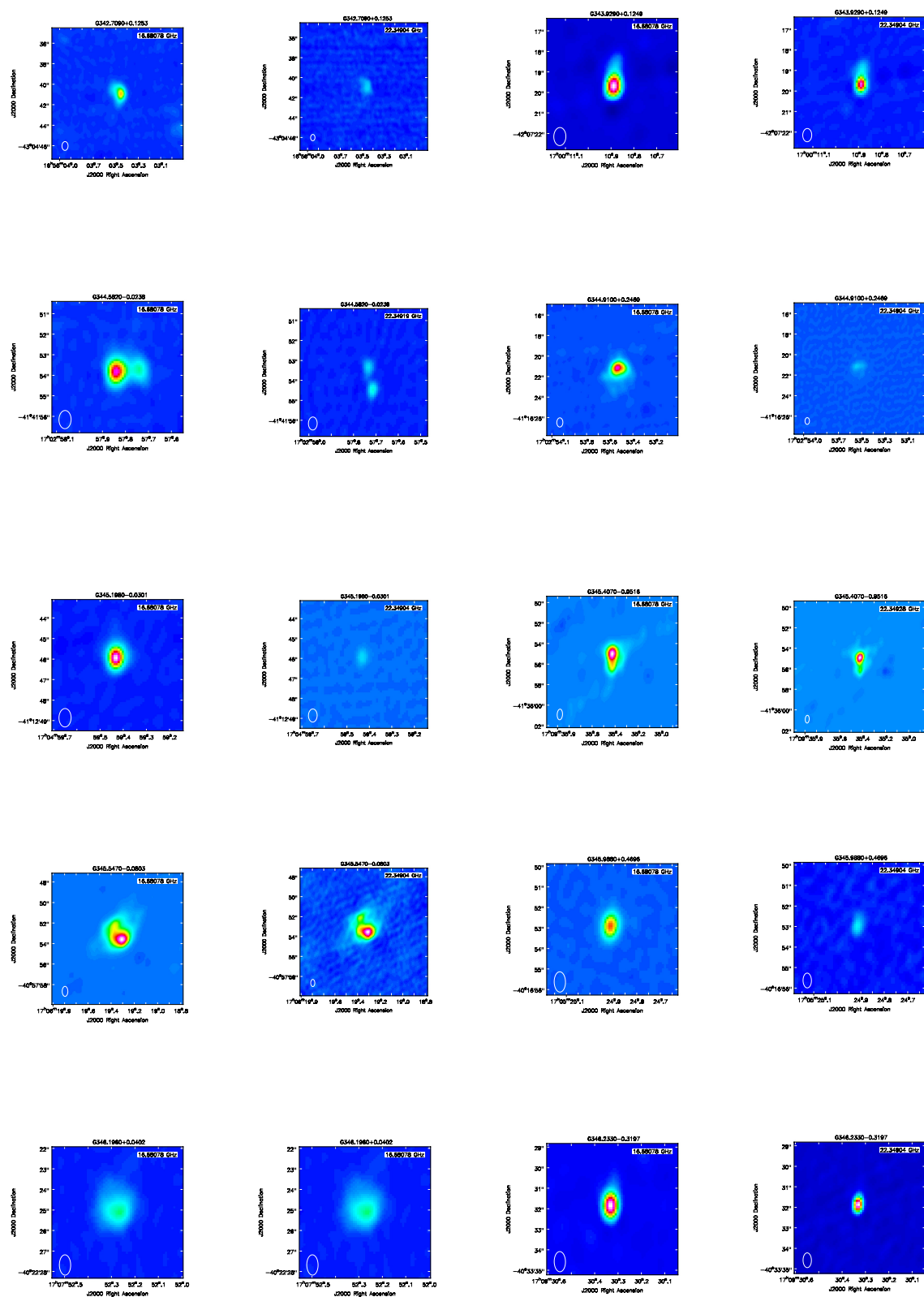


Figure A.6 Continued from previous figure

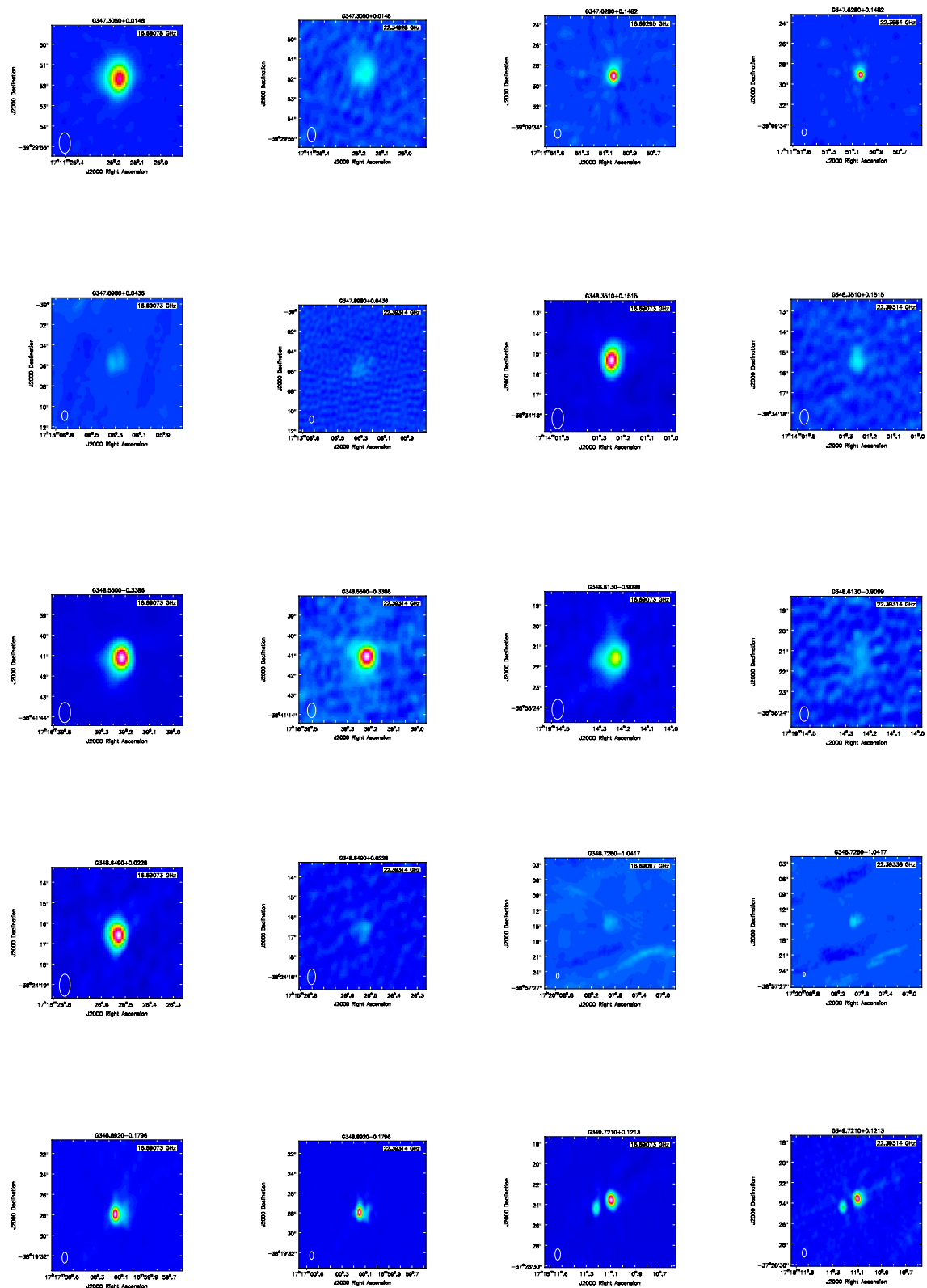


Figure A.7 Continued from previous figure

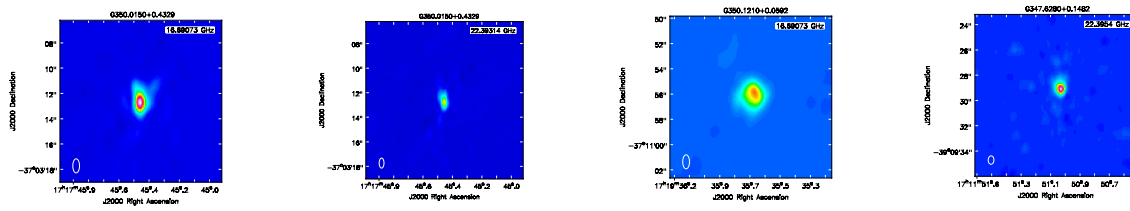


Figure A.8 Continued from previous figure

Appendix B

Additional Figures and Tables for Chapter 3

B.1 Measured 5.5 and 9GHz fluxes and estimated 9GHz-5GHz spectral indices of the CORNISH-South survey

Table B.1 | Fluxes of 5.5 GHz and 9 GHz CORNISH-South UCHII regions, and calculated 9GHz-5GHz spectral indices.

Source name	$F_{5.5GHz}$ (mJy)	F_{9GHz} (mJy)	$\alpha_{9GHz-5GHz}$
G295.1520-0.5882	22.83 ± 0.20	18.39 ± 0.08	-0.440 ± 0.091
G295.2090-0.7448	6.24 ± 0.14	4.60 ± 0.64	-0.620 ± 0.640
G297.2530-0.7540	5.41 ± 0.22	2.67 ± 0.49	-1.431 ± 0.351
G297.4570-0.7628	5.55 ± 0.11	5.53 ± 0.22	-0.009 ± 0.319
G297.5360-0.8283	38.29 ± 0.34	35.94 ± 0.31	-0.128 ± 0.407
G297.6620-0.9763	3.87 ± 0.28	1.96 ± 0.77	-1.383 ± 0.560
G298.8320+0.1270	108.03 ± 0.35	81.92 ± 0.02	-0.562 ± 0.019
G302.0220+0.2539	97.02 ± 0.32	99.33 ± 0.12	0.048 ± 0.180
G302.0320-0.0605	932.20 ± 3.35	1346.38 ± 0.01	0.746 ± 0.0397
G303.1170-0.9714	479.21 ± 1.69	380.70 ± 0.01	-0.467 ± 0.0129
G303.5350-0.5970	9.55 ± 1.90	11.18 ± 0.13	0.320 ± 0.447
G303.9300-0.6878	16.00 ± 0.16	28.44 ± 0.07	1.168 ± 0.595
G303.9390-0.6895	38.38 ± 0.19	48.06 ± 0.03	0.457 ± 0.075
G304.5560+0.3275	83.34 ± 0.70	72.99 ± 0.09	-0.269 ± 0.200
G305.3590+0.1995	234.06 ± 6.12	161.79 ± 0.09	-0.750 ± 0.088
G305.3600+0.1513	45.47 ± 0.71	112.97 ± 0.120.13	1.848 ± 0.569
G305.5530-0.0118	13.92 ± 0.17	11.19 ± 0.17	-0.443 ± 0.186
G305.5620+0.0123	14.91 ± 2.33	43.03 ± 0.23	2.153 ± 0.752
G305.7980-0.2415	9.91 ± 0.15	10.28 ± 0.15	0.075 ± 0.227
G305.8000-0.2438	0.97 ± 0.10	2.28 ± 0.74	1.736 ± 4.644
G307.6100-0.2933	1.13 ± 0.11	1.60 ± 1.07	0.711 ± 3.131

Table B.2 | Continued from previous table.

Source name	$F_{5.5GHz}$ (mJy)	F_{9GHz} (mJy)	$\alpha_{9GHz-5GHz}$
G307.6220-0.2623	182.71 ± 0.92	118.46 ± 0.08	-0.880 ± 0.075
G307.7360-0.5944	5.61 ± 0.11	6.00 ± 0.24	0.136 ± 0.394
G308.0560-0.3961	106.89 ± 0.25	119.50 ± 0.05	0.226 ± 0.088
G308.2000-1.0200	30.80 ± 0.16	21.44 ± 0.049	-0.735 ± 0.047
G308.9180+0.1218	435.14 ± 7.31	189.40 ± 0.07	-1.689 ± 0.047
G309.9210+0.4787	346.56 ± 1.84	365.35 ± 0.03	0.107 ± 0.042
G311.1360-0.2373	3.13 ± 0.09	4.24 ± 0.35	0.617 ± 0.891
G311.5960-0.3984	2.27 ± 0.10	3.42 ± 0.67	0.833 ± 2.390
G311.6430-0.3800	195.54 ± 0.47	238.03 ± 0.07	0.399 ± 0.139
G312.3070+0.6608	26.49 ± 0.17	36.19 ± 0.07	0.633 ± 0.194
G312.5480-0.2809	21.67 ± 0.17	15.87 ± 0.11	-0.632 ± 0.107
G314.2200+0.2727	38.65 ± 1.55	33.96 ± 0.17	-0.263 ± 0.215
G315.3270-0.2291	6.90 ± 0.13	2.79 ± 0.50	-1.836 ± 0.311
G316.3580-0.3611	5.96 ± 0.15	3.82 ± 0.33	-0.904 ± 0.290
G316.3600-0.3632	5.68 ± 0.15	2.31 ± 0.62	-1.828 ± 0.391
G317.4290-0.5609	41.53 ± 3.56	35.79 ± 0.04	-0.302 ± 0.128
G317.8690+0.1541	7.27 ± 0.25	2.19 ± 0.57	-2.432 ± 0.302
G317.8890-0.0584	14.10 ± 0.15	11.54 ± 0.13	-0.406 ± 0.141
G318.0470+0.0855	2.72 ± 0.10	1.92 ± 0.72	-0.713 ± 0.686
G319.3620+0.0133	58.20 ± 0.33	32.08 ± 0.04	-1.209 ± 0.033
G319.4000-0.0125	397.29 ± 10.21	86.51 ± 0.18	-3.095 ± 0.084
G319.4520-0.0218	136.42 ± 0.66	134.54 ± 0.07	-0.028 ± 0.098
G320.2340-0.2836	324.12 ± 1.52	347.86 ± 0.05	0.144 ± 0.074
G320.4270+0.1030	11.25 ± 2.40	3.02 ± 0.70	-2.671 ± 0.366
G320.7780+0.2423	23.98 ± 0.33	7.35 ± 0.19	-2.401 ± 0.102
G321.1250-0.2653	29.54 ± 0.23	13.47 ± 0.10	-1.594 ± 0.071
G323.4590-0.0787	425.72 ± 27.40	304.78 ± 0.11	-0.679 ± 0.126
G324.2000+0.1198	1708 ± 54.90	1093.49 ± 0.02	-0.906 ± 0.034
G327.4020+0.4446	99.51 ± 10.60	60.90 ± 0.05	-0.997 ± 0.087
G327.9010+0.1539	3.64 ± 0.13	2.2 ± 0.74	-0.995 ± 0.624
G328.3070+0.4304	1142.42 ± 78.84	1148.40 ± 0.01	0.011 ± 0.102
G328.8080+0.6331	974.30 ± 57.00	515.40 ± 0.07	-1.293 ± 0.066
G329.2720+0.1148	1.72 ± 0.18	4.50 ± 0.33	1.955 ± 1.292
G330.2840+0.4931	41.62 ± 0.37	23.90 ± 0.27	-1.126 ± 0.414
G330.9530-0.1823	1133.74 ± 114.91	1075.38 ± 0.01	-0.107 ± 0.137
G331.2780-0.1888	35.61 ± 7.19	11.37 ± 0.12	-2.319 ± 0.127
G331.3520+1.0655	88.57 ± 0.98	58.65 ± 0.20	-0.837 ± 0.181
G331.4420-0.1874	61.72 ± 5.38	44.77 ± 0.23	-0.652 ± 0.242
G331.5120-0.1027	87.52 ± 0.48	96.25 ± 0.15	0.193 ± 0.257
G331.5420-0.0665	181.50 ± 7.26	160.81 ± 0.03	-0.246 ± 0.060
G331.6030-0.1075	15.91 ± 0.30	22.71 ± 0.41	0.723 ± .234
G332.6930-0.6120	11.07 ± 0.23	19.06 ± 0.09	1.105 ± 0.614
G332.8260-0.5493	2151.59 ± 12.44	3969.66 ± 0.00	1.244 ± 0.081
G333.0140-0.4419	53.16 ± 0.94	67.40 ± 0.02	0.482 ± 0.054
G333.0290-0.0631	5.56 ± 0.15	11.65 ± 0.16	1.501 ± 3.551

Table B.3 | Continued from previous table.

Source name	$F_{5.5GHz}$ (mJy)	F_{9GHz} (mJy)	$\alpha_{9GHz-5GHz}$
G333.1350-0.4322	1246.00 ± 4.72	1936.83 ± 0.02	0.896 ± 0.080
G333.1630-0.1003	139.64 ± 3.44	70.30 ± 0.19	-1.394 ± 0.138
G333.2210-0.4022	11.80 ± 2.25	7.76 ± 0.19	-0.850 ± 0.333
G333.3870+0.0318	4.61 ± 0.12	2.62 ± 0.75	-1.143 ± 0.594
G333.6790-0.4353	61.03 ± 0.26	80.01 ± 0.02	0.550 ± 0.055
G334.7030-0.1263	14.68 ± 2.58	7.17 ± 0.25	-1.455 ± 0.219
G334.7220-0.6531	287.87 ± 16.12	113.55 ± 0.10	-1.889 ± 0.073
G335.3900-0.2905	10.37 ± 0.17	15.13 ± 0.10	0.766 ± 0.331
G335.5780-0.2072	60.23 ± 3.63	38.57 ± 0.04	-0.905 ± 0.065
G336.0270-0.8170	6.20 ± 0.34	8.21 ± 0.16	0.571 ± 0.412
G336.3680-0.0043	626.40 ± 48.86	411.15 ± 0.10	-0.855 ± 0.113
G336.4100-0.2577	23.86 ± 0.32	17.61 ± 0.08	-0.616 ± 0.082
G336.8450-0.0089	42.03 ± 0.50	15.86 ± 0.07	-1.978 ± 0.042
G336.8640+0.0048	6.41 ± 0.31	11.98 ± 0.15	1.269 ± 2.310
G336.8880+0.0489	21.83 ± 0.40	5.02 ± 0.26	-2.985 ± 0.122
G336.9000-0.0319	197.47 ± 0.63	217.79 ± 0.07	0.198 ± 0.122
G336.9830-0.1832	24.98 ± 0.20	40.49 ± 0.24	0.981 ± 1.143
G337.0040+0.3239	242.47 ± 1.30	147.70 ± 0.09	-1.001 ± 0.076
G337.0470-0.0011	8.70 ± 0.23	2.34 ± 0.65	-2.668 ± 0.323
G337.1940-0.0599	10.50 ± 2.77	10.75 ± 0.63	0.047 ± 1.015
G337.4040-0.4024	107.76 ± 0.95	176.01 ± 0.11	0.996 ± 0.545
G337.6120-0.0597	7.62 ± 0.38	7.62 ± 0.22	0.001 ± 0.326
G337.6320-0.0781	50.30 ± 0.26	47.39 ± 0.17	-0.121 ± 0.225
G337.7050-0.0532	95.64 ± 0.70	252.39 ± 0.06	1.970 ± 0.208
G337.7110+0.0855	95.64 ± 0.70	188.08 ± 0.06	0.624 ± 0.162
G337.7130+0.0879	11.13 ± 0.55	21.76 ± 0.07	1.361 ± 3.919
G337.8440-0.3747	12.71 ± 0.17	29.85 ± 0.06	1.733 ± 0.373
G337.9270-0.4575	903.35 ± 6.20	1065.07 ± 0.01	0.334 ± 0.014
G338.0750+0.0120	958.95 ± 34.33	624.96 ± 0.03	-0.869 ± 0.043
G338.1470-0.1715	12.47 ± 0.23	10.32 ± 0.11	-0.383 ± 0.125
G338.2710-0.2924	28.02 ± 0.25	14.68 ± 0.10	-1.312 ± 0.077
G338.3320+0.1320	299.54 ± 1.70	444.12 ± 0.06	0.800 ± 0.205
G338.3620+0.1409	7.05 ± 0.22	3.06 ± 0.59	-1.691 ± 0.386
G338.3740-0.1516	175.13 ± 1.17	206.96 ± 0.08	0.339 ± 0.153
G338.4610-0.2579	18.38 ± 0.24	8.73 ± 0.74	-1.512 ± 0.517
G338.4890+0.0448	67.03 ± 0.63	35.79 ± 0.02	-1.274 ± 0.020
G338.5660+0.1096	4.98 ± 0.19	4.54 ± 0.27	0.190 ± 0.350
G338.6810-0.0843	91.50 ± 0.69	105.25 ± 0.12	0.284 ± 0.209
G338.9160+0.3833	189.36 ± 8.73	130.59 ± 0.16	-0.755 ± 0.153
G338.9220+0.6243	199.7 ± 10.14	114.25 ± 0.03	-1.135 ± 0.0453
G339.1040+0.1482	78.06 ± 4.40	65.28 ± 0.24	-0.363 ± 0.282
G339.2820+0.1359	1.57 ± 0.12	2.12 ± 0.67	0.610 ± 1.727
G339.4670+0.0837	6.16 ± 0.16	4.26 ± 0.36	-0.751 ± 0.335
G339.4770+0.1852	72.00 ± 0.49	38.88 ± 0.32	-1.251 ± 0.242
G339.5660-0.0863	20.52 ± 0.29	9.25 ± 0.14	-1.617 ± 0.095
G339.5900+0.0831	61.20 ± 0.50	34.25 ± 0.32	-1.179 ± 0.248

Table B.4 | Continued from previous table.

Source name	$F_{5.5GHz}$ (mJy)	F_{9GHz} (mJy)	$\alpha_{9GHz-5GHz}$
G339.7460+0.0952	17.27 ± 0.29	10.50 ± 0.12	-1.011 ± 0.100
G340.2490-0.0461	95.36 ± 1.30	26.04 ± 0.43	-2.636 ± 0.217
G340.7850-0.0959	6.27 ± 0.13	6.99 ± 0.25	0.221 ± 0.426
G341.7020+0.0521	175.60 ± 1.74	115.47 ± 0.01	-0.851 ± 0.013
G341.9740+0.2251	52.91 ± 0.47	54.71 ± 0.23	0.068 ± 0.346
G342.7090+0.1253	8.93 ± 0.19	5.03 ± 0.32	-1.165 ± 0.250
G343.9290+0.1249	19.10 ± 0.15	32.13 ± 0.06	1.056 ± 0.340
G344.5820-0.0238	9.48 ± 0.18	5.05 ± 0.31	-1.281 ± 0.238
G344.9100+0.24692	5.26 ± 0.43	12.71 ± 0.11	1.790 ± 0.740
G344.9110+0.2466	18.98 ± 0.20	12.71 ± 0.11	-0.814 ± 0.103
G345.0030-0.2243	165.47 ± 9.26	242.12 ± 0.09	0.773 ± 0.344
G345.1980-0.0301	5.91 ± 0.13	5.62 ± 0.27	-0.103 ± 0.366
G345.4070-0.9516	383.52 ± 5.89	667.83 ± 0.04	1.126 ± 0.292
G345.5470-0.0803	87.95 ± 0.35	61.99 ± 0.23	-0.711 ± 0.216
G345.8040+0.0480	42.44 ± 0.34	36.54 ± 0.35	-0.304 ± 0.413
G346.1630-0.1328	13.77 ± 0.40	8.08 ± 1.02	-1.084 ± 0.834
G346.1960+0.0402	6.72 ± 0.16	2.88 ± 0.48	-1.721 ± 0.313
G346.2330-0.3197	10.98 ± 0.17	15.14 ± 0.10	0.654 ± 0.279
G347.3050+0.0148	8.94 ± 0.15	4.16 ± 0.42	-1.555 ± 0.289
G347.6000+0.2437	57.45 ± 0.54	42.33 ± 0.42	-0.620 ± 0.423
G347.6280+0.1482	139.67 ± 6.57	167.80 ± 0.10	0.373 ± 0.212
G347.8700+0.0138	185.17 ± 1.49	357.05 ± 0.08	1.333 ± 2.144
G347.9660-0.4318	80.16 ± 0.69	88.75 ± 0.18	0.207 ± 0.311
G348.5500-0.3386	22.97 ± 0.21	16.41 ± 0.10	-0.682 ± 0.101
G348.6130-0.9099	2.14 ± 0.17	2.39 ± 0.80	0.226 ± 1.385
G348.6490+0.0228	3.65 ± 0.14	3.81 ± 0.43	0.090 ± 0.667
G348.6980-1.0276	1664.86 ± 10.32	1623.56 ± 0.03	-0.051 ± 0.045
G349.7210+0.1213	44.75 ± 0.32	9.02 ± 0.30	-3.251 ± 0.129
G350.0150+0.4329	125.69 ± 0.47	117.01 ± 0.28	-0.145 ± 0.366
G350.1110+0.0882	59.11 ± 1.49	36 ± 0.07	-0.991 ± 0.172
G350.1170+0.0686	126.22 ± 0.96	45.57 ± 0.36	-2.069 ± 0.213
G350.1210+0.0592	266.36 ± 0.66	247.75 ± 0.09	-0.147 ± 0.113